DEPOSITION AND MODELLING OF RARE EARTH DOPED OPTICAL FILMS

Ilana Massarek

Department of Electrical and Electronic Engineering
University College, London

A thesis submitted to University College, University of London
for the degree of Doctor of Philosophy

April 1994

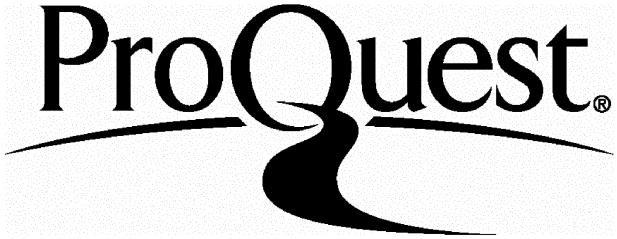

Abstract

For integration within optical circuits, active devices should ideally be kept as short as possible. As the gain of a device is related to its length and the concentration of active ions, it is necessary for short active devices to contain high levels of ion dopants. The experimental aim of the work presented in this thesis was to determine whether highly erbium-doped silicate glass (Er^{3+}-SiO_2) can be fabricated with suitable characteristics to produce planar active devices. The performance of rare-earth doped optical amplifiers was analysed theoretically.

In highly doped materials, the optical gain is affected by ion-ion interactions. By solving the rate equations for the levels involved in radiative transitions in the model, the material gain was predicted as a function of the pump power and Er concentration. The negative effects of ion-ion interactions on gain can be overcome by careful design of the waveguide geometry and refractive index step. In particular, the dependence on Er^{3+} concentration of threshold pump power and amplifier gain are discussed.

Plasma enhanced chemical vapour deposition (PECVD) was used to deposit the thin films. PECVD is a non-equilibrium low temperature deposition process. The deposition conditions of aluminium oxide, silicon dioxide, and erbium oxide were studied. By analysing the chemical composition, refractive index, deposition rate, and uniformity of the films, the process conditions were optimised. The silicon dioxide and erbium oxide processes were combined to fabricate Er^{3+}-doped silicate planar waveguides. The Er doping was achieved using $Er(thd)_3$, a volatile organic precursor. Waveguides with a dopant concentration of 10^{20}-10^{22} ion/cm^3 showed the typical fluorescence spectra of the Er^{3+}-ion and had a radiative lifetime of 9ms before annealing and 2-3ms after annealing and for high pump powers.

Acknowledgements

For the financial support for this project I would like to thank:

Dott. A Fioretti, Dott. M. del Giudice, and Dott. M. Valli from the former Face-Alcatel in Rome.

The Optical Interdisciplinary Research Council (OIRC), and in particular Prof. D. Payne of Southampton University.

Mr. Michael Grant of Bell Northern Research Europe (BNRE) in Harlow.

The British Council and the Italian Ministry of Foreign Affairs.

The Science and Engineering Research Council.

I am particular grateful to Prof. Chris Pitt, Dott. Marco Federighi and Dr. Tim Mills for their supervision and help in finding new sources of financial support every time I was stranded.

I am indebted to Phil Trwoga for constant support in the deposition experiments, for the fluorescence and lifetime measurements, and for providing all kinds of verbal and practical help.

A special mention must be given to my colleagues at UCL: J. Rice, Dr. T. Kenyon, A. James, for providing help in optical experiments, J. Van Sickle for building and adapting equipment, F. Stride, K. Lee for assistance in the cleanroom and T. Rivers for initial help in designing the gas delivery system.

The following people have contributed to the analysis of the waveguides:

Dr. J. Milledge of the UCL geology department for assistance in X-ray analysis.

D. Hall of Loughborough Consultants for AES.

Dr. B. Farmeny from Sussex University for RBS.

Dr. M. Hempstead from Southampton University for the first lifetime measurement. R. Bellerby form BNRE and J. Gallagher from Imperial College London for support in ellipsometry measurements.

Jasmine Pradissitto must be acknowledged for providing entertaining and diverse discussions.

Of course my greatest thanks must go to Miles Eddowes who valiantly took on the pleasure of doing some minor proof reading for an excessive reward.

Finally, I am grateful to my late father Gabriele Massarek, and my new husband Adam Beaudin for providing support.

Table of contents

List of tables

Chapter 3

Chapter 4

Chapter 5

Chapter 6

List of illustrations

Chapter 5

Chapter 6

Chapter 1: Introduction

1.1. General Introduction

This thesis is concerned with the modelling and fabrication of active thin films to be used as optical waveguide amplifiers in an integrated circuit. The primary aim of this chapter is to place the work in context.

The term integrated optics was introduced in the 1960's[1,2,3] to refer to the combination of several optical components within a single optical waveguiding system. The field is based on the concept of optical waveguiding[4,5,6] in which a beam of light is guided along a thin dielectric layer deposited on a substrate with a lower refractive index.

Several passive devices such as stripe waveguides, directional couplers[7], junctions and active devices such as modulators[8], lasers[9] and amplifiers have been successfully made in many different designs. Complete integration of optical circuitry requires light to be generated, guided, amplified, and modulated on a single component and is difficult to achieve on monolithically grown wafers.

There are presently two schools of thought for integrating higher levels of optics and electronics[10]. In the mainstream one, all functions take place on a monolithically grown and processed wafer such as InP, GaAs, Si/Ge and GaAs on Si. The second approach is a hybrid version where the different functions are combined on a common Si substrate using surface mounting techniques with glass (or other) optical waveguides to interconnect the devices. The hybrid approach, of direct relevance to this thesis, is less elegant than the first, but offers lower cost integrated circuits for commercial applications.

Silicon has a number of attractive properties as a substrate for integrated optics. It is relatively low cost and available in large area. It has high thermal conductivity and good electrical properties; it can be a conductor, semiconductor or insulator depending on processing. Furthermore, solvents do not affect the properties of Si and SiO_2 and high temperature (400°C) soldering can be used to seal pakages.

Two types of passive planar guides are widespread. The size and core-superstrate refractive index difference of the guides are designed for efficient mode matching. The first type is an approximately 4μm wide rib nitride waveguide on silica used for

matching to semiconductor lasers. The second type is an 8-11μm monomode silica waveguide used for matching with an optical fibre. To enable light to be coupled efficiently between integrated optical circuits and single-mode fibres, channel waveguides are designed to support a single spatial mode with a mode size matched to that of the fibres.

Glass fibres[11] are used as low loss transmission lines because of their large bandwidth in the visible and infrared regions. Transmission over a long distance results in signal attenuation. In the mid-eighties, the use of rare-earths as dopants[12] led to the first signal fibre amplifiers[13,14,15]. By combining the optical gain of rare-earth ions with the large optical confinement available in a single mode optical fibre, these fibres offer a fascinating medium in which to produce efficient low cost devices. In past years, most of the rare-earths have been investigated in a range of glass hosts such as silica and fluoride fibres[16]. This effort has led to the demonstration of a variety of efficient laser sources and amplifiers. The spectrum of possibilities offered by this technology is staggering, ranging from blue and far infrared continuos-wave lasers, to 1.3μm and 1.5μm amplifiers. These devices are expected to play a fundamental role in several important commercial applications. The erbium-doped fibre amplifiers which operate in the important 1.55μm telecommunication window have excellent properties for applications in optical communication systems. These characteristics include high gain, low noise, low interchannel cross-talk, and low drive power.

Because of their cylindrical geometry, rare-earth doped fibres cannot be integrated within planar optical circuits. Rare-earth doping of planar waveguides is an attractive method to obtain compact and practical optical amplifiers and lasers which can be easily integrated within optical circuits. To have potential applications in integrated optics, these glass waveguides should be deposited directly onto a silica on silicon substrate on which other components can be fabricated or mounted. For integration within optical circuits, active devices must be kept as short as possible. Short active devices need doping levels which are two orders of magnitude higher than those generally used in fibres.

Rare-earth doped glass on Si waveguides would offer an array of novel, compact and extremely efficient practical amplifiers and lasers, which due to their low power requirements could be driven by inexpensive laser diodes. Many future applications

are envisioned; these range from components in communication and sensor networks to medical lasers.

The development of fibre communications is providing an incentive to develop active waveguide designs and compositions compatible with standard low attenuation silica-based fibre. Specifically, the limitations of fusion splicing for simultaneously interconnecting many telecommunication fibres could be overcome by using a planar device with low insertion loss, low reflectivity, low noise and high gain. This device would allow the reliable interconnection of several telecommunication fibres. An Er^{3+}-SiO_2 planar waveguide could be used to compensate for insertion losses and would be an ideal candidate for matching to erbium doped fibre amplifiers. A simple illustrative application of the Er^{3+}-glass waveguides is the star coupler[17], see fig. 1.1.

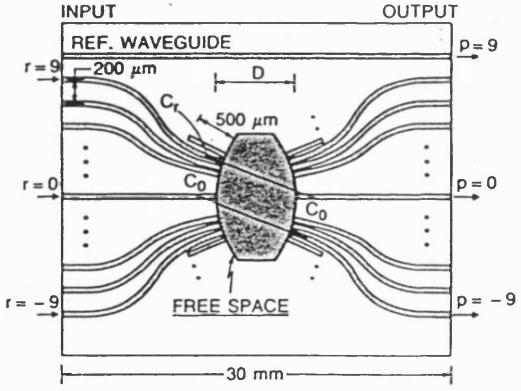

Figure 1.1. Geometry of a 19 X 19 star coupler.

Here, an array of waveguides converge to a central region in which the glass cores merge into a slab waveguide. The waveguides radiate across the slab and are intercepted by closely spaced waveguides on the other side. A key feature of star couplers is the V groove[18] which enables fast fibre alignment. In addition to fibre to fibre losses, there are also losses due to division. The use of Er^{3+}-doped glass in either the free-space planar guide or throughout the array could be used to compensate for these losses.

In 1989, when this research started, low-loss passive optical glass waveguides had been investigated. Work on rare-earth doped $LiNbO_3$ had already been started at UCL[19]. Erbium-doped fibre amplifiers and ion exchange waveguides in rare-earth

doped glasses[20] were starting to be developed at Southampton University. The challenge of this research was to investigate the possibility of growing rare-earth doped silicates on silica on silicon using plasma enhanced chemical vapour deposition (PECVD). To optimise the deposition conditions, the film characteristics will require analysis. The final aim is to determine both experimentally and theoretically, whether erbium doped glass on silicon would be a suitable material for active optical devices such as waveguide amplifiers.

1.2. Outline of thesis

Following an introduction, chapter 2 provides a general summary of waveguide theory and gives the fundamental principles of active materials and amplifiers. Only the passive and active characteristics that are relevant to Er^{3+}-doped amorphous silica waveguides are discussed.

In the first part of Chapter 3, rare-earth ions and their characteristics are introduced. The level system for the Er^{3+} ion is presented and the level notation explained. A discussion of Er^{3+} sites in glass and structural models follows.

Chapter 4 is aimed at developing a theoretical understanding of highly doped Er^{3+}-silicates. The rate equations for the energy levels of the Er^{3+}-ion are derived taking into account the processes which affect gain. The results obtained by numerically solving the wave equation are presented. A discussion of rare-earth distribution and its effect on transfer rates and upconversion coefficients concludes the chapter.

The experimental techniques used to deposit and analyse the materials are presented in chapter 5: the choice of precursors and experimental results are in chapter 6. Chapter 5 begins with a comparison of PECVD with other glass forming techniques. The fundamental principles involved in the deposition are discussed. A detailed description of the equipment designed, developed and installed, follows. The diagnostics techniques used to analyse the passive and active film characteristics are introduced.

Chapter 6 begins with the reasons for the choice of precursors for the silica (SiO_2), alumina (Al_2O_3), and erbia (Er_2O_3), and the results of separate calibration experiments for each component. The Er^{3+}-SiO_2 binary glass results are presented

and the fluorescence spectra and lifetime measurements are displayed. The final results confirm that fluorescing highly doped Er^{3+}-SiO_2 can be produced by PECVD.

The experimental and theoretical results are compared in chapter 7. It is argued that the project was successful since it demonstrated that highly doped Er^{3+}-glass planar waveguides have the right active characteristics to be used as integrated optical amplifiers. Suggestions for future developments are provided.

References

1. T. Tamir, 'Introduction', in 'Integrated optics', T. Tamir (ed.), Springer-Verlag (1979).

2. H. Koglenik, 'An introduction to integrated optics', IEEE Trans, **MTT23**, 1, pp.2-20 (1975).

3. P.K. Tien, 'Integrated optics and new wave phenomena in optical waveguides', Rev. of Mod. Phys, **49**, 2, pp.361-411 (1977).

4. H. Koglenik, 'Theory of dielectric waveguides' in 'Integrated optics', T. Tamir (ed.), Springer-Verlag (1979).

5. R. Ulrich, 'Thin dielectric films for integrated optics', J. Vacuum. Sci. and Technol., **11**, 1, pp.156-162 (1974).

6. P.K. Tien, 'Light waves in thin films and integrated optics', Appl. Opt., **10,** pp.2395-2413 (1971).

7. C.S. Tsai, 'Optical channel waveguide switch and coupler using total internal reflection', IEEE J. Quantum Electron., **14**, pp.513-517 (1978).

8. A. Neyer, W. Sohler, 'High speed cut-off modulator using a titanium-diffused lithium niobate channel waveguide', Appl. Phys. Lett., **35**, pp.256-258 (1979).

9. E. Lallier, J.P. Pochelle, M. Papuchon, M.P. De Micheli, M.J. Li, Q. He, D.B. Ostrowsky, C. Grezes-Beset and E. Pelletier, 'Nd:MgO:$LiNbO_3$ channel waveguide laser devices', IEEE J. Quantum Electron., **27**, 2, pp.618-625 (1991).

10. C.H. Henry, G.E. Blonder and R.F. Kazarinov, 'Glass waveguides on silicon for hybrid optical packaging', J. Lightwave. Technol., **7**, 10, pp.1530-1539 (1989).

11. D.N. Payne, A.J. Barlow, and J.J. Ramskov Hansen, 'Development of low- and high-birefringence optical fibres', IEEE J. Quantum Electron., **18,** 4, pp.477-487 (1982).

12. S.B. Poole, D.N. Payne, and M.E. Fermann, 'Fabrication of low-loss optical fibres containing rare-earth ions', Electron. Lett., **21**, 17, pp.737-738 (1985).

13. R.J. Mears, L. Reekie, S.B. Poole, and D.N. Payne, 'Neodynium-doped silica single-mode fibre lasers', Electron. Lett., **21**, 17, pp.739-740 (1985).

14. S.B. Poole, D.N. Payne, R.J. Mears, M.E. Fermann, and R.I. Laming, 'Fabrication and characterisation of low-loss optical fibres containing rare-earth ions', J. Lightwave Technol., **LT-4**, 7, pp.870-876 (1986).

15. L. Reekie, I.M. Jauncey, S.B. Poole, and D.N. Payne, 'Diode-laser-pumped operation of an Er^{3+}-doped single-mode fibre laser', Electron. Lett., **23**, pp.1076-1077, (1987).

16. M.J.F. Digonnet, 'Rare-earth doped fibre lasers and amplifiers', M.J.F. Digonnet (ed.), Dekker, (1993).

17. C. Dragone, C.H. Henry, I.P. Kamninow and R.C. Kistler, 'Efficient single mode integrated optic star coupler on Si', IEEE Photonics Technol. Lett., **1**, pp.241-243 (1989).

18. S. Day, R. Bellerby, G. Cannell and M. Grant, 'Silicon based fibre pigtailed 1X16 power splitter', Electron. Lett., **28**, 10, pp.920-922, (1992).

19. M.V. Plissi, 'Rare-earth doped stripe waveguide laser devices' Ph. D. Thesis, University College, UCL, (1993).

20. T. Feuchter, E.K. Mwarania, J. Wang, L. Reekie, and J.S. Wilkinson, 'Erbium doped ion-exchanged waveguide lasers in BK7 glass', IEEE Photonics Technol. Lett., **4**, 6, pp. 542-553, (1992).

Chapter 2: Introduction to waveguides and amplifiers

Introduction

In this chapter a simplified understanding of optical waveguides and amplifiers is given. The material covered is from the literature and is generally known and accepted. The equations and concepts introduced here are used in subsequent chapters to generate the theory of Er^{3+}-doped optical waveguide amplifiers.

2.1. Optical waveguides

Optical waveguides are structures which are used to confine and guide light in guided wave devices and integrated circuits[1].
A planar guide consists of a thin film of refractive index n_f sandwiched between a substrate and a superstrate with lower refractive indices, n_s and n_c, respectively. The light is confined by internal reflection at the film-substrate and film-superstrate interface.

By Snell's law

$$n_f \sin\theta_f = n_c \sin\theta_c \qquad 2.1\text{-}1$$

At angles greater than critical angle, θ, given by

$$\sin\theta = \frac{n_c}{n_f} \qquad 2.1\text{-}2$$

total internal reflection occurs.

When θ is small, a light wave from the superstrate is refracted into the film and refracted again into the substrate. This is known as a radiation mode. When θ is increased to a value larger than the critical angle for the film-superstrate interface, light is totally internally reflected at the film-superstrate interface only. This is a substrate mode. Finally a waveguide mode[2] occurs when θ is larger than the critical angle at the film-substrate interface and light is totally internally reflected at both upper and lower surface interfaces.

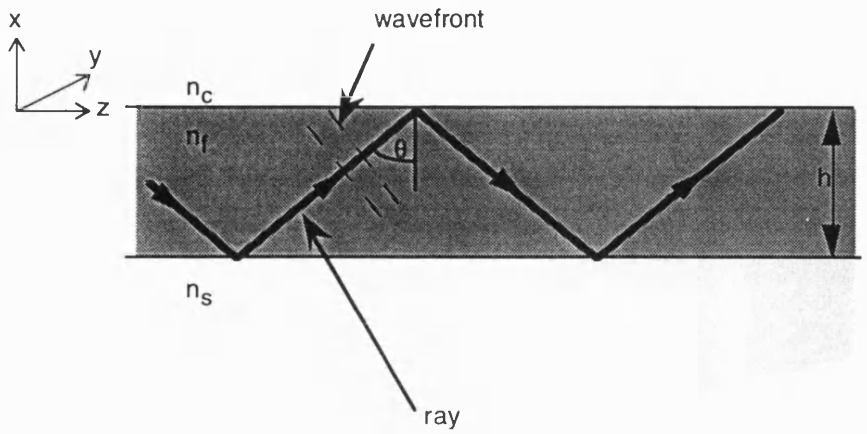

Figure 2.1. Cross-section of a planar waveguide showing a guided mode. A light wave in a waveguide mode can be considered as a plane wave, the wavefront vector of which propagates along a zigzag path in the film.

The superposition of plane waves is an approximate, convenient, and easily visualised representation of guiding. Electromagnetic theory, through Maxwell's equations and the wave equation, results in a more accurate yet cumbersome representation. For the purpose of this thesis, the first model, with a few amendments will suffice.

Assume that light in the guide propagates in the z-direction, confinement occurs in the x-direction, and that the guide structure and light are uniform in the y direction. Guiding can be pictured as two superimposed uniform plane waves, with plane normals which follow a zig-zag path (shown in figure 2.1.) having been internally reflected at the film boundaries. Consider monochromatic, coherent waves with angular frequency, ω, wavelength, λ, which travel with a wavevector kn_f in the direction of the normal, where k is the free-space wave vector and is given by

$$k = \frac{2\pi}{\lambda} = \frac{\omega}{c} \qquad 2.1\text{-}3$$

c being the velocity of light.

A planar guide supports transverse electric (TE) modes, or transverse magnetic modes (TM). In a TE mode, the electric field is parallel to the junction between the high refractive index and low refractive index layers. The TM mode in a waveguide

is characterised by the magnetic field which is parallel to the junction and the electric field which is perpendicular to the junction.

The fields of the waves have the form $\exp(ikn_f(\pm\cos\theta + z\sin\theta))$.
For a guided mode the propagation constant β is given by

$$\beta = \frac{\omega}{v_p} = kn_f\sin\theta \qquad 2.1\text{-}4$$

where v_p is the phase velocity in the medium.
An effective index N can be defined as

$$N = \frac{\beta}{k} = n_f\sin\theta \qquad \text{where } n_c<N<n_f \qquad 2.1\text{-}5$$

Not all angles are allowed, only a discrete set of angles (or none) lead to a self-consistent picture that corresponds to 'guided modes'. For self consistency the sum of all phase shifts that occur from one boundary to the other must be multiples of 2π. For a film thickness h, one finds a phase shift of $kn_fh\cos\theta$ on first transverse passage through film, a phase shift, $-2\phi_c$, on total internal reflection from film superstrate interface, another $kn_fh\cos\theta$ on downward transverse, and a phase shift $-2\phi_s$, on total internal reflection from the film-substrate boundary.

Thus the self-consistency condition is

$$2kn_fh\cos\theta - 2\phi_s - 2\phi_c = 2m\pi \quad \text{where m=0,1,2...} \qquad 2.1\text{-}6$$

The solutions to 2.1-6 for ϕ_S and ϕ_C, for TE and TM polarisations are given (by Born and Wolf[3] in the theory of total reflection) by the Fresnel formulae

$$\tan\phi_{s,cTE} = \frac{\sqrt{n_f^2\sin^2\theta_f - n_{s,c}^2}}{n_f\cos\theta}$$
$$\tan\phi_{s,cTM} = \frac{n_f^2}{n_{s,c}^2}\frac{\sqrt{n_f^2\sin^2\theta_f - n_{s,c}^2}}{n_f\cos\theta_f} \qquad 2.1\text{-}7$$

Equation 2.1-6 is the dispersion relation of the guide. It gives β as a function of ω and film thickness and must be solved numerically.

For TE modes, substituting for ϕ_s and ϕ_c in equation 2.1-6, and using $\cos\theta = \sqrt{1-\sin^2\theta}$ and 2.1-5

$$kh\left(n_f^2 - N^2\right)^{\frac{1}{2}} = m\pi + \tan^{-1}\left(\frac{N^2 - n_s^2}{n_f^2 - N^2}\right)^{\frac{1}{2}} + \tan^{-1}\left(\frac{N^2 - n_c^2}{n_f^2 - N^2}\right)^{\frac{1}{2}}$$

where m=0,1,2... 2.1-8

To make results more broadly applicable, normalisations which combine several guide parameters are introduced.

A normalised frequency and film thickness V are defined by

$$V = kh\sqrt{n_f^2 - n_s^2} \qquad 2.1\text{-}9$$

The normalised guide index is

$$b = \left(\frac{N^2 - n_s^2}{n_f^2 - n_s^2}\right) \qquad 2.1\text{-}10$$

where b is zero at frequency cut off and approaches unity away from it.

The asymmetry of the waveguide structure is defined by

$$a = \left(\frac{n_s^2 - n_c^2}{n_f^2 - n_s^2}\right) \qquad 2.1\text{-}11$$

where a applies to TE modes only and ranges from zero for perfect symmetry $(n_s = n_c \neq n_f)$ to infinity for strong asymmetry $(n_s \neq n_c)$ and $(n_s \approx n_f)$.
Substituting 2.1-10, 2.1-11 and 2.1-12 into equation 2.1-9 and simplifying

$$V(1-b)^{\frac{1}{2}} = m\pi + \tan^{-1}\left(\frac{b}{1-b}\right)^{\frac{1}{2}} + \tan^{-1}\left(\frac{b+a}{1-b}\right)^{\frac{1}{2}} \qquad 2.1\text{-}12$$

the cut off frequency when m and b=0 is

$$V_o = \tan^{-1}\sqrt{a} \qquad 2.1\text{-}13$$

using 2.1-9

$$\left(\frac{h}{\lambda}\right)=\frac{1}{2\pi}\left(n_f^2-n_s^2\right)^{-1/2}\tan^{-1}\sqrt{a} \qquad 2.1\text{-}14$$

The cut off frequency v_m of the m^{th} mode is

$$V_m = V_o + m\pi \qquad 2.1\text{-}15$$

An estimate of the number of guided modes allowed in the waveguide is

$$M=\frac{2h}{\lambda}\left(n_f^2-n_s^2\right)^{1/2} \qquad 2.1\text{-}16$$

The plane wave internal reflection picture has to be adapted to account for field penetration in the substrate and superstrate. This results in an effective waveguide thickness larger than h, and a confinement of guided light that is not complete and is given by a confinement factor. A light ray must be defined as the direction of the Poynting vector. The relation between the wave normal and ray is essentially the spatial analogue of the relation between the phase velocity and group velocity.

The Goos-Hänchen shift occurs on total internal reflection; the reflected ray is shifted laterally relative to the incident ray. To obtain a zig-zag ray model of light, a Goos-Hänchen shift has to be added at both interfaces. As a consequence of ray penetration, the effective thickness is

$$h_{eff} = h + x_s + x_c \qquad 2.1\text{-}17$$

where x_s and x_c are the penetration depths in superstrate and substrate. The guided light spreads somewhat into the substrate and superstrate and is confined to a thickness, h_{eff}. By solving the wave equation for a guided mode, the fraction of light which is actually confined within the guide can be calculated. This confinement factor D is approximately equal to

$$D = kh_{eff}(n_f^2 - n_s^2)^{1/2} \qquad 2.1\text{-}18$$

2.2. Active waveguides

The optical properties of a dielectric material can be described in two ways:
- a microscopic picture giving the probability of all transitions and scattering processes involving photons and atoms of the material.
- a macroscopic picture giving the complex optical constants as a function of light frequency.

In sections 2.2.1. and 2.2.2. the microscopic model is developed. Starting from the electronic transitions between two levels, the conditions necessary for gain are established and an expression for gain in terms of level populations is derived.
In section 2.2.3., using a macroscopic model, absorption and gain are described in terms of complex optical constants. An expression for gain in terms of the imaginary part of the electric susceptibility is derived. The Kramers-Kronig relations linking the real and imaginary parts of the electric susceptibility are also given.

2.2.1. Electronic transitions

Consider a two level system with a total of N atoms per unit volume, N_1 in level 1 the ground state (Energy E_1), and N_2 in level 2 the excited state (Energy E_2). Three transitions[4] between the two levels are possible:
-absorption of a photon of frequency $\nu=(E_2 - E_1)/h$. The transition rate from level 1 to level 2 is $B_{12} N_1 N(\nu)\Delta\nu$ where B_{12} is the Einstein coefficient of absorption and $N(\nu)\Delta\nu$ is the number of photons per unit volume in the frequency interval ν, $\nu+\Delta\nu$.
-spontaneous emission of a photon of frequency ν. The spontaneous electron transition rate from levels 2 to 1 is $A_{21}N_2$, where A_{21} is the Einstein coefficient of spontaneous emission.
-stimulated emission of a photon as above, in phase with a stimulating signal photon of same frequency. The stimulated electron transition rate from levels 2 to 1 is $B_{21}N_2N(\nu)\Delta\nu$ where B_{21} is the Einstein coefficient of stimulated emission .

At thermal equilibrium

$$\frac{N_2}{N_1} = e^{-h\nu/kT} \qquad 2.2.1\text{-}1$$

and

$$A_{21}N_2\Delta\nu + B_{21}N_2N(\upsilon)\Delta\nu = B_{12}N_1N(\upsilon)\Delta\nu \qquad 2.2.1\text{-}2$$

The photon density in thermal equilibrium is given by the blackbody distribution at temperature T

$$N(\upsilon) = \frac{8\pi n^3\upsilon^2}{c^3}\frac{1}{\left(e^{h\nu/kT}-1\right)} \qquad 2.2.1\text{-}3$$

where n is the refractive index of the material.
Using equations 2.2-1, 2.2-2 and 2.2-3, the Einstein relations are obtained

$$B_{21} = B_{12}$$
$$A_{21} = \frac{B_{21}8\pi n^3\nu^2}{c^3} \qquad 2.2.1\text{-}4$$

2.2.2. Absorption and gain

Consider a collimated beam of monochromatic radiation passing through an absorbing medium, see figure 2.2., and assume that the medium has only a single radiation transition between the levels E_1 and E_2.

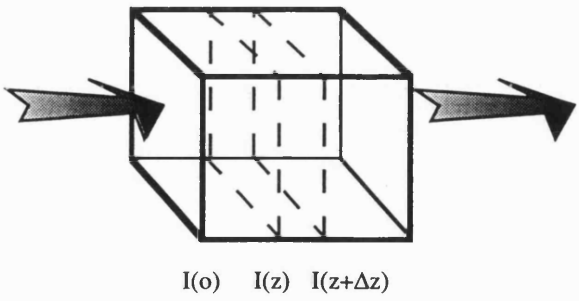

Figure 2.2. Passage of radiation through an absorbing material.

For a homogeneous medium, the change in intensity with distance z, defined as the number of photons flowing through a unit area per unit time, is

$$\frac{dI}{dz} = \gamma I \qquad 2.2.2\text{-}1$$

where γ is the gain coefficient if positive, and the absorption coefficient if negative. The solution is

$$I(z) = I(0)e^{\gamma z} \qquad 2.2.2\text{-}2$$

Ignoring spontaneous emission, the change in photon density per second is

$$\frac{dN(\nu)}{dt} = B_{21}(N_2 - N_1)N(\nu) \qquad 2.2.2\text{-}3$$

The intensity of the light beam is related to the photon density by $N(\upsilon) = \frac{nI}{c}$, equation 2.2.2-3 becomes

$$\frac{dI}{dt} = B_{21}(N_2 - N_1)I \qquad 2.2.2\text{-}4$$

The change in intensity with z can be expressed as

$$\frac{dI}{dz} = \frac{dI}{dt}\frac{dt}{dz} = \frac{B_{21}(N_2 - N_1)In}{c} \qquad 2.2.2\text{-}5$$

Comparing 2.2.2-5 and 2.2.2-1, the gain coeficient is

$$\gamma = B_{21}(N_2 - N_1)\frac{n}{c} \qquad 2.2.2\text{-}6$$

Normally, $N_1 > N_2$, γ is negative and absorption occurs. The material will exhibit gain if the stimulated emission rate exceeds the absorption rate, $N_2 > N_1$; that is when γ is positive. This condition (positive γ), called population inversion, is achieved by pumping ground state electrons into the excited state. In order to get an excited atomic population greater than half the total atomic population, a third level is required. The pump excitation raises ground level atoms to a higher level E_3,

these atoms decay rapidly to the level E_2. The metastable level, E_2, has a slow radiative decay lifetime to the ground state and thus achieves population inversion. The Er^{3+} ion energy level is often simplified to a three level system[5] such as the one described above. This three level system is a good model for glasses with low dopant concentrations. It is not accurate for highly doped glasses and so an 8 level system is used in the model discussed in chapter 4. Nonetheless, the basic principles of absorption, excitation, emission and gain are the same.

2.2.3. Electric susceptibility

Absorption and gain can also be described in terms of the imaginary part of the electric susceptibility χ'' of the propagation medium. The value of the optical constants n and k depend on the frequency of the electromagnetic wave. The real and imaginary part of these optical constants and of the electric susceptibility are not independent of each other. The equations linking the real and imaginary parts are known as the Kramers-Kronig relations. It can be shown that $\chi'(\omega)$ is the Hilbert transform of $\chi''(\omega)$.

Dielectrics whose polarisation, **P**, is directly proportional and in the same direction as the electric field, **E**, are linear and isotropic. The complex polarisation of a homogeneous, linear, and isotropic medium is

$$\mathbf{P} = \varepsilon_o \chi_E \mathbf{E} = \varepsilon_o (\chi' - i\chi'')\mathbf{E} \qquad 2.2.3\text{-}1$$

The electric displacement, **D**, is

$$\mathbf{D} = \varepsilon\mathbf{E} + \mathbf{P} = \varepsilon\left(1 + \frac{\varepsilon_0}{\varepsilon}\chi\right)\mathbf{E} = \varepsilon'\mathbf{E} \qquad 2.2.3\text{-}2$$

ε_0 and ε are the electric constants of free space and of the medium of interest respectively. The complex electric constant ε' is

$$\varepsilon'(\omega) = \varepsilon\left(1 + \frac{\varepsilon_0}{\varepsilon}\chi(\omega)\right) \qquad 2.2.3\text{-}3$$

The effect of the atomic transition has been accounted for by modifying ε into a complex electric constant . The refractive index far from resonance is

$$n^2 = \frac{\varepsilon}{\varepsilon_0} \qquad 2.2.3\text{-}4$$

and k, the wave vector, is

$$k = \omega\sqrt{\mu\varepsilon}$$

and μ is the magnetic constant.

The complex wave vector is

$$k' = \omega\sqrt{\mu\varepsilon'} = k\left(1+\frac{\varepsilon_0}{2\varepsilon}\chi\right) \qquad |\chi| \prec\prec 1 \qquad 2.2.3\text{-}5$$

Expressing χ in terms of its real and imaginary components $\chi = \chi' - i\chi''$

$$k' = k\left[1+\frac{\chi'(\omega)}{2n^2}\right] - \frac{ik\chi''(\omega)}{2n^2} \qquad 2.2.3\text{-}6$$

A plane wave propagating in a medium has the form

$$E(z,t) = \mathrm{Re}\left[Ee^{i\left(\omega t - k' z\right)}\right] = \mathrm{Re}\left[Ee^{i\omega t - i(k+\Delta k)+\left(\gamma/2\right)z}\right] \qquad 2.2.3\text{-}7$$

The result of the atomic polarisation is thus to change the phase delay per unit length from k to k+Δk, where

$$\Delta k = \frac{k\chi'(\omega)}{2n^2} \qquad 2.2.3\text{-}8$$

as well as to cause the amplitude to vary exponentially with distance according to $e^{(\gamma/2)z}$, where

$$\gamma(\omega) = -\frac{k\chi''(\omega)}{n^2} \qquad 2.2.3\text{-}9$$

This is the gain coefficient expressed in terms of the imaginary part of the electric susceptibility.

According to a theorem of complex variables, the real and imaginary parts of a complex function that has no poles in the lower z plane are related by the Hilbert transform. When applied to the complex electric susceptibility, these transforms for the case of $\chi(\infty) = 0$ are

$$\chi'(\omega) = \frac{1}{\pi}\text{P.V.}\int_{-\infty}^{\infty}\frac{\chi''(\omega')}{\omega'-\omega}d\omega'$$
$$\chi''(\omega) = -\frac{1}{\pi}\text{P.V.}\int_{-\infty}^{\infty}\frac{\chi'(\omega')}{\omega'-\omega}d\omega' \qquad 2.2.3\text{-}10$$

where P.V. stands for the Cauchy principal value of the integral that follows.
The equations 2.2.3-10 are known as the Kramers-Kronig relations.

Conclusions

The equations derived in this chapter are used in different sections of the thesis. In the section 5.6.1 on prism coupling, the effective index equation is calculated from the angle θ_4 of the mode lines. Equation 2.1-8 is solved numerically to calculate the refractive index and the film thickness from the effective index.

The rate equations discussed in section 4.2, use the Einstein coefficients, equation 2.2.1-4, and the concepts introduced in section 2.2 for the 2 level system. The definition of the gain coefficient, (equation 2.2.2-6) slightly modified by accounting for the cross-sections of the levels (see section 3.4), is applied to the erbium amplifier in equation 4.3-1. The expression for the gain coefficient in terms of the imaginary part of the electric susceptibility (equation 2.2.3-9) is used in equation 4.3.2. The Kramers-Kronig relations (equation 2.2.3-10) and the expression for the electric constant 2.2.3-3, are applied in section 4.3 to solve the wave equation.

References

1. T. Tamir, 'Guided wave optoelectronics', T. Tamir (ed.) Springer-Verlag (1988).

2. P.K. Tien, 'Light waves in thin films and integrated optics', Appl. Opt. **10**, pp.2395-2413 (1971).

3. M. Born and E. Wolf, 'Principles of Optics', Pergamon, New York (1970).

4. A. Yariv, 'Quantum electronics', Wiley, 3rd Ed. (1989).

5. P. Urquhart, 'Review of rare-earth doped fibre lasers and amplifiers,' IEE Proc., J. Optoelectronics, **135**, pp.385-407 (1988).

Chapter 3: Properties and structure of rare-earth doped glass

Introduction

Research on lasers and excited states of rare-earths started in the sixties. A review of this activity is given by Reisfeld and Jørgensen[1]. Rare-earth ions can be used as the active medium of a laser or amplifier because the position of their fluorescence and absorption spectra is not strongly effected by external fields. This characteristic is due to their distinctive electron configuration.

Interest in the Er^{3+}-ion has recently been rekindled because its main transition, at 1535nm, falls into the lossless window for fibre-optic communications[2]. The long lifetime of the metastable state permits high population inversions to be achieved under steady state conditions and low pump powers. Erbium doped fibre amplifiers (EDFA's) have absorption bands at 532nm, 807nm, 980nm, and 1547nm, all of which have been successfully used as pump levels.

EDFA's technology has developed fast and successfully, there are nonetheless inherent limitations in the use of fibres due to their cylindrical geometry, length and the way in which they are fabricated. Short active planar waveguides with similar optical characteristics are attractive for their tremendous potential in integrated optics. Lithography techniques may be used to fabricate power splitters such as Y-junctions, single mode trees[3], and star couplers[4].

In this chapter the foundation stones for an understanding of rare-earths as glass dopants are laid. The electronic structure, discussed in section 3.1, is responsible for the distinctive optical characteristics of each rare-earth. The energy levels of the Er^{3+}-ion and the Russell Saunders notation are introduced in section 3.2. The effect of broadening and transition rates on the magnitude and shape of cross sections are illustrated in 3.3 and 3.4.

In the last part of the chapter an explanation for clustering and effect of the codopants, based on the co-ordination number size and charge of the various glass constituents is given. Structural models of Er^{3+}-doped silicates are shown. The change of the Er^{3+}-site due to the addition of Al is explained.

3.1. Rare-earths

The rare-earths, or lanthanides, are a set of 15 elements occupying the penultimate row of the periodic table. The name and chemical symbol of the lanthanide series is shown in table 3.1. Ionisation of the rare-earths usually takes place to form a trivalent state. All rare-earths have the same outer electronic structure of $5s^2 5p^2 6s^2$. The number of electrons occupying the inner 4f shell dictates their optical characteristics.

Rare-earth	Chemical symbol
lanthanum	^{57}La
cerium	^{58}Ce
praseodymium	^{59}Pr
neodymium	^{60}Nd
promethium	^{61}Pm
samarium	^{62}Sm
europium	^{63}Eu
gadolinium	^{64}Gd
terbium	^{65}Tb
dysprosium	^{66}Dy
holmium	^{67}Ho
erbium	^{68}Er
thulium	^{69}Tm
ytterbium	^{70}Yb
lutetium	^{71}Lu

Table 3.1. The lanthanide series showing atomic number.

The two 6s electrons and one of the 4f electrons, are removed from Er to form the Er^{3+}-ion. However, the outer 5s and 5p shells remain intact. Consequently the remaining 4f electrons are partially shielded from perturbation by external fields. The electronic configuration of the Er^{3+}-ion, and thus the position of its absorption and emission bands, are not strongly affected by the host.

3.2. Energy levels of Er^{3+}-ion

The electronic structure of rare-earth ions is dominated by electron-electron interaction, with spin orbit next in importance. These interactions produce the free ion J multiplets. The host has the least influence on the electronic structure. However, glass composition has an important effect on the magnitude and shape of the bands.

The electron-electron interaction splits the single-electron configuration into levels described by the quantum numbers, L and S, where L is the total orbital quantum number, and S is the total spin quantum number. The allowed values of L, L=0,1,2,3,.., are expressed by the capital letters S, P, D, F, G, H, I, respectively.

Spin orbit interaction splits the levels into multiplets by causing the energy of a state to be dependent on the total momentum quantum number J, where J=(L+S), (L+S-1), (L+S-2), (L-S). The level notation is based on the Russell-Saunders coupling of atomic physics[5], and the symbol characterising each level is $^{2S+1}L_J$.

The maximum capacity of the f shell is 14, the f shell of the Er^{3+} ion contains 11 electrons and 3 vacancies. It is convenient to calculate the electronic configuration using the 3 vacancies rather than the 11 electrons. The ground state of an atom is the state with the highest value of S and of L, in this order. For the ground state of Er^{3+}, the sum of the individual spins for each vacancy is $S=s_1+s_2+s_3=1/2+1/2+1/2=3/2$. The highest value of L compatible with the exclusion principle is $L=l_1+l_2+l_3=1+2+3=6$. According to Hund's rule, if an atom has more electrons than vacancies in the valence shell, the ground state has the highest value of J, where J=L+S=15/2. The ground state is $^4I_{15/2}$, the other levels of the ^4I multiplet are in ascending energy, J=13/2, 11/2, and 9/2.

For the complete configuration of Er^{3+}, the possible values of L=1, 2, 3, 4, 5, 6, and s=1/2 and 3/2, all total momentum quantum numbers can be calculated. There is a certain amount of mixing of the multiplets of close levels; the result is shown in the energy level diagram shown in figure 3.1. The energy levels are labelled by their Russell-Saunders SLJ term.

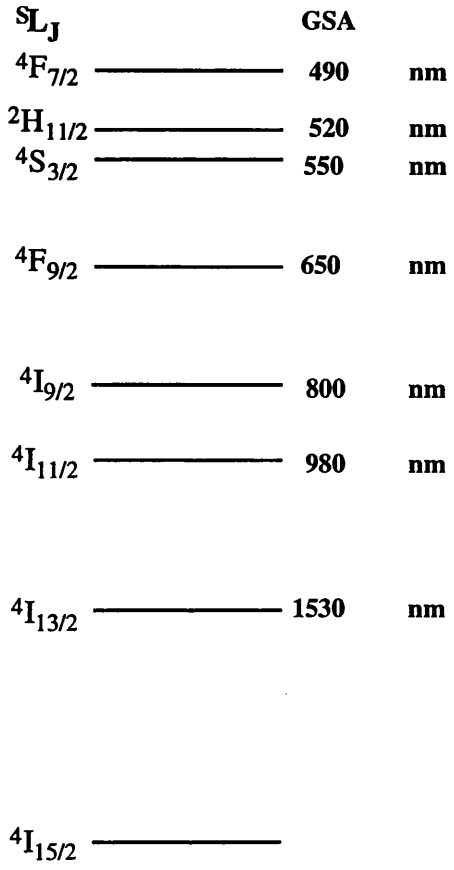

Figure 3.1. Energy levels of Er^{3+} labelled with dominant Russell-Saunders $^{S}L_J$ term. For each state, the GSA column lists the wavelength of the excited-state absorption terminating on it.

The first four excited levels have all been successfully used as pump levels. The most efficient pump is in the 980nm range, corresponding to the third, $^4I_{11/2}$, level. An ion in the ground state is excited, by a pump at 980nm, to the third level. It then decays non radiatively to the $^4I_{13/2}$ metastable state. This is the initial level for the transition producing gain at 1500nm, any process removing ions from this state other than stimulated emission into the signal mode, decreases amplifier efficiency. These processes will be discussed in detail in section 4.1 of chapter 4.

3.3. Broadening mechanisms and transition rates

The host can change the relative position of levels slightly, and can also produce variations in transition strengths. The effect of the host on the ion can be represented by a potential field which can be expanded in a spherical harmonic series[6]. Only the even terms of this expansion produce shifts in the energy levels.

The odd terms produce a mixing of the 5d wave functions with 4f wave functions, thus permitting the otherwise forbidden electric-dipole transitions between the 4f levels. Individual dopant ions can occupy several different sites in a multi-component glass, the disorder in the even terms leads to a distribution of energies for a given Stark component and produces inhomogeneous broadening of the emission and absorption spectra. The disorder in the odd terms produces variations in transition strengths between a given pair of components. The transitions are also homogeneously broadened through dephasing processes. These processes are dominated by electron-phonon interactions and are therefore strongly temperature dependent.

The J+1/2 degeneracies corresponding to the maximum number of energy levels, are $g_2=7$ for the $^4I_{13/2}$ upper level manifold and $g_1=8$ for the $^4I_{15/2}$ lower level manifold. At low temperatures, most of the expected 7 Stark levels of $^4I_{13/2}$ and 8 components of the $^4I_{15/2}$ ground state are resolved[7]. At room temperature, even the highest components have some thermal occupation, and the emission and absorption spectra are composites of 56 largely unresolved Stark transitions. The magnitude and shape of the absorption and emission cross-section spectra are determined by the crystal potential field together with the homogeneous and inhomogeneous broadening. The relative significance of the two broadening mechanisms has important implications for the gain saturation properties of an amplifier.

In addition to the host dependent electric-dipole contribution, the $^4I_{13/2}$-$^4I_{15/2}$ transition has considerable magnetic dipole strength which is insensitive to the host material.

An empirical technique for the analysis of rare-earth transitions was developed by Judd[8] and Ofelt.[9] The model uses the approximation: the energy range occupied by opposite parity states is small compared to the separation from the $(4f)^n$ multiplets. The spectrally integrated strength of the transition between a given pair of J multiplets is then determined by the empirical parameters and the appropriate reduced matrix elements. All the host dependence is contained in the three intensity parameters which are found for a given dopant material combination from a least squares fit of the absorption spectrum. Judd-Ofelt analysis is accurate to 10-15% and provides linestrengths of transitions for which direct measurements are difficult.

It applies only to the integrated transition strengths, and provides no spectral information.

3.4. Absorption and stimulated emission cross sections

The host has a strong effect on magnitude and shape of the absorption and emission cross-section. Two diagrams, figure 3.2 and figure 3.3 taken from Miniscalco[6] illustrate how glass composition modifies spectra.

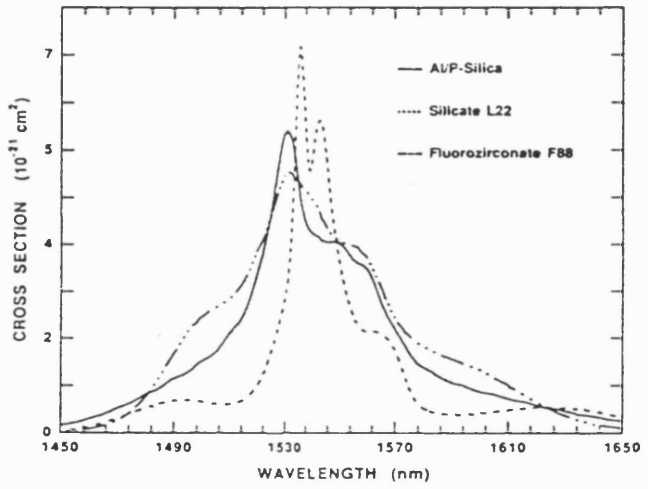

Figure 3.2. 1500nm absorption cross-section spectra for different glass types illustrating the variation in magnitude and shape. (ref. 6)

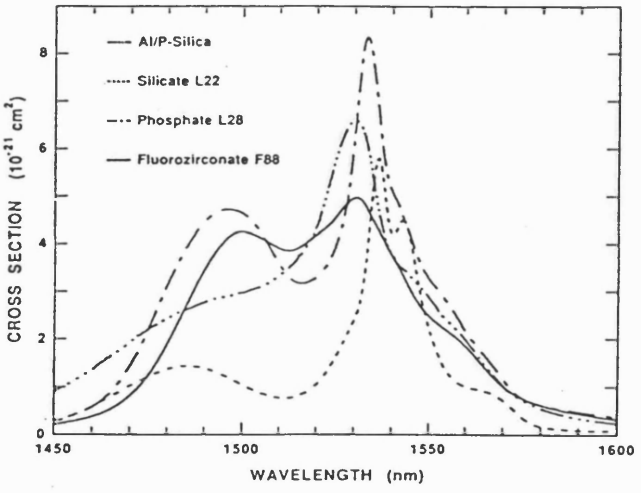

Figure 3.3. 1500nm stimulated emission cross-section spectra for different glass types. (ref. 6)

Note that the silicate spectra are narrow and sharp, whereas the Al/P silica spectra are much broader. The addition of Al or P increases the number of possible sites of the Er^{3+}-ion in the host which results in greater variation of transitions and broadening of the spectra. The differences in spectra between glasses are caused by changes both in the crystal field splittings and in the intensity of the Stark transitions. The integrated absorption cross-section is defined as

$$K_a = \int \sigma_{12}(\nu) d\nu \qquad 3.4\text{-}1$$

where σ_{12} is the absorption cross section.
The host can affect K_a by a factor 2. Silicates have the lowest value of K_a, Al/P SiO_2 has an unusually high K_a value.

For highly inverted 3 level and four level lasers and amplifiers, the maximum gain occurs at the peak of the stimulated emission cross-section spectrum. The peak cross-section is determined by the spectral shape as well as the integrated cross-section. In order to account for broadening mechanisms and Stark splitting of the levels, the gain coefficient must be expressed in terms of the integrated emission cross-section.

The quantities $\frac{B_{21}n}{c}$ and $\frac{B_{12}n}{c}$ (see section 2.2.2) are the stimulated emission and absorption cross-sections respectively (σ_{21} and σ_{12}) and have the dimensions of area. The derivation, in chapter 2, of the Einstein relations for levels 1 and 2 is oversimplified, and this is reflected in the fact that the cross-sections are slightly different. For the Er^{3+}-ion, the gain coefficient in terms of cross-sections is

$$\gamma = \sigma_{21}(\nu) n_2 - \sigma_{12}(\nu) n_1 \qquad 3.4\text{-}2$$

For high population inversions, the population of the ground state is negligible and the second term of 3.5-2 goes to zero.

The relationship between σ_{21} and A_{21} is best seen by referring to the spontaneous lifetime τ_{sp} of level $^4I_{13/2}$ which is defined by

$$\frac{1}{\tau_{sp}} = \int A_{21}(\nu)d\nu$$
$$\frac{1}{\tau_{sp}} = \int \frac{8\pi\nu^2 n^3}{c^3} B_{21}(\nu)d\nu = \int \frac{8\pi\nu^2 n^2}{c^2} \sigma_{21}(\nu)d\nu \qquad 3.4\text{-}3$$

where ν is the photon frequency.

The peak absorption and emission generally lie within 1nm of each other; indicating that the same pair of Stark components dominates both emission and absorption. Low temperature measurements have revealed these to be the lowest level of each manifold.

3.5. Solubility of rare-earths in silica

Pure silica is an unusual host for rare-earths, allowing only low concentrations to dissolve. In the rigid silica network, rare-earth ions which require large coordination numbers cluster in order to share non bridging oxygens. The addition of Al has been found to improve the solubility of rare-earth ions in silica and thus reduce clustering. Al increases the waveguide refractive index step, and modifies the spectra, changing the sharp double peaked Er^{3+}-SiO_2 spectrum into a broader wider spectrum which is similar to that of multicomponent glasses. It was initially thought that the solubility limitations might be the dominant constraint for producing Er-doped silica. However, the results presented in chapter 6 demonstrated that high Er concentrations can readily be incorporated into a PECVD silica. Gain is limited by the formation of ion pairs. The addition of codopants eliminates large clusters, but may just reduce rather than eliminate ion pair formation.

3.6. Classification of oxides in glasses

In order to analyse multicomponent glasses, it is helpful to look at the characteristics of the oxides which are the components of these glasses. Certain

elements are glass-formers in combination with oxygen, while others are not. Silicon is a glass-former, whereas erbium in combination with oxygen, crystallises. Glass-forming oxides[10] contain elements in which the cation is small and highly charged. B, Si, Ge, P, and As are the most important glass-formers, where Al is a typical intermediate. The decisive factor for determining whether an element is a glass former is the polarisation of the surrounding oxygen ions by the strong electric field of the small and highly charged cation. A glass forming cation has a homopolar, and therefore directional bond with the oxygen ions. The small size and high charge of the cation favours the formation of glassy oxides.

Element	Valence Z	a/Å	Z/a^2 ref.11	Group
Si	+4	0.42	22.7	Glass-former
P	+5	0.35	40.81	Glass-former
P	+3	0.44	15.49	Intermediate
Al	+3	0.51	11.53	Intermediate
Er	+3	0.89	3.787	Network Modifier
Na	+1	0.97	1.06	Network Modifier

Table 3.2. Classification of oxides as glass-formers and network modifiers, Z is the ionic charge and a the distance between centres of the cation and the oxygen ion in the crystal.

It is possible to divide oxides into three groups: glass-former, intermediate and modifier by listing values of Z/a^2 in descending order, where Z is the ionic charge and a the distance between centres of the cation and the oxygen ion in the crystal. Table 3.2 shows the ions of interest to the project, and sodium a commonly used network modifier, in descending order of Z/a^2 values. Erbium is clearly a network modifier. These criteria for glass-forming effectiveness of particular oxides break down for unusual structures.

There is a sharp difference in structure between a solid and its liquid, this difference being mainly in the range over which order persists, not in the kind of order. It has been empirically observed[12] that typical glass-formers have relatively low co-ordination numbers in the liquid and solid states, and that non-glass formers have high co-ordination numbers. Generally, the co-ordination numbers do not change

appreciably when a crystal melts. In the CRC Chemical Handbook of Chemistry and Physics[11] a co-ordination number of six is given for erbium oxide; this is typical for non-glass formers. Most of the crystal M_2O_3 are oxides of trivalent metals[13]. Their structures are ionic and do not generally involve strong polarisation. The structure of Er_2O_3 is cubic, the unit cell contains 16 molecules and thus 80 atoms. The cubic lattice parameter, a, of Er_2O_3 is 10.54Å. The erbium ion can exist in three coordinations 6, 8 and 12. K. Arai's[14] spectra show 5 and 7 stark split energy levels; this is an indication that in glass erbium can sit in at least two configurations. Al_2O_3 can exist as a hexagonal structure and a rhombic one. SiO_2 forms covalent structures which can be crystalline (hexagonal quartz), or amorphous.

3.7. Erbium sites in silicates

Pure silica can incorporate only small amounts of rare-earths before a non uniform dopant distribution which reduces gain appears. The addition of codopants such as the alkali metals, aluminium and phosphorous, have been demonstrated to change the glass matrix making high concentrations of Er^{3+}-doped silicate glasses viable. Rare-earths can be distributed in different ways within a glass matrix: a random distribution, a random distribution of rare-earth ion pairs and rare-earth clusters, or microcrystals. The effect of distribution on gain is discussed in detail in chapter 4. Clusters quench gain and must be avoided. The addition of Al, P and non-bridging oxygens can be used to eliminate microscopic clustering, however these apparently uniform glasses may have a significant proportion of rare earths in ion pairs[15]. When only one type of rare-earth dopant is present, the rapidly interacting ions in the pair do not contribute to gain, whilst randomly distributed singly excited ions are efficient. Ion-ion interactions are discussed in detail in chapter 4.

The two points addressed here are:

1) What are the possible rare-earth sites in glass for the random, ion pair, and clustered distributions ?

2) How does the addition of a codopant change the glass matrix?

In order to get a tentative picture of the short range order around Er^{3+}-ions, low temperature absorption and photoluminescence spectra of the glasses need to be analysed. From the features of the spectra, and the similarities and differences

between different glass compositions, it is possible to determine the Stark splitting of the energy levels and their intensity. The observed change in band position or in band intensity, is related to a difference in the near neighbour environment of the rare-earth and thus to a difference in the symmetry of the site. The environment around the rare-earth can be varied by adding a codopant.

3.7.1. Structural models

Robinson[16,17] looked at the low temperature $^4I_{15/2}$-$^4S_{3/2}$ absorption spectra of a series of binary alkali silicate glasses doped with Er^{3+} to demonstrate the presence of four different sites for the Er^{3+} in these glasses. Tentative models for the structures are given.

1) The A site is the most common and appears in all glasses regardless of the alkali ion size. In this site, the Er^{3+} is six fold coordinated, in a near octahedral arrangement. Figure 3.4 shows a schematic drawing of the A site. Three charge compensating monovalent alkali ions are required.

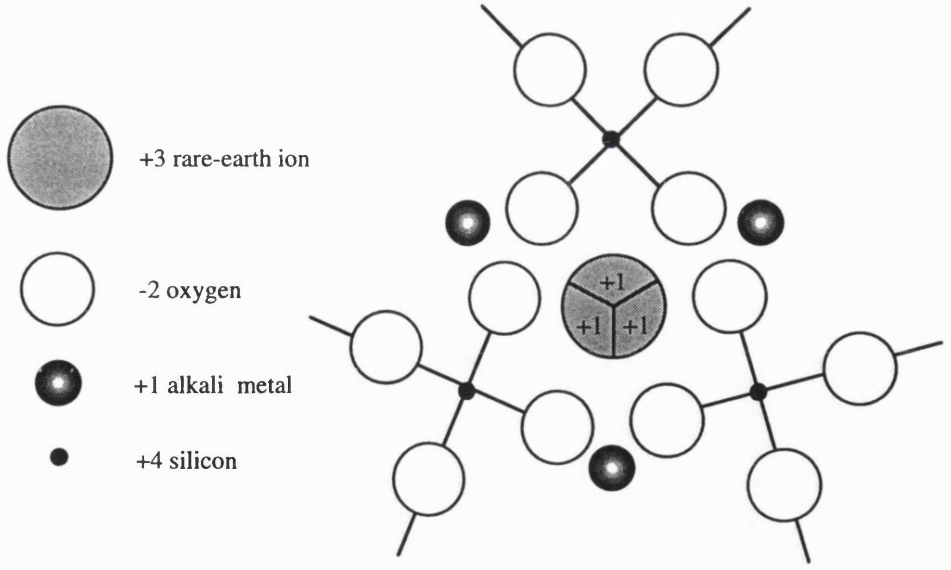

Figure 3.4. A schematic representation of the sixfold coordinated near octahedral site for Er^{3+}. Note the presence of the three monovalent alkali ions necessary for charge compensation.

2) The B site, characteristic of binary Li and Na glasses, is an arrangement in which the rare-earths group together. The concentration of alkali ions is lower for the B

site than the A site. Er^{3+}, with its high cationic field strength, requires a high co-ordination number of non-bridging oxygens to screen the electronic charge of the cation. The number of alkali ions is insufficient for charge compensation, therefore another source must be found. The additional positive charge may be obtained by either grouping the tri-positive rare-earth ions together, or by introducing bridging oxygens next to the rare-earth. An example of an Er^{3+}-ion group around a silica tetrahedron is shown in figure 3.5. Each one of the rare-earth ions is shared by 3 $SiO_{4/2}$ tetrahedra. One of the rare-earths in figure 3.5 can be replaced by a monovalent alkali ion, or one of the oxygens in the tetrahedra could be replaced by a bridging oxygen (equivalent to adding a positive charge).

Furthermore, charge compensation does not necessarily occur in the immediate vicinity of a silica tetrahedron, but could be balanced by an adjacent one. Thus variations of the three models can result in a large number of situations. Robinson's research was prior to Er-doped fibre amplifiers, thus there is no mention of fluorescence quenching. However the close proximity of Er^{3+}-ions in the B model is an indication that this glass would exhibit poor gain. The close proximity of the rare-earth ions in the B model, result in a fast interaction between excited ions which can be deleterious to gain if the ions are of the same species. The ion-pairs (see chapters 4 and 7) responsible for strong ion-ion interactions are in the close proximity of the B site.

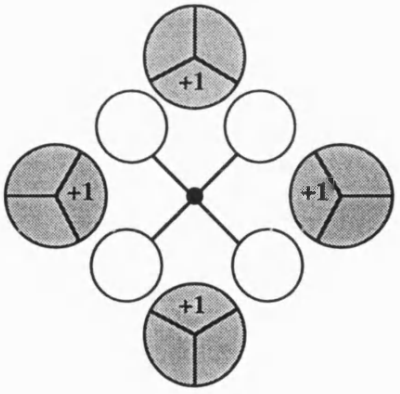

Figure 3.5. A non-bridging silicate tetrahedron is surrounded by four rare-earth ions.

3) The C site is present in K, Rb and Cs silicate glasses. Most of the peaks in its spectrum coincide with those for Er^{3+} in Er_2O_3[18]. This similarity suggests that this site may be similar to that of Er^{3+} in Er_2O_3. The Er^{3+}-ions in Er_2O_3 do not

fluoresce, thus the C structure has microcrystallisation which results in fluorescence quenching.

4) The D site is similar to the A site, the discrepancy being due to the difference in size between the network modifier ions. In the D site, Na and Li are replaced by the large alkali ions K, Rb, and Cs. Non-uniform dopant distribution, similar to that of the B structure, can occur in the D site if one of the alkali ions in figure 3.4 is replaced by an Er^{3+}-ion.

More recently, Marcus and Polman[19] performed extended X-ray absorption fine structure (EXAFS) and photoluminescence (PL) measurements on three different Er^{3+}-doped glasses: silica and sodium silicate doped with Er^{3+} in the molten phase, and silica doped by MeV ion implantation. The PL spectra of the Er^{3+}-doped silica prepared from the melt and ion implantation look similar. The shape of the Na-SiO_2 spectrum is quite different. Changes of the Stark-split energy levels are due to local differences in the host electric field. EXAFS data showed that Er^{3+}-ions have 6 O first neighbours, at a distance 2.26Å, and a second neighbour Er-Si shell at 3.11Å. A schematic representation of the Er^{3+} site in SiO_2 is shown in figure 3.6. They found that the Er^{3+}-site in sodium silicate glass is essentially site A described above. When a Na network modifier is added, the Na^+ ions break the Si-O network and the Er-O group is freed from the forces applied by the Si-O network.

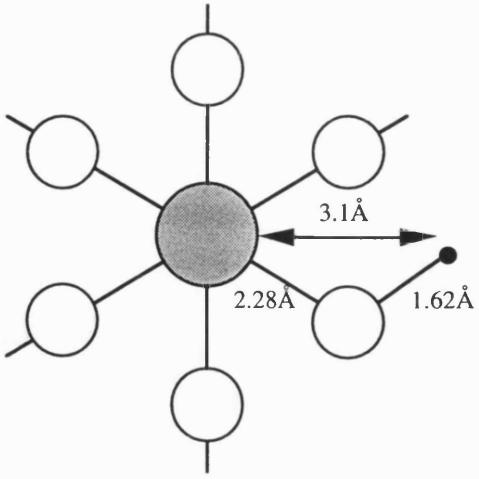

Figure 3.6. Schematic representation of local environment around the Er^{3+}-ion in SiO_2.

3.7.2. Erbium doped alumino-silicate glass

What happens when Al_2O_3 is added to rare-earth-doped silica? The addition of Al to the Er^{3+}-silicate glass changes the rare-earth environment. The limitations in Er^{3+}-sites dictated by the rigidity of the silica covalent bonds and the sixfold coordination of Er with O are lifted. In terms of short-range order, the Er^{3+}-ion can be described to be in an environment of prescribed symmetry. In order to picture the effect of Al, let us now consider the Er^{3+}-sites in materials containing Al and O. It is thus instructive to look at the absorption spectrum of the Er^{3+}-ion in crystals of $Y_3Al_5O_{12}$ and in $YAlO_3$[20]. The Er^{3+}-ion is situated in an eight-fold coordinate site in the cubic $Y_3Al_5O_{12}$. The coordination of the rare-earth site is twelve-fold in $YAlO_3$. Both these crystals can be made to operate as optical amplifiers. Arai et al.[15] suggest that Al is incorporated into the silica network in two ways:

a) a tetrahedral bonding configuration as a network former $AlO_{4/2}$.

b) in an octahedral co-ordination of oxygen atoms as a network modifier such as $AlO_{6/2}$.

Combinations of the various structural units $SiO_{4/2}$, $AlO_{4/2}$ and $AlO_{6/2}$ surround the Er^{3+} ions to accommodate them into the glass network. Thus, the Al introduces bridging oxygens, increases the coordination number of the rare-earth ion, increases the freedom of bonding configurations available eliminating clustering. Al codoped glass has a spectrum similar to that of multicomponent glasses because it contains rare-earth ions in several co-ordination states and bonding configurations.

The effect of Al can also be explained in terms of solvation chemistry. In the liquid state Al_2O_3 dissolves well in SiO_2, and Er_2O_3 dissolves in Al_2O_3 without liquid immiscibility. Therefore, $AlO_{4/2}$, and/or $AlO_{6/2}$, act as solvation shells, making Er_2O_3 soluble in SiO_2.

Summarising, the Er^{3+}-ion in alkali silicate glasses may sit in a six fold octahedral site, cluster, or form ion-pairs around a silica tetrahedron. In crystals containing Al and O, Er^{3+} has a higher coordination of either eight or twelve. The several coordination states and bonding configuration that exist in Al codoped glass result in its broad atypical spectrum. This extra bonding and configuration freedom is also responsible for the increase of Er^{3+} solubility in silica. The addition of Al increases the Er^{3+} solubility in silica, making evenly distributed high concentration Er^{3+} doped silicate glass viable. However, the addition of non-bridging oxygens

through the use of a different codopant such as P, or a novel deposition technique, should, result in similarly highly doped Er^{3+}-silicates.

References

1. R. Reisfeld, 'Lasers and excited states of rare-earths', Springer-Verlag (1977).

2. P. Urquhart, 'Review of rare-earth doped fibre lasers and amplifiers', IEE Proc., **135,** pp.385-407 (1988).

3. S. Day, R. Bellerby, G. Cannell and M. Grant, 'Silicon based fibre pigtailed 1x16 power splitter', Electron. Lett., **28**, 10, pp.920-922, (1992).

4. C. Dragone, C.H. Henry, I.P. Kamninow and R.C. Kistler, 'Efficient single mode integrated optic star coupler on Si', IEEE Photonics Tecnol. Lett., **1**, pp.241-243 (1989).

5. R. Eisberg and R. Resnick, 'Quantum physics of atoms, molecules, solids, nuclei and particles' John Wiley, 2nd Ed. (1985).

6. W. Miniscalco, 'Erbium-doped glasses for fiber amplifiers at 1500nm' J. Lightwave Technol., **9,** 2, pp.234-250, (1991).

7. E. Desurvire and J.R. Simpson, 'Evaluation of $^4I_{15/2}$ and $^4I_{13/2}$ Stark-level energies in erbium doped aluminosilicate glass fiber', Opt. Lett., **15**, pp.547-549 (1990).

8. B.R. Judd, 'Optical absorption intensities of rare-earth ions', Phys. Rev., **127,** 3, pp.750-761 (1962).

9. G.S. Ofelt, 'Intensities of crystal spectra of rare-earth ions', J. Chem. Phys., **37**, 3, pp.511-520 (1962).

10. G.O Jones, 'Glass', Chapman and Hall Ltd., pp.21-42 (1956).

11. R.Weast, ed., 'CRC handbook of chemistry and physics', 69th Ed.

12. S.R. Elliot, 'Physics of amorphous materials', Longman, pp.48-49 (1985).

13. R.W.G. Wyckoff, 'The structure of crystals', 2nd. Ed., The Chemical Catalog Company Inc., pp.252-254.

14. K. Arai, H. Namikawa, K. Kumata, and T. Honda, 'Aluminium or phosphorous co-doping effects on the fluorescemce and structural properties of neodymium-doped silica glass', J. Appl. Phys., **59**, pp.3430-3436 (1986).

15. P.F. Wysochi, J.K. Wagener, M.J.F. Digonnet and H.J. Shaw, 'Evidence of modelling of paired ions and other loss mechanisms in erbium-doped silica fibres', Proc. SPIE, **1789**, pp.66-79 (1992).

16. C.C. Robinson, 'Multiple sites for Er^{3+} in alkali silicate glasses(I). The principal sixfold coordinated site of Er^{3+} in silicate glass', J. Non-Cryst. Solids, **15**, pp.1-10 (1974).

17. C.C. Robinson, 'Multiple sites for Er^{3+} in alkali silicate glasses(II). Evidence of four sites for Er^{3+}', J. Non-Cryst. Solids, **15**, pp.11-29 (1974).

18. J. Gruber et al., 'Energy levels of single-crystal erbium oxide', J. Chem. Phys., **45**, pp.477-482 (1966).

19. M.A. Marcus and A. Polman, 'Local structure around Er in silica and sodium silicate glasses', J. Non-Cryst. Solids, **136**, pp.260-265 (1991).

20. S.A. Payne et al., 'Infrared cross-section measurements for crystals doped with Er^{3+}, Tm^{3+}, and Ho^{3+}', IEEE J. Quantum Electron., **28**, pp.2619-2630 (1992).

Chapter 4: Modelling

Introduction

Erbium doped waveguide amplifiers are attractive active elements which may be introduced into integrated optical circuits. To achieve gains of a few dB/cm, high doping levels are required. However, dopant concentration is limited by phase separations and clustering of rare-earth ions. Clustering can be reduced by changing the Er^{3+}-site in the glass matrix[1]. A gain of 3dB over 2.8cm of fluoride fibre[2] and signal enhancement on pumping 21dB over 2.4cm of sodium calcium silicate glass[3] have recently been reported.

The performance of optical amplifiers depends on the populations of the energy levels participating in radiative transitions. These populations are dependent on concentration and distribution of rare-earth ions, and on the waveguide design and pumping conditions.

The chapter starts by introducing the mechanisms that effect amplifier efficiency. By solving the rate equations given in section 4.2, an expression for gain in terms of level populations and cross sections is derived in section 4.3. The wave equation for the waveguide is solved numerically. The relationship between gain, pump photon density and Er^{3+} concentration is given in the material's section of 4.4. Waveguide geometry and refractive index profile can be tailored to improve pump efficiency through the overlap between Er^{3+} concentration and field intensity. The performance of planar and channel amplifiers with high doping levels are compared in section 4.5. The presence of clusters and ion pairs is discussed in the final section where the effect of dopant ion separation on energy transfer rates is analysed.

4.1. Amplifier efficiency

Several factors affect the efficiency of an amplifier : host glass composition, dopant concentration, waveguide design and pump wavelength. Ion-dynamic lattice interactions, excited state absorption, and ion-ion interactions can have a deleterious effect on the amplifier gain by converting pump photons into heat and emissions at unwanted wavelengths.

Recalling the energy level diagram figure 3.1 from section 3.2, the metastable level $^4I_{13/2}$ is the initial level for the transition producing gain at 1535nm. Any process removing Er^{3+} ions from this state, other than stimulated emission into the signal mode, decreases the gain of the amplifier. Non-radiative relaxation directly to the ground state as a result of interaction between electrons and phonons, does not significantly reduce the metastable population of silicate glasses. The loss mechanisms that significantly affect efficiency are excited state absorption, discussed in section 4.1.1 and ion-ion interactions introduced in section 4.1.2. Clustering and uneven dopant distributions exacerbate cooperative processes because interaction strengths are related to ion-ion separation.

The OH^- complex is extremely effective at quenching excited rare earth ions. The fluorescence is absorbed by an OH^- impurity. This is possible because the OH^- absorption peak extends to the 1400nm region, which overlaps with the tail of the Er^{3+} ion emission at 1500nm. For low OH^- concentrations, the energy transfer process and quenching rate is controlled by the rare earth concentration and distribution. The OH^- impurities are easily reduced by annealing deposited material. In future work, it would be interesting to find the optimum temperature at which fluorescence intensity is maximised without modifying distribution, and thus reducing the metastable lifetime.

4.1.1. Excited state absorption

Excited state absorption (ESA) is the excitation of an ion in the metastable state, or another excited state, to a higher level through the absorption of a pump or signal photon. The ion ultimately returns to the excited state it came from, however, a photon is lost either to heat or spontaneous emission at an unwanted wavelength. Excited ions have an ESA spectrum which differs from their ground state absorption (GSA) spectrum due to the new energy gaps to the higher lying states.

4.1.2. Ion-ion interactions

There are several types of ion-ion interactions which lead to concentration quenching in Er-doped glasses, through either cooperative upconversion or cross-relaxation. Four of these mechanisms are illustrated in figure 4.1.

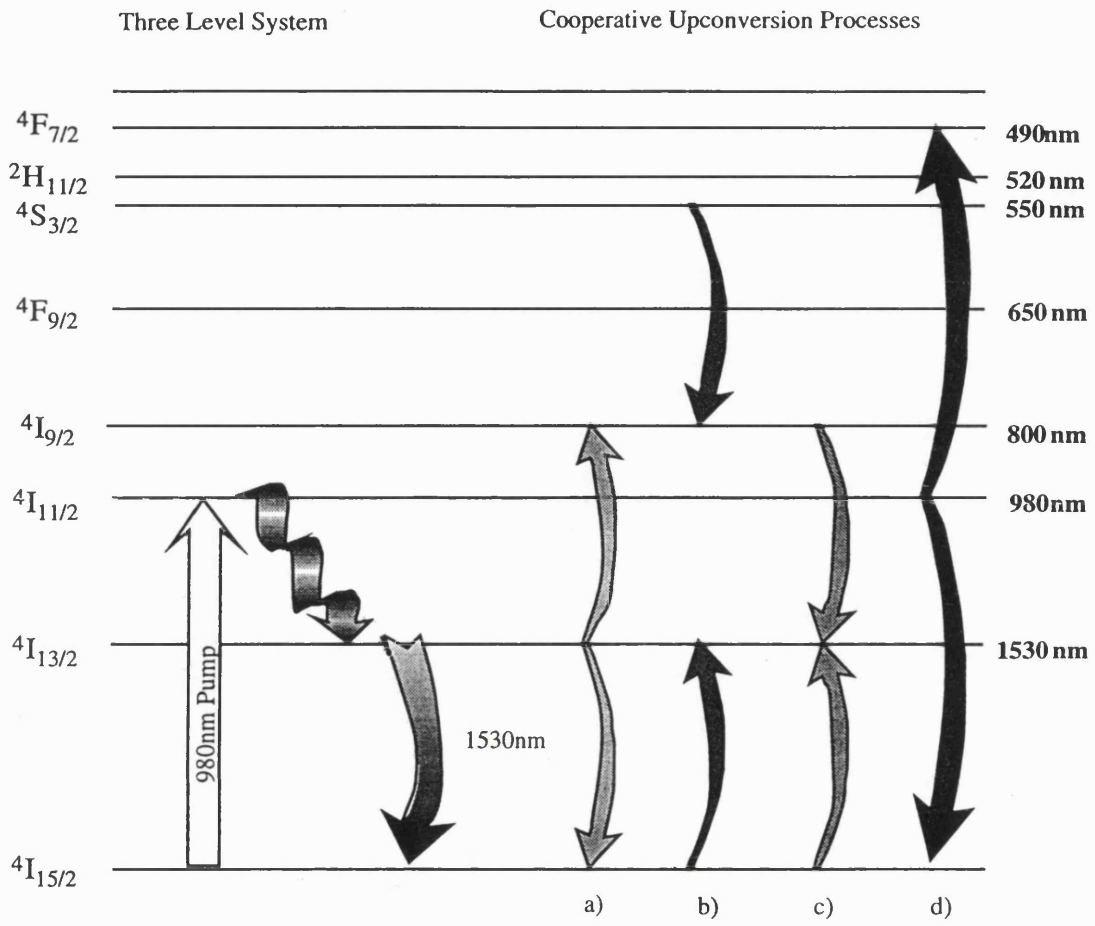

Figure 4.1. The energy level diagram for the Er^{3+}-ion, showing how the simple three level system on the left is affected by ion-ion interactions on the right.

The first case, labelled a), is called low level upconversion. 2 neighbouring atoms are excited to the $^4I_{13/2}$ state. Energy is transfered non-radiatively from the donor atom to the acceptor atom. This results in a de-excited donor atom and an acceptor atom in the $^4I_{9/2}$. When the material is excited using the $^4I_{13/2}$ pump band and low pump powers, low level upconversion is dominant and the other cooperative processes are negligible. Due to the fast lifetime of the $^4I_{9/2}$ state, the most probable decay path for the acceptor atom is to the $^4I_{11/2}$ and then to the $^4I_{13/2}$. However, there is a low probability for the atom to relax to the ground state under emission of a photon at 980nm.

For higher pump powers, and when the $^4I_{11/2}$ or the $^4I_{9/2}$ pump bands are used, higher level cooperative processes become evident. In the case shown in figure 4.1d), two ions in the $^4I_{11/2}$ state interact; the donor transfers its energy to the acceptor leaving itself in the ground state and the acceptor in the higher $^4F_{7/2}$ level.

The acceptor atom may relax down to the metastable level through multiphonon emission, or emit a photon with wavelength 540nm, 520nm, 650nm, 720nm, 820nm, or 980nm. The probability of photon emission at a particular wavelength is dependent on the lifetime of that level.

Concentration quenching can also occur through the two cross-relaxation processes labelled b) and c) in figure 4.1. For the case illustrated by b), an ion excited into the $^4S_{3/2}$ level interacts with a nearby atom in the ground state, the donor transfers part of its energy to the acceptor, leaving the acceptor in the $^4I_{13/2}$ level and the donor in the $^4I_{9/2}$ level. In figure 4.1c), an ion in the $^4I_{9/2}$ state interacts with an ion in the ground state; the partial energy transfer results in both donor and acceptor being left in the intermediate $^4I_{13/2}$ state.

Several factors determine which one of the ion-ion interactions becomes dominant. As shown later in this chapter, pump wavelength, pump power, waveguide geometry, dopant concentration, and dopant distribution affect the populations of the energy levels. The transition probabilities of ion-ion interactions for Er^{3+}-doped silica and alumino-silicates are not all known. The upconversion coefficient, k_2, from the $^4I_{13/2}$ state was calculated to be around $10^{-22}m^3/s$ in EDFA by Blixt[4]. The upconversion coefficient from the $^4I_{11/2}$ state is k_3; no direct calculation of its value is presently available. From theoretical considerations, k_3, and higher order interionic coupling terms can be estimated. For simplicity, upconversion coefficients were initially assumed to be constants independent of Er^{3+} concentration. The upconversion coefficient is dependent on glass matrix composition, dopant concentration, and dopant distribution as discussed later in this chapter. The results in section 4.4.1 were obtained accounting for the dependence of upconversion coefficients on Er^{3+}-ion separation. For the results in 4.4.2, (historically obtained before those of previous section) the upconversion coefficients were assumed to be independent of Er^{3+} concentration.

4.2. Rate equations

The rate equations for the energy levels in figure 4.1 are developed taking into account radiative, non-radiative, inter-ionic transitions and ESA. In the following discussion, energy levels $^4I_{15/2}$, $^4I_{13/2}$, $^4I_{11/2}$, $^4I_{9/2}$, $^4F_{9/2}$, $^4S_{3/2}$, $^2H_{11/2}$, $^4F_{7/2}$, of the Er^{3+} ion are indicated as levels 1, 2, 3, 4, 5, 6, 7, 8. The population of level i is n_i, where

i=1 to 8. The system is pumped with a photon density N_p into level 3 and a signal photon density N_s into level 2. The analysis is restricted to 1-photon processes. The steady state rate equations for the excited state populations of Er^{3+} are given by

$$\frac{dn_1}{dt} = -B_{12}n_1N_s + (A_{21} + B_{21}N_S)n_2 - B_{13}n_1N_P + k_2n_2^2 + k_3n_3^2 - k_{1,6}n_1n_6 - k_{1,4}n_1n_4 \qquad 4.2\text{-}1$$

$$\frac{dn_2}{dt} = B_{12}n_1N_s - (A_{21} + B_{21}N_S)n_2 + \frac{n_3}{\tau_3} - 2k_2n_2^2 + 2k_{1,4}n_1n_4 + k_{1,6}n_1n_6 \qquad 4.2\text{-}2$$

$$\frac{dn_3}{dt} = B_{13}n_1N_P - 2k_3n_3^2 - B_{38}n_3N_P - \frac{n_3}{\tau_3} + \frac{n_4}{\tau_4} \qquad 4.2\text{-}3$$

$$\frac{dn_4}{dt} = k_{1,6}n_1n_6 - \frac{n_4}{\tau_4} - k_{1,4}n_1n_4 + k_2n_2^2 + \frac{n_6}{\tau_6} \qquad 4.2\text{-}4$$

$$\frac{dn_6}{dt} = \frac{n_8}{\tau_8} - k_{1,6}n_1n_6 - \frac{n_6}{\tau_6} \qquad 4.2\text{-}5$$

$$\frac{dn_8}{dt} = B_{38}n_3N_P + k_3n_3^2 - \frac{n_8}{\tau_8} \qquad 4.2\text{-}6$$

the Einstein coefficients A_{ij}, B_{ij}, represent spontaneous and stimulated emission, as given in chapter 2. τ_i are non-radiative lifetimes, k_i and k_{ij} coefficients represent ion-ion interactions, upconversion (i=j) and cross relaxation ($i \neq j$) respectively. The term $B_{38}n_3N_P$ is due to ESA from level 3. All spontaneous emission terms from levels above level 3 have been omitted because non-radiative lifetimes are much shorter than radiative ones. However, if radiative emission from a particular level is of interest, the spontaneous emission term A_{ij} must be added to the corresponding rate equation.

The rate equations can also be written in terms of cross-sections and group velocity, and hence can be more easily related to experimental results. This is done by recalling the definition of cross-section for photon absorption and scattering. Consider a parallel beam of photons travelling with phase velocity v_g, passing through a slab of matter, containing n atoms per unit volume, as shown in figure 4.2.

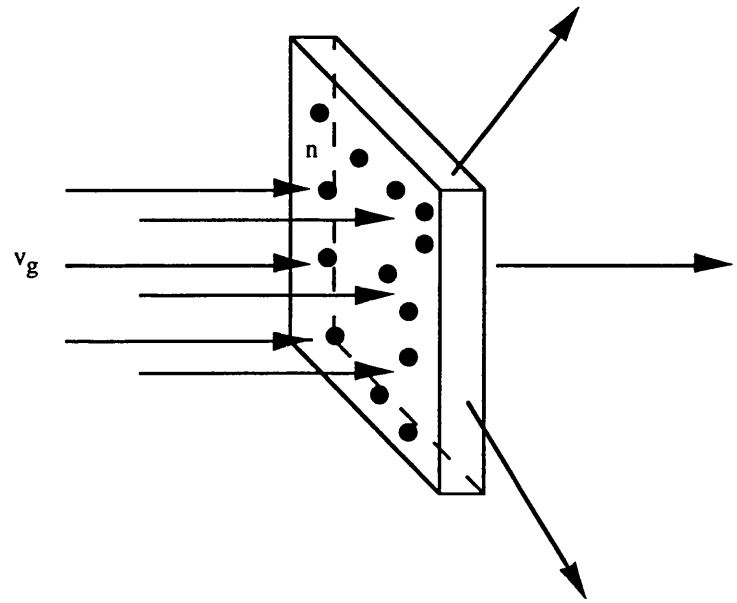

Figure 4.2. A beam of photons with group velocity v_g, passing through a thin slab of material containing n absorbing atoms per unit volume.

Assume that the slab is thin and so that the probability of photon absorption is close to zero. The likelihood of absorption is defined so that

$$\frac{dn_i}{dt} = n_i N_{s,p} v_g \sigma \qquad 4.2\text{-}7$$

σ, the cross section is a proportionality constant with dimension of area. From the rate equation 4.2-1, the rate of change of population of ground state atoms which had not previously been excited is

$$\frac{dn_1}{dt} = -B n_1 N_s \qquad 4.2\text{-}8$$

Comparison of equations 4.2-7 and 4.2-8 gives

$$B = \sigma v_g \qquad 4.2\text{-}9$$

Using the relation 4.2-9 the rate equations can be rewritten by expressing the stimulated Einstein coefficients in terms of cross-sections.

The first three rate equations become

$$\frac{dn_1}{dt} = (\sigma_{21}n_2 - \sigma_{12}N_1)v_g N_S + \frac{n_2}{\tau_{21}} - \sigma_{13}v_g n_1 N_P + k_2 n_2^2 + k_3 n_3^2 - k_{1,6}n_1 n_6 - k_{1,4}n_1 n_4 \qquad 4.2\text{-}10$$

$$\frac{dn_2}{dt} = -(\sigma_{21}n_2 - \sigma_{12}N_1)v_g N_S - \frac{n_2}{\tau_{21}} + \frac{n_3}{\tau_3} - 2k_2 n_2^2 + 2k_{1,4}n_1 n_4 + k_{1,6}n_1 n_6 \qquad 4.2\text{-}11$$

$$\frac{dn_3}{dt} = \sigma_{13}v_g n_1 N_P - 2k_3 n_3^2 - \sigma_{38}v_g n_3 N_P - \frac{n_3}{\tau_3} + \frac{n_4}{\tau_4} \qquad 4.2\text{-}12$$

τ_{21}, the radiative lifetime, is given by $\tau_{21} = \frac{1}{A_{21}}$ as shown in equation 3. 4-3

In steady state conditions, the left hand side of all rate equations is nil, and the equations are solved for steady state populations. Since the system is closed, the total number of electrons is conserved and each equation in the set is a consequence of the others. That is

$$\sum_i n_i = n_E \qquad 4.2\text{-}13$$

where n_E is the total number of Er^{3+}-ions per unit volume.

4.3. Gain

The contribution of radiative transitions between levels 1 and 2, to gain[5] $\gamma(\lambda)$, at wavelength λ, can be written as

$$\gamma(\lambda) = \sigma_{21}(\lambda)n_2 - \sigma_{12}(\lambda)n_1 \qquad 4.3\text{-}1$$

where σ_{21} and σ_{12} are the emission and absorption cross-sections.

The propagation of optical fields is determined by the complex atomic susceptibility. Using equation 2.2.3-9, the imaginary part of the susceptibility, χ'', is the sum of the terms of the form

$$\chi''=\frac{n_r^2}{k}(\sigma_{21}(\lambda)n_2 - \sigma_{12}(\lambda)n_1) \qquad 4.3\text{-}2$$

where n_r is the refractive index far from resonance, and k is the wavevector. Stark splitting does not affect the form of equation 4.3-2, provided the dependence of cross-section on wavelength is considered. The cross-sections, $\sigma_{21}(\lambda)$ and $\sigma_{12}(\lambda)$, can be related to their respective spectroscopic lineshapes via the Ladenburg-Fuchtbauer equation.

$$\sigma''_{21,12}(\lambda)=\frac{\langle\lambda_s^2\rangle_{21,12}^2}{8\pi n_r^2 c\tau}\cdot\frac{I_{21,12}(\lambda)}{\int I_{21,12}(\lambda)d\lambda} \qquad 4.3\text{-}3$$

where the $I_{21,12}(\lambda)$ are the experimental fluorescence and absorption lineshapes. $\langle\lambda_s^2\rangle_{21,12}^{1/2}$ are the fluorescence and absorption wavelengths averaged over all possible transitions. They may be roughly approximated as the peak fluorescence and absorption wavelengths of the Er^{3+}-silicate used.

The population values obtained by solving the rate equations and the cross sections calculated from the lineshapes using the Ladenburg-Fuchtbauer relation 4.3-3, are used to calculate χ''. The Hilbert transform of χ'' (equation 2.2.3-10) gives χ', the real part of the atomic susceptibility. The atomic susceptibility is used to calculate the dielectric constant, ε, via the relation 2.2.3-3.

Now, the wave equation can be solved numerically. The two dimensional wave equation can be used because in the effective index approximation for stripe waveguides, the third dimension, y, is accounted for in the confinement factor in $\Delta\varepsilon$.

$$\left(\frac{\partial^2}{\partial x^2}+\frac{\partial^2}{\partial z^2}\right)E=-\frac{\omega^2}{c^2}(\varepsilon_o+\Delta\varepsilon)E \qquad 4.3\text{-}4$$

$$E=E_0(z,x)e^{ikz}$$

$\Delta\varepsilon$, the part of ε which is not a constant, is dependent on waveguide passive characteristics such as lateral confinement and the waveguide active characteristic gain. From Agrawal[6] , $\Delta\varepsilon$ is given by

$$\Delta\varepsilon = 2n_f\Delta n - \frac{in_f D\gamma}{k_o} + \frac{in_c}{k_o}[1-D]\alpha \qquad 4.3\text{-}5$$

where α is the waveguide loss and D the confinement factor is given in equation 2.1-18.

In order to estimate the effect of gain on $\Delta\varepsilon$, take the largest possible contribution, that is the contribution corresponding to the peaks of $\sigma_{21}(\lambda)$ and $\sigma_{12}(\lambda)$. Spectral lineshapes are assumed to be independent of power in this calculation only.

4.4. Results

The wave equation for planar and channel waveguides was solved using two numerical approaches: a beam propagation method (BPM) and a full-vectorial finite-element method (VFEM). The results from the two approaches were in close agreement (1%) and were published[7,8]. The parameters input into the two models were picked (out of an experimental results hat) by the two programmers and are thus slightly different. References of the papers published and submitted for publication are in Appendix A.

4.4.1. Material Gain

Table 4.1 gives a list of the values of the coefficients and lifetimes used. It was assumed that different fabrication processes do not affect these measurements significantly. Whereas this assumption is certainly valid for the Einstein coefficients, lifetimes and ion-ion interaction coefficients are affected by fabrication processes. The k_{ij} coefficients depend on the Er^{3+} concentration and are discussed in section 4.5.

Ideally, these measurements should be reproduced for the glass under investigation. The rate equations are solved numerically. Population values obtained by solving the rate equations are used to calculate the complex atomic susceptibility.

The wave equation in the waveguide is solved using the beam-propagation method[9] (BPM), under the assumption that variations in the field amplitude along the cavity are slow compared to phase variations.

Constants		Constants	
B_{12}	$1.32\times10^{-16}m^3/s$	σ_{12}	$6.6\times10^{-25}m^2$
B_{21}	$1.14\times10^{-16}m^3/s$	σ_{21}	$5.7\times10^{-25}m^2$
$B_{13}=\sigma_{13}v_g$	$6.24\times10^{-17}m^3/s$	σ_{13}	$31.2\times10^{-26}m^2$
B_{38}	$5\times10^{-17}m^3/s$	$v_g=c/n_g$	$2\times10^8m/s$
$A_{21}=1/\tau_{21}$	$100s^{-1}$	$A_{21}=1/\tau_{21}$	$100s^{-1}$
τ_3	$1.5\times10^{-4}s$	τ_4	$5\times10^{-8}s$
τ_8	$2\times10^{-8}s$		

Table 4.1. List of coefficients and lifetimes taken from the literature[10].

The effect of upconversion and ESA on the properties of the amplifier have been assessed by studying local gain in the doped material and overall gain of a single-stripe amplifier with uniform Er^{3+}-doping. The waveguide dimensions used are: width 1μm, thickness 5μm, and length 0.5 to 5cm. The refractive index step is 7.5×10^{-3} and it is a monomode waveguide.

When no ion-ion interactions are present, optical gain becomes positive when the pump photon density exceeds the ratio $\sigma_{12}/\sigma_{21}\sigma_{13}\tau_{21}v_g$. This threshold photon density is independent of Er^{3+} concentration. When pump photon density is $\approx 1/(\sigma_{13}\tau_3 v_g)$ the population of level 3 starts to be significant. For very high pump photon densities, optical gain saturates at approximately $\sigma_{21}n_E$ (about $5.7\times10^{-23}n_E$ m^{-1} for Al: P silica). In integrated optics, local gains of a few dB per cm are needed requiring a minimum Er^{3+} concentration $n_E=10^{21}$ ions/cm^{-3}.

When upconversion from the metastable level is considered, the parameters which determine the level populations are: Er^{3+} concentration n_E, the normalised pump photon density $\phi = \tau_3\sigma_{13}v_gN_p$, and the concentration $n_t = (k_2\tau_3)^{-1}$ at which the upconversion rate is of the same order of magnitude as the non-radiative decay rate of electrons from level 3. The populations of levels 1 and 2 are approximately

$n_1 = \frac{(n_E - n_2)}{\phi}$ and $n_2 = (n_E n_1)^{1/2}$. When upconversion from level 3 and ESA are taken into account, the expressions for n_1 and n_2 are more complicated.

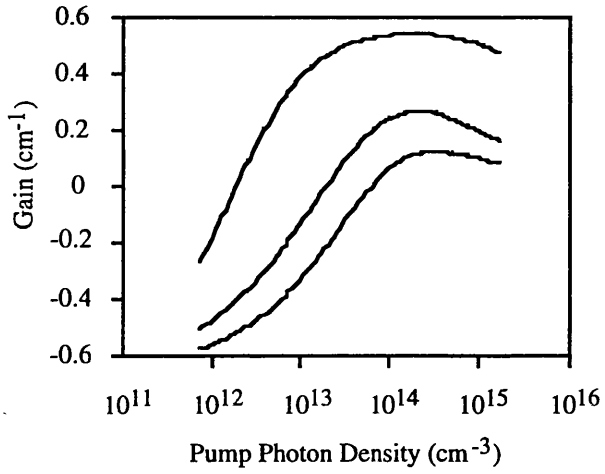

Figure 4.3. Optical gain of Er^{3+}-doped silica as a function of the pump photon density in the presence of ESA and with or without low level upconversion. The top curve shows gain in absence of upconversion. The two lower curves have been obtained with upconversion coefficient $k = 4 \times 10^{-24} m^3/s$ from level $^4I_{13/2}$ (middle curve) and with upconversion coefficient $k = 1 \times 10^{-22} m^3/s$ from level $^4I_{13/2}$ (lower curve). The Er^{3+} concentration is 2×10^{26} ions$/m^3$.

The effect of low order upconversion on optical gain is shown in figure 4.3. Figure 4.3 shows gain as a function of the pump photon density in Er-doped silica for $n_E = 2x10^{26} m^{-3}$. The top curve represents gain in absence of upconversion. The lower asymptote of the extension of the top curve (not shown in Fig. 4.3) is equal to $\sigma_{12} n_E$. The upper asymptote in absence of ESA would be $\sigma_{21} n_E$, ESA causes a slight reduction in gain with increase of pump photon density, and thus there is a turning point in the curve. The two lower curves represent gain in presence of upconversion from level 2 only. Two upconversion coefficient values have been used. An increase of the upconversion coefficient results in an increase of threshold power and a decrease in saturation gain for all powers; both effects increase with Er^{3+} concentration.

Figure 4.4 shows the effect of higher order upconversion on gain. The curves represent gain in the presence of only upconversion (upper curve), and gain with higher order upconversion, cross relaxation and ESA from level 3 as well (lower curve). Ion-ion interactions do not affect the lower asymptote, however, the upper one is now $\left(n_E / \tfrac{1}{2} k_{ud} \tau_3\right)^{1/2}$ where τ_3 is the non radiative lifetime of the pump level. For a

uniformly distributed glass the asymmetry between the lower and upper asymptotes can be used to measure the upconversion coefficient k_2. Excited state absorption from the pump level removes the horizontal asymptote at saturation (lower curve). For low Er^{3+} concentration, and in the absence of ion-ion interactions, the threshold pump photon density is independent of n_E.

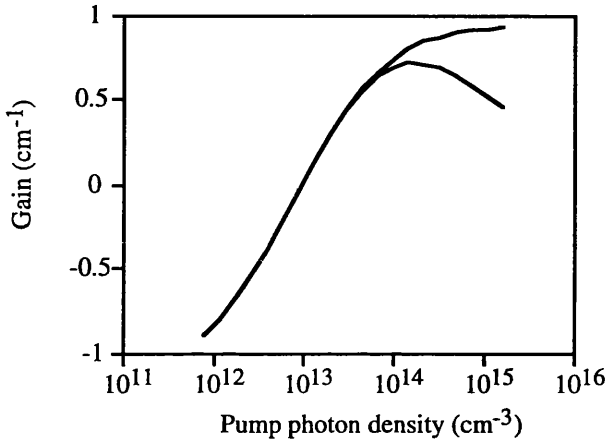

Figure 4.4. Optical gain of Er^{3+}-doped silica as a function of the pump photon density showing effect of higher order upconversion and ESA. The two curves have been obtained with upconversion from level 2 only (upper curve), and with higher order upconversion, cross relaxation and ESA from level 3 as well (lower curve). The Er^{3+} concentration is 2×10^{26} ions$/m^3$, the upconversion coefficient is $k=4\times10^{-24} m^3/s$.

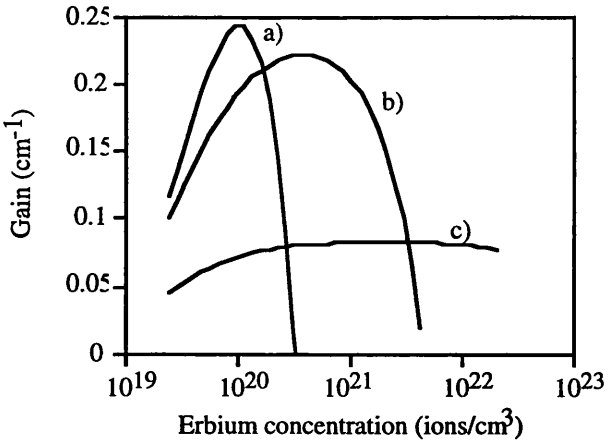

Figure 4.5. Optical gain of Er-doped silica versus Er concentration for three different pump photon densities. Gain is in presence of upconversion from level 2, higher order upconversion, cross relaxation and ESA from level 3. The pump photon densities for the three curves are: a) $10^{14}cm^{-3}$, b) $10^{15}cm^{-3}$ and c) $10^{16}cm^{-3}$.

For a given pump power, gain increases with Er^{3+} concentration until the metastable level starts to be significantly depleted by upconversion. Maximum gain is achieved for $n_E = (\phi\sigma_{21}/2\sigma_{12})^2/k_2\tau_3$. The saturation gain decreases in the presence of higher order upconversion and ESA. This is shown in figure 4.5 were gain is plotted against Er concentration for three different pump photon densities. Similar curves can be obtained for a channel amplifier. Kitagawa[11] published experimental results showing a similar gain versus Er^{3+} concentration curve for a fixed pump power of 100mW. From the family of curves in figure 4.5, it is seen that the pump power must be optimised depending on the Er^{3+} concentration. For a fixed concentration, if the pump power is too small it is insufficient to cause population inversion, if it is too high a gain reduction is seen due to ESA from the pump level. An optimum Er^{3+} concentration value cannot be assigned, however for modest pump powers the Er^{3+} concentration should be in the range $5x10^{19}$ion/cm^3 to $1x10^{22}$ion/cm^3.

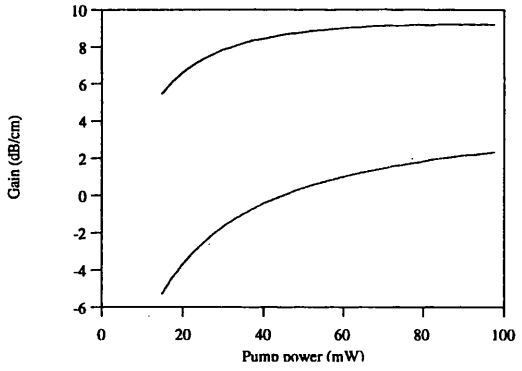

Figure 4.6. Gain of a single-channel amplifier as a function of pump power (λ=980nm). The two curves have been obtained with upconversion coefficient $k = 4\times10^{-24}\,m^3/s$ from level $^4I_{13/2}$ (upper curve) and with upconversion coefficient $k = 1\times10^{-22}\,m^3/s$ from level $^4I_{13/2}$ (lower curve). The Er^{3+} concentration is $2\times10^{26}\,ions/m^3$.

The effect of upconversion on the properties of waveguides has been assessed by studying the gain of a single stripe amplifier with uniform doping. The effect of different stripe widths and lengths are discussed in section 4.4.2. An increase in confinement results in an increase in gain but also a more significant upconversion related gain depression. Figures 4.6 and 4.7 show the effect on gain of low level upconversion and higher order upconversion. The result of increasing the upconversion coefficient is to increase the threshold power and to decrease

saturation gain for all powers. Higher order ion-ion interactions and ESA do not significantly shift the threshold power, but decrease saturation gain. With high Er^{3+} concentration, ion-ion interactions and ESA can result in a decrease in gain at 1530nm, and in an increase of luminescence at 520nm as discussed in our previous publication[12].

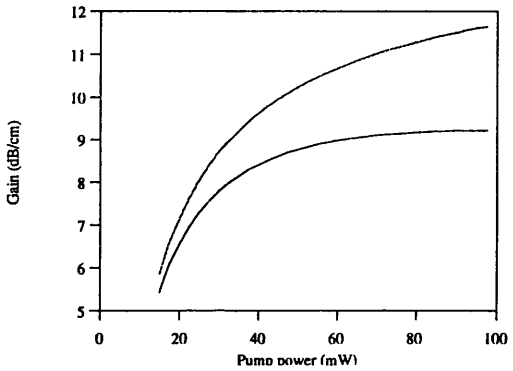

Figure 4.7. Gain in presence of higher order upconversion of a single-channel amplifier as a function of pump power (l=980nm). The two curves have been obtained with upconversion from level 2 only (upper curve), and with higher order upconversion, cross relaxation and ESA from level 3 as well (lower curve). The Er^{3+} concentration is 2×10^{26} ions$/m^3$, the upconversion coefficient is $k = 4\times10^{-24} m^3/s$.

The effect of upconversion from the metastable state, higher order upconversion and ESA from the $^4I_{11/2}$ level on the gain coefficient for a highly doped Er^{3+}-SiO_2 material has been analysed. The dopant concentration, waveguide geometry, pump wavelength, and power must be tailored for the intended application. In the next section the effect of waveguide geometry and refractive index optimisation on gain is presented.

4.4.2. Amplifier gain

A numerical approach that combines a full-vectorial finite-element method (VFEM) and a Runge-Kutta (RK) algorithm was used. The VFEM allows realistic electromagnetic analysis of the amplifier to be investigated; it computes the field intensity profiles at both pump and signal wavelengths, accounting for all excited guided modes and signal polarisation states. The RK algorithm was used to

integrate the nonlinear propagation equations of a multilevel system whose rate equations include terms due to ion-ion interactions.

The waveguide geometries and refractive index profiles used are shown in figure 4.8.

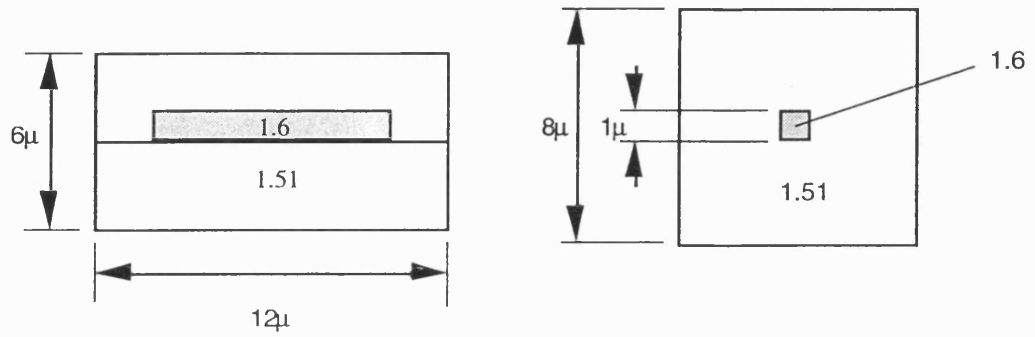

Figure 4.8. Waveguide geometry and refractive index profile of planar waveguide (left) and channel waveguide (right) used in model.

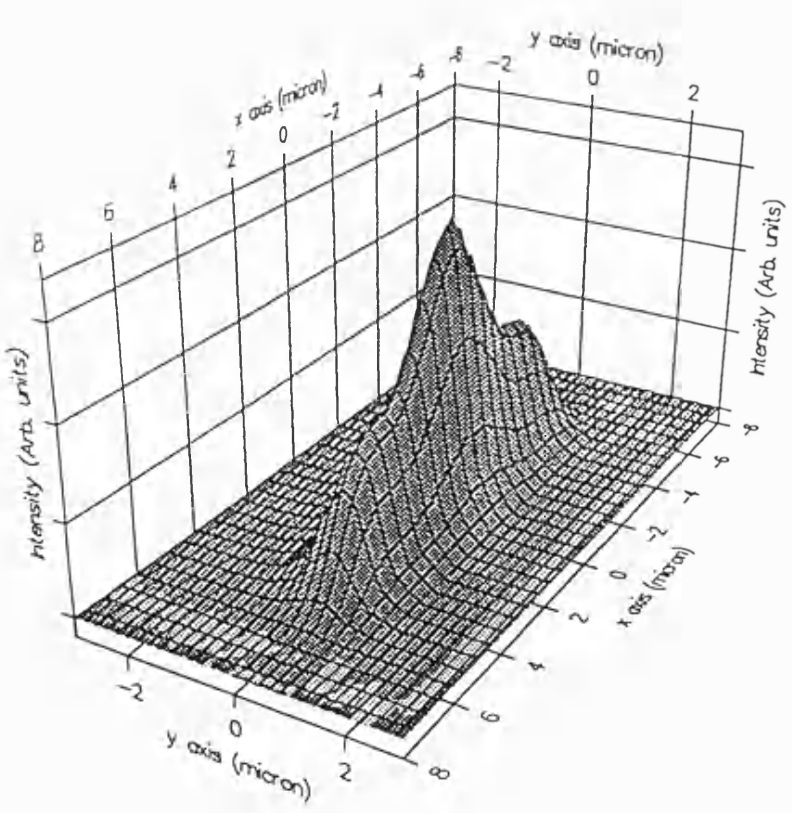

Figure 4.9. Normalised signal intensity for the planar waveguide; the signal wavelength is 1.532μm and the input signal field is linearly polarised in the x direction.

The channel waveguide was chosen to be single mode at both signal and pump wavelengths. A high refractive index step was used to provide good overlap between electromagnetic field and erbium distribution. Having obtained the guided modes, the normalised intensity profiles at pump and signal wavelength were computed, see figure 4.9 and 4.10. Linearly polarised pump fields at 45° to x axis and linearly polarised signal fields in x direction were used. In the channel amplifier the square core and single mode operation condition provide a polarisation independent signal gain, an important requirement in many optical systems.

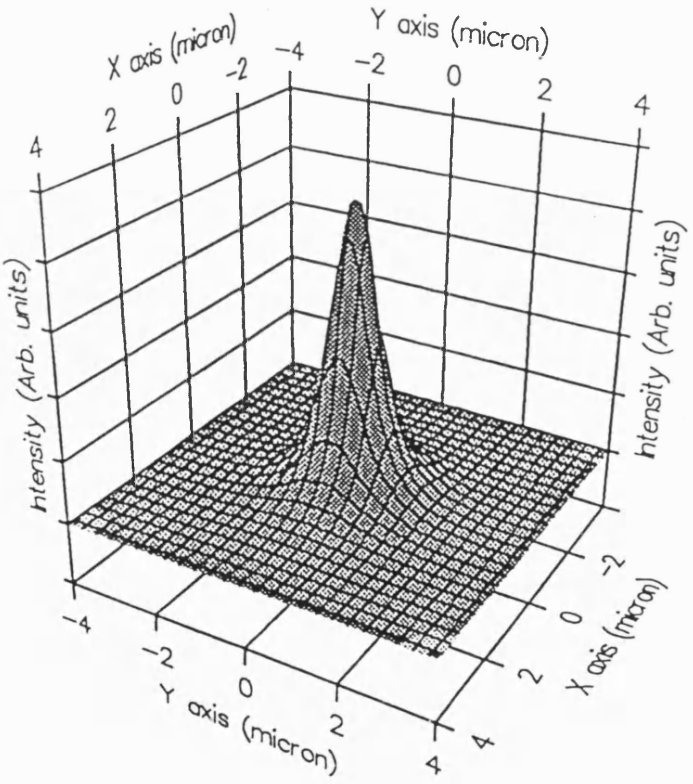

Figure 4.10. Normalised signal intensity for the channel waveguide; the signal wavelength is 1.532μm and the input signal field is linearly polarised in the x direction.

The absorption and emission spectra used were typical Er^{3+}-Al_2O_3-SiO_2 glass spectra. The gain bandwidth was subdivided into 113 wavelength slots between 1475nm and 1587nm. N_s=1mW, τ_{21}=11ms, τ_{32}=1ns, τ_{43}=1ns. Figure 4.11 and Figure 4.12 show gain versus Er^{3+} concentration for the two types of amplifiers. The waveguides length was taken as 8cm and N_p=100mW. Gain characteristics were computed accounting for and neglecting ion-ion interactions. In this section

only, upconversion and cross-relaxation coefficients were assumed to be constants independent of Er^{3+} concentration. The dependence of upconversion coefficients on erbium concentration and distribution is discussed in detail in section 4.4.3.

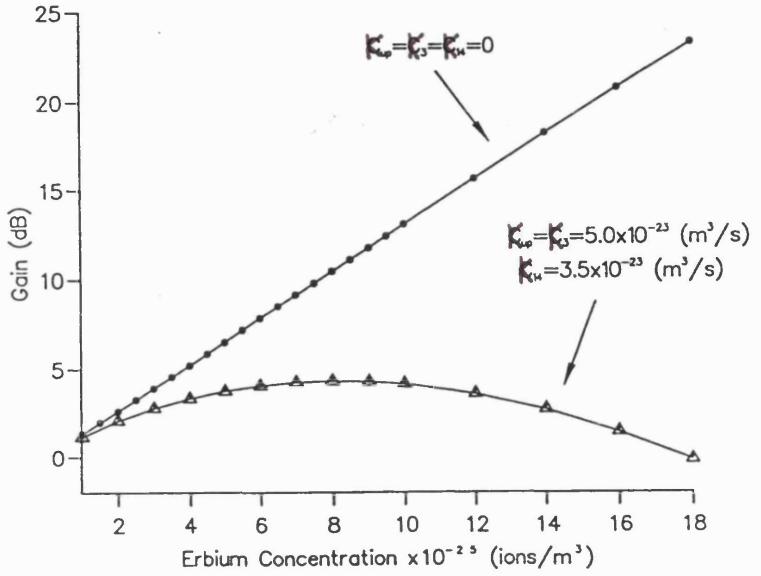

Figure 4.11. Gain versus erbium concentration for the planar amplifier (P_{p0}=100mW, P_{s0}=1μW, L=8cm).

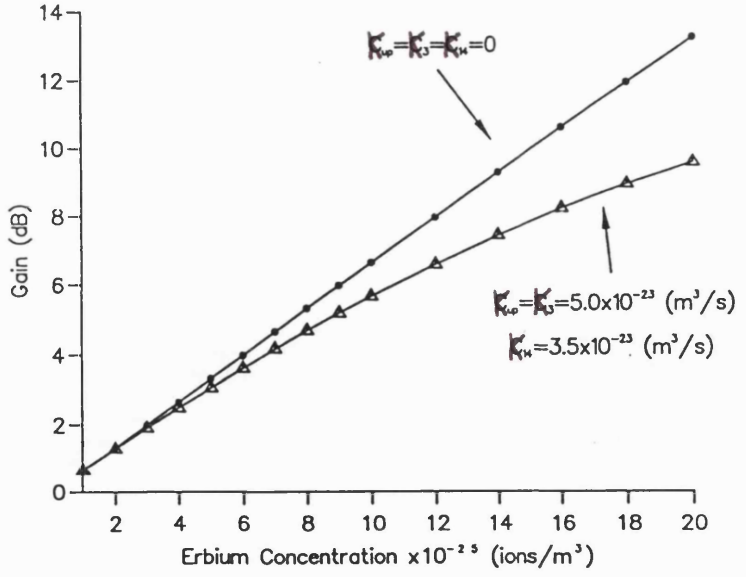

Figure 4.12 Gain versus erbium concentration for the channel amplifier (P_{p0}=100mW, P_{s0}=1μW, L=8cm).

It is interesting to note that ion-ion interactions significantly affect the amplifier performance for the planar guide; above an optimum Er^{3+} concentration the gain is reduced. For the channel amplifier the effect of ion-ion interactions is much smaller. This feature is explained by observing that the small core dimensions increase mode field confinement and thus improve pump efficiency. To prove this assertion the channel amplifier was analysed at a lower pump power. Figure 4.13 shows gain characteristics versus Er^{3+} concentration at 10mW pump power.

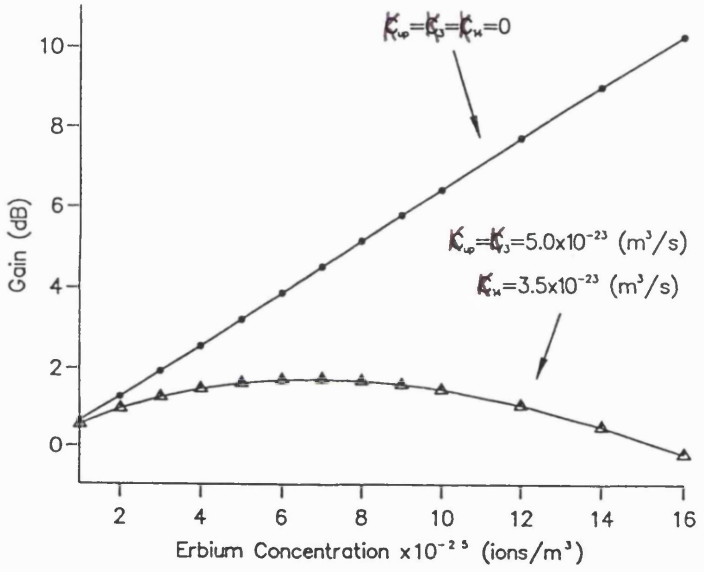

Figure 4.13. Gain versus erbium concentration for the channel amplifier (P_{p0}=10mW, P_{s0}=1μW, L=8cm).

Finally, gain characteristics as a function of device length and pump power were investigated, the Er^{3+} concentration was chosen so as to maximise pumping efficiency for a waveguide 8cm long, pumped with N_p=100mW. Figure 4.14 and figure 4.15 show signal gain versus waveguide length and pump power. In figure 4.14 it is observed that the 0dB gain threshold for the channel and planar amplifiers is obtained with 11mW and 44mW pump power respectively.

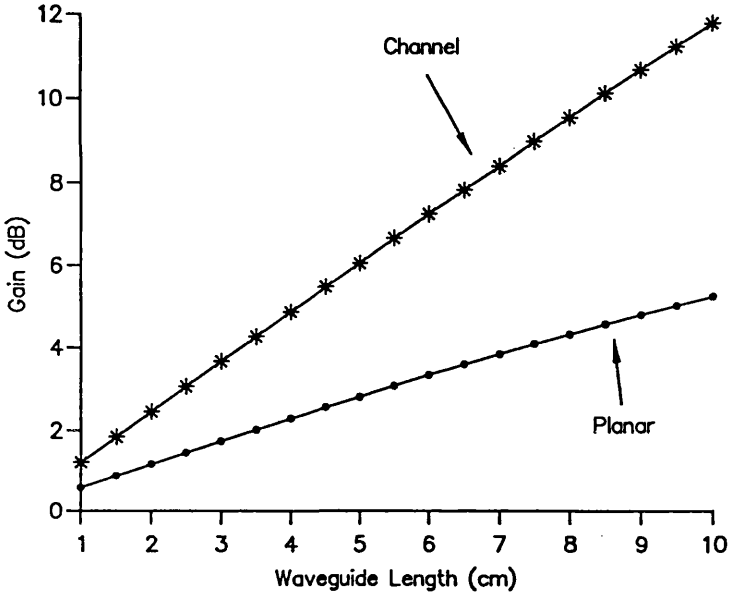

Figure 4.14. Signal gain versus waveguide length (P_{p0}=10mW, P_{s0}=1μW, and erbium concentration optimised at L=8cm).

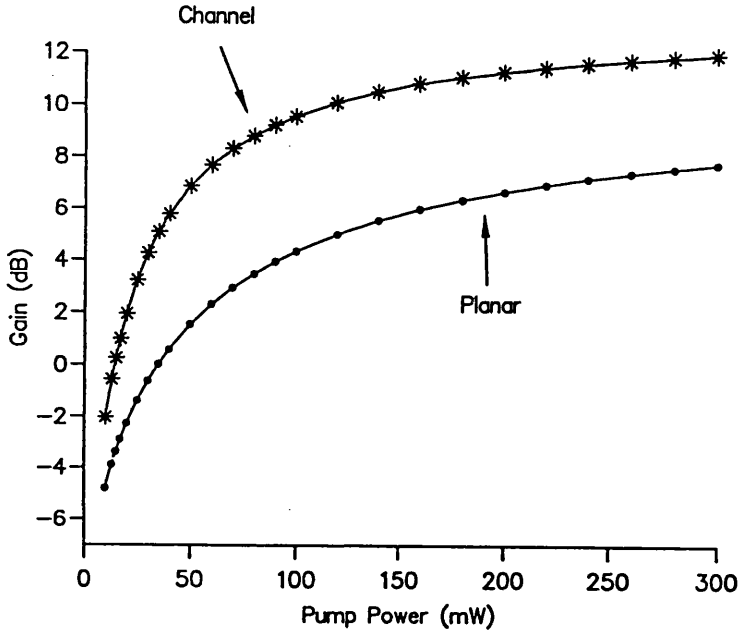

Figure 4.15. Signal gain versus pump power (L=8cm, P_{s0}=1μW, and erbium concentration optimised at P_{p0}=100mW).

Numerical results show how the negative effect on the gain by ion-ion interactions may be overcome by careful design of the waveguide. Monomode channel waveguide amplifiers with small square cores and high refractive index steps result in the highest gain per centimetre. They provide polarisation insensitive signal gain, lower noise levels and higher pump efficiencies than planar waveguide amplifiers.

4.5. Transfer rates

The gain of rare-earth doped waveguides and amplifiers is strongly dependent on rare-earth concentration and distribution. Amplifier efficiency is reduced by energy transfer between two neighbouring ions of same species. Conversely, energy transfer between ions of different species (Yb-Er) can increase gain. In chapter 3, it was shown that local charge compensation causes rare-earth ions to form ion pairs and triplets. This results in an uneven dopant distribution of randomly located single ions and fast interacting ion pairs. The presence of ion pairs, even at low rare-earth concentrations, was observed in crystals[13] and fibres[14].

The upconversion coefficients k_{ij} of the rate equations are related to the energy transfer rates. The transfer rates are dependent on donor-acceptor separation and acceptor lifetime. For uniformly doped materials, ion-ion separations can be calculated from the concentration. In the presence of ion pairs, the ion-ion separation and dopant concentration are not directly related. Two transfer rates will exist: a fast one between the two ions in a pair and a slow one between isolated ions. The upconversion coefficient is inversely proportional to the cube of the interionic distance. The interionic separation is much smaller for ion pairs than for randomly distributed ions.

Ion pairs can be in three states: one excited, both excited, or none excited. For low pump powers, ion pairs will behave like single ions because one of the ions, at most, will be excited. For high pump power, both ions in a pair will be excited and ion-ion interactions will result in one of the two ions relaxing to ground state. This transfer rate is very fast making the two photon excited state negligible. The rate equations need to be modified to account for ion pairs.

Determination of the nearest neighbour distance in a glass is difficult. Choose R_{NN} as the distance within which there is a $1-1/e$ probability of finding a nearest neighbour. For a random distribution[15],

$$R_{NN} \cong \frac{0.62}{(n_d + n_a)^{1/3}} \qquad 4.5\text{-}1$$

where n_d and n_a are the donor and acceptor concentrations respectively. In the presence of only erbium, $n_d=n_a=n_E$.

At an interionic distance of 8Å and above, dipole-dipole interactions are highest. Below 8Å, quadrupole-quadrupole transitions dominate. In a uniformly distributed glass with a rare earth concentration of 10^{26} ions/m^3, the interionic separation is ~13Å, thus dipole-dipole interaction dominates. For highest possible rare earth concentrations of 10^{28} ions/m^3, the interionic separation is ~5Å. If the rare earths are not uniformly distributed, the interionic separation between ion pairs will be smaller than 5Å, thus dipole-quadrupole or quadrupole-quadrupole transitions dominate.

Consider two ions separated by a small distance R, the energy transfer rate[16] will vary as $R^{-\theta}$, where $\theta=6$ for dipole-dipole interactions, $\theta=8$ for dipole-quadrupole interactions, and $\theta=10$ for quadrupole-quadrupole interactions. The exchange interaction between rare-earth ions is highly anisotropic and this results in a strong angular dependence of the two ions on the transfer rate. It is assumed that in a glass, the angular dependence averages out because all angles are possible. Dexter[17] has shown that the transition probability of an electric dipole process in which a donor ion transfers energy to an acceptor can be written in terms of the fluorescence line shape of the donor $f_d(E)$ and the absorption lineshape of the acceptor $F_a(E)$.

$$P_{da} = \frac{3h^4c^4Q_A}{4\pi R_{da}{}^{\theta} n^4 \tau_{21}} \int \frac{f_d(E)F_a(E)dE}{E^4} \qquad 4.5\text{-}2$$

where $Q_A = \int \sigma_A(E)dE$ and $\sigma_A(E)$ is the absorption cross section found by dividing the absorption coefficient at energy E by the concentration of ions. Q_A is assumed to be concentration independent. Since the value of E in the denominator of the integral is almost a constant over the range of integration, it is usually given the

value at the centre of the overlap region (peak of spectra) and taken outside the integral. These values were determined for Er^{3+}

$$Q_A = 1.0\times10^{-20}\left(m^{-1}\right)^{-1} = 1.0\times10^{-18}\left(cm^{-1}\right)^{-1}$$

$$\int f_s(E)F_A(E)dE = 5.8\times10^{-5}\left(m^{-1}\right)^{-1} = 5.8\times10^{-3}\left(cm^{-1}\right)^{-1}$$

using the above values and taking $R_{da} = 13\text{Å}$, $\tau = 10\times10^{-3}$s P_{da}, was calculated as $P_{da} = 2.9\times10^{2}s^{-1}$.

If R_0 is defined as the critical distance, such that when $R_{da} = R_0$, then $P_{da}\tau = 1$, it follows that

$$P_{da} = \left(\frac{R_0}{R_{da}}\right)^6 \frac{1}{\tau} \qquad 4.5\text{-}3$$

From equation 4.5-3 R_0=15.5Å. For distances greater than R_0, the effect of electric dipole energy is small. For Er concentration corresponding to R_0 see figure 4.16. The transfer coefficients in the rate equations k_{ij} can be related to the transition probabilities by

$$k_{ij}N_a = \frac{N_a R_0^6}{(N_a + N_d)\tau R_{da}^6} \qquad 4.5\text{-}4$$

Combining equations 4.5-1 and 4.5-4

$$k_{ij}N_a \approx \frac{17.6N_a R_0^6 (N_a + N_d)}{\tau_d} \qquad 4.5\text{-}5$$

It is important to note that transfer coefficients are not constants but depend on ion concentration when ions are randomly distributed. A plot of equation 4.5-5 showing the linear relation between the upconversion coefficient and the total ion concentration is shown in figure 4.16.

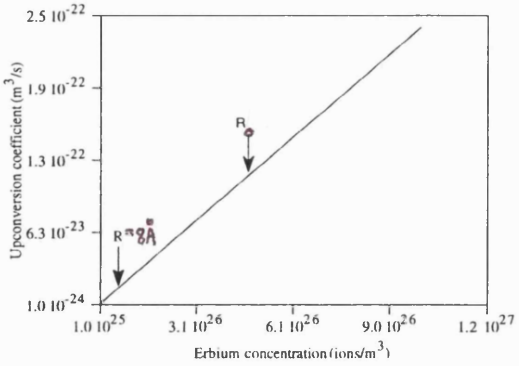

Figure 4.16. Graph of upconversion coefficient versus erbium concentration.

For concentrations on the left of R=8Å the transfer coefficients are negligible, for concentrations on the right of R_o the linear relation breaks down, quadrupole-dipole interactions or quadrupole-quadrupole interactions dominate. Lifetime was assumed not to vary with concentration.

The empirical formula relating observed lifetime, τ_{obs}, to the ion concentration[18] n_{Er} is

$$\tau_{obs} = \frac{\tau_o}{1+(n_{Er}/Q)^2} \qquad 4.5\text{-}6$$

where τ_o is the lifetime for an isolated ion, Q the quenching concentration is $4-6\times10^{20}\,\text{ions}/\text{cm}^3$. Unfortunately, because the concentration at which ion-ion interactions become important were determined empirically, the above equation may not be accurate for all glasses. The magnitude of ion-ion interactions is dependent on ion separation which is related to concentration for a randomly distributed dopant only. The maximum effect on the upconversion coefficient of a lifetime variation would be a change of an order of magnitude.

In the presence of ion pairs, the time dependence of fluorescence decay shows a fast and a slow component, corresponding to ion pairs and a uniform random distribution of erbium ions respectively (see chapter 6). For very high pump powers, the intensity of the emission in the slow and fast components is proportional to the number of ions in the uniform distribution and in ion pairs. Increasing the Er^{3+} concentration beyond the onset of ion pairs formation will not

significantly reduce the interionic background separation, but increases the proportion of ions which form ion pairs. Thus for a non uniformly distributed glass, the average lifetime of the metastable level will not decrease significantly with an increase of Er^{3+} concentration.

For ion pairs the transfer coefficients are constants independent of concentration, but dependent on ion pair separation R_{da}=3.5-5Å. For high pump powers, ion pairs of same rare-earth species have a deleterious effect on gain because transfer rates are much faster than radiative decay. In the high pump regime, ion pairs effectively act as absorbers only. The amount of ion pair formation depends on the fabrication process and the concentration of codopants used. Non uniform dopant distribution in glasses containing two rare-earths might enhance the desired fast interaction between donors and acceptors of different species. The potential for these doubly doped glasses is discussed in the future work section of chapter 7.

References

1. K. Arai, H. Namikawa, K. Kumata, and T. Honda, 'Aluminium or phosphorous co-doping effects on the fluorescence and structural properties of neodymium-doped silica glass', J. Appl. Phys., **59**, pp. 3430-3436 (1986).

2. M.W. Kim, W.J. Cho, J.C. Jo, and S.S. Choi, '1.55 mm gain in a short Er^{3+} and Tm^{3+}-doped heavy metal fluoride glass fibre', Jpn. J. Appl. Phys., **30A**, pp. 2020-2025 (1991).

3. J. Shmulovich, A. Wong, Y.H. Wong, P.C. Becker, A.J. Bruce and R. Adar, 'Er^{3+} glass waveguide amplifier at 1.55 mm on silicon', Electron. Lett., **9**, pp. 1181-1182, (1992).

4. P. Blixt, J. Nilsson, T. Carlnas and B. Jaskorzynska, 'Concentration-dependent upconversion in Er^{3+}-doped fiber amplifiers: experiments and modelling', IEE Trans. Photonics Technol. Lett., **3**, pp. 996-998, (1991).

5. E. Desurvire, 'Study of the complex atomic susceptibility of erbium-doped fibre amplifiers.' J. Lightwave Technol., **8**, 10, pp. 1517-1527, (1990).

6. G.P. Agrawal, 'Fast-fourier-transform based beam-propagation model for stripe-geometry semiconductor lasers: inclusion of axial effects', J. Appl. Phys., **56**, pp. 3100-3109, (1984).

7. M. Federighi, I. Massarek, P.F. Trwoga, 'Optical amplification in thin film waveguides with high Er concentration', IEEE Photonics Technol. Lett., **5**, 2, pp.227-229, (1993).

8. F. Di Pasquale, M. Zoboli, M. Federighi, I. Massarek, 'Finite-element modelling of silica waveguide amplifiers with high erbium concentration', to be published J. Quantum Electron.

9. G.P. Agrawal, W.B Joyce, R.W. Dixon and M. Lax, 'Beam-propagation analysis of stripe-geometry semiconductor lasers: threshold behaviour', Appl. Phys. Lett., **43**, pp.11-13, (1983).

10. A. Brenier, R. Moncorge, and C. Pedrini, 'Er^{3+} -Tm^{3+} energy transfer in $YLiF_4$ (YLF)', IEEE J. Quantum Electron., **26**, 6, pp.967-971 (1990).

11. T. Kitagawa, K. Hattori, K. Shuto, M. Yasu, M. Kobayashi and M. Horiguchi, 'Amplification in erbium-doped silica based planar lightwave circuits', SPIE Proc. Santa Fe, PDpp.1-4 (1992).

12. I. Massarek, P.F. Trwoga, M. Federighi, 'Ion-ion interactions in waveguides with high Er concentration', ECIO Proc., **3**,.pp.40-41(1993).

13. M.D. Shinn and W.A. Sibley, 'Eu^{2+}-sensitized Mn^{2+}luminescence in $RbMgF_3$:Eu,Mn', Phys. Rev.B, **29**, 7, pp.3834-3842 (1983).

14. E. Delevaque, T Georges, M. Monerie, P. Lamouler, and J.-F. Bayon, 'Modeling of pair-induced quenching in erbium-doped silicate fibers', IEEE Photonics Technol. Lett., **5**, 1, pp. 73-75 (1993).

15. C.Y. Chen, R.R. Petrin, D.C. Yeh, and W.A. Sibley, 'Concentration-dependent energy transfer processes in Er^{3+}- and Tm^{3+}- doped heavy-metal fluoride glass', Opt. Lett., **14**, 9, pp. 432-434, (1989).

16. J.C. Wright, 'Radiationless processes in molecules and condensed phases' Topics Appl. Phys., Springer-Verlag Berlin, **15**, pp. 239-295, (1976).

17. D.L. Dexter, 'A theory of sensitized luminescence in solids', J. Chem Phys., **21,** 5, pp. 838-850, (1952).

18. W. Miniscalco, 'Erbium-doped glasses for fiber amplifiers at 1500nm', J. Lightwave Technol., **9**, 2, pp. 234-250, (1991).

Chapter 5: Process and analysis techniques

Abstract

In this chapter, the process used for depositing thin film waveguides is presented. The chapter begins with an overview of other techniques used for deposition and the advantages of PECVD over these methods. A brief introduction to plasmas is given and is followed by a review on how PECVD works as a non-equilibrium deposition process.

The apparatus used in this project is described, giving particular emphasis to the adaptations required in the gas delivery system for the co-deposition of Er^{3+}-doped silicates. The process procedure is discussed.

A range of analytical methods was used to measure the film properties. The compositional analysis was done by AES and RBS. X-ray diffraction, used for Er_2O_3 only, provided a rapid estimate of stoichiometry. A stylus instrument was used to measure film thickness. The refractive indices and film thicknesses were studied using ellipsometry and optical waveguiding. A spectrometer was used to investigate absorption and fluorescence spectra. Lifetime measurements were performed using a fast diode detector, an oscilloscope and a chopped excitation laser beam.

Experimental methods are discussed in this chapter, results are presented in the following chapter.

5.1. Comparison of PECVD with other processes

The waveguides of interest in this research have two distinctive characteristics: very high Er^{3+} concentration and compatibility with component forming techniques such as photolithography. High Er^{3+} concentrations are necessary to achieve gains of a few dBs in a waveguide a few cm long. For use in integrated optics, the waveguide must be on the same substrate as the passive components; it is therefore necessary that the deposition process must not damage previously built devices, or jeopardise subsequent component forming steps.

Several techniques have been used to deposit Er^{3+}-doped silicate waveguides. Metal organic chemical vapour deposition[1, 2] (MOCVD) is generally used for the fabrication of optical silica based fibres. MOCVD relies on pyrolitic dissociation of the precursor chemical vapours. The high temperatures required for MOCVD, post deposition annealing and fibre pulling, lead to clustering of the rare-earth ions. Thus, even though low concentrations of erbium in silica waveguides have been deposited, high concentrations are not readily achieved. Furthermore, MOCVD is incompatible with component forming techniques such as diffusion and photolithography.

Ion exchange waveguides have been made in erbium doped glass[3,4]. To avoid phase separation of components in melt glass, erbium concentration must be kept low. Furthermore, this technique is not readily adaptable for use in integrated circuits on silicon wafers.

Er^{3+}-doped sodium calcium silicate glass has been fabricated by RF sputtering on oxidised silicon wafers[5]. These waveguides may be integrated, although the process gives little direct control over the rare-earth concentration. The films are prepared using glass targets so the Er^{3+} concentration can only be within the limit of established glass forming techniques.

Recently, rare-earth doped silica waveguides on Si have been fabricated by flame hydrolysis deposition and aerosol doping[6]. The doping levels are dependent on the strength of the aqueous solution of the rare-earth chloride and delivery rate of the aerosol to the burner. This technique gives relatively poor control of the rare-earth concentration, results in high water incorporation, and requires a 1350°C anneal to consolidate the soot. When the project started, the idea of using an aqueous rare-earth chloride aerosol in the PECVD system was discarded because it was believed that the high water content and subsequent anneal would result in a high concentration of clusters. This initial hypothesis was confirmed by Bebbington[6], who found that aerosol doped glasses show clustering at relatively low Er^{3+} concentration of 0.1 and 0.5wt%.

Silicon dioxide waveguides are conventionally formed using equilibrium techniques such as thermal oxidation from the silicon substrate at temperature greater than 1000°C. For integrated optics, thin film deposition must be performed at low temperatures so that any underlying interconnections or device structures are not modified. The weakly ionised non-equilibrium plasma used in PECVD permits

lowering of the deposition temperature[7]. Using this non-equilibrium process, the glass phase may be adjusted independently of thermal phases and thus high Er^{3+} concentrations may be achieved.

5.2. Plasma deposition

A comprehensive analysis of the physics of plasma is given by Bittencourt[8]. Chapman[9] describes in detail glow discharges as applied to plasma processes such as PECVD. Plasma processing provides a versatile way of etching, depositing and cleaning thin films. Plasma processing is widely used by the semiconductor micro-electronics industry.

A plasma, the fourth state of matter, consists of an ionised gas with positively and negatively ionised charges and neutral molecules. The plasma used in the PECVD deposition process has a very low degree of ionisation (10^{-4}) and thus consists mainly of neutrals. The two basic inelastic processes in a plasma are excitation and relaxation, and then ionisation and recombination. For the discharge to be sustained, ionisation must equal recombination; this is achieved by the application of a radiofrequency (RF) voltage across parallel electrodes immersed in the gas. The parameter which determines the strength of the collisions in a plasma and the rate of relaxation to thermal equilibrium is the number of electrons in the Debye sphere where λ, the Debye length , is defined as

$$\lambda = \left(\frac{\varepsilon_o kT}{n_e e^2} \right)^{1/2} \qquad 5.2\text{-}1$$

where ε_0= permittivity of free space, k = Boltzmann's constant, T = temperature, n_e= electron density, e = electronic charge. As a whole, a plasma is an equipotential, but at each point in space and time, a net charge exists. The Debye sphere is the space in which this charge is felt. (In a laboratory plasma $n_e=10^{10}/cm^3$, kT=2eV, λ=105μm.) The glow discharge used for PECVD deposition is a relatively collisionless plasma.

A plasma will respond to applied voltages by forming a sheath around the electrodes. This occurs because the particles are free to move. Initially, since electrons are more mobile than ions, an isolated substrate builds up negative charge. The plasma is perturbed, ions are attracted to the substrate, and a steady state is reached. This process is known as Debye shielding. The glow of a plasma is due to

the relaxation of atoms excited by electron impact. Glow intensity depends on the number of excited electrons. Thus, the electron deficient sheath can be seen as a dark space.

The electric field applied between the plates in the reactor causes the breakdown of the gas molecules into a variety of reactive species such as electrons, ions, radicals, atoms and molecules in ground or excited states. The molecules are close to the deposition temperature (300^{o}C), however the effective electron temperature is a factor of 10 or 100 times greater. Under this non-equilibrium condition, the bombardment of neutral atoms by high energy electrons forms reactive species that would normally only occur at high temperatures. Thus high temperature reactions can take place at low temperatures due to the plasma enhancement.

The plasma has a potential V_p which is different from the substrate floating potential V_f. The barrier to electrons is $(V_p - V_f)$. The voltage across the sheath results in the plasma being positive with respect to the substrate and it influences the energy with which an ion strikes the substrate. When an ion enters the sheath, it is accelerated by the voltage and strikes the substrate (after collisions) with a high kinetic energy. The kinetic energy must be high compared with the interatomic binding energies in the growing film. The binding energy of SiO_2 and Al_2O_3 are 51.3kcal/mol and 65.3kcal/mol respectively. Impurities such as water, organics, and polymers have lower binding energies and are etched off by the energetic bombarding ions, leaving the glass intact.

The challenges of plasma deposition arise from the complexity of the non-equilibrium, chemically reactive environment. PECVD has been mainly developed empirically. Due to the extremely complex plasma environment, theoretical understanding of reactive plasmas and their interactions with surfaces is still weak. Our approach to process design was empirical.

The reactor geometry, RF power, and deposition pressure all affect film uniformity and isotropy, as well as the deposition rates and the degree of structural damage in the film. We found that uniformity and isotropy can be improved by using a lower pressure. Charge density decreases at low pressure thus reducing throughput and deposition rates. Similarly, low RF powers result in low charge density and uniform, isotropic films with little damage. However, low RF powers and pressures result in slow depositions. A compromise between film quality and deposition time must be found in order to grow waveguides of a few microns thick in a few hours.

5.3. Apparatus

In this work a Plasma Technology PD80 machine, modified for the co-deposition of any combination of rare-earth oxides, silica, and aluminium oxide is used. The adaptation of the equipment required the design of a multi-line gas and vapour delivery system with control electronics[10].

Figure 5.1 is a schematic of the laboratory layout, showing the multi-line gas delivery system and chamber. Cylinders containing relatively safe gases (N_2O and CF_4 in O_2) are kept in stainless steel cabinets, the cabinets containing the more dangerously toxic, highly flammable, pyrophoric gases and vapours (5%SiH_4 in Ar and TMA, or TMAA) are extracted. 5%SiH_4 in Ar is the silicon precursor. N_2O is used as the oxidising agent. CF_4 in O_2 is the 'cleaning gas'; it is used to etch off unwanted glass deposits from the substrate table and walls in between runs. 5%SiH_4 in Ar is the silicate precursor. TMA and TMAA are the Al precursors.

The gas concentrations are maintained using mass flow controllers (MFC). The MFC and all air actuated valves in the system are controlled using purpose designed electronics. Safety interlocks prevent the user from opening valves when the machine is in a potentially dangerous condition. A mixing manifold located in the main body of the machine is used to mix 5%SiH_4 in Ar, N_2O, Ar, and the Al precursor, or a selection of these gases according to the requirements. The Er precursor is mixed with the other gases and vapours just prior to the heated showerhead. Gases are introduced into the reactor via a shower head in the upper electrode. The water cooling system has been adapted to enable the top electrode to be heated.

An Ar carrier is passed through a bubbler containing TMA, or TMAA kept at a constant temperature (-20°C to 20°C) by a refrigerated bath. The amount of precursor which reaches the reactor is dependent on the vapour pressure, temperature, and on the distance from bubbler to chamber.

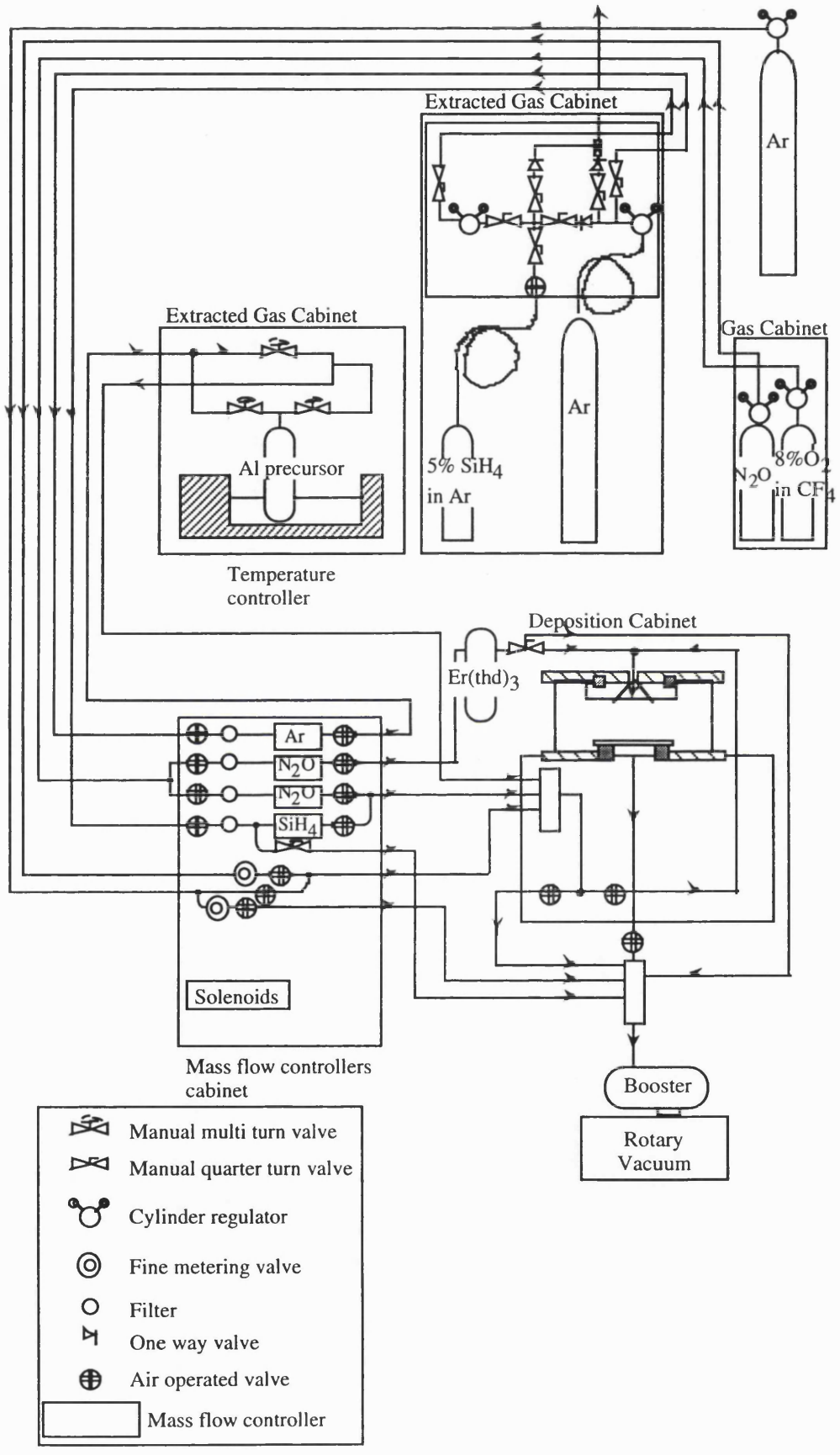

Figure 5.1. Laboratory gas delivery system.

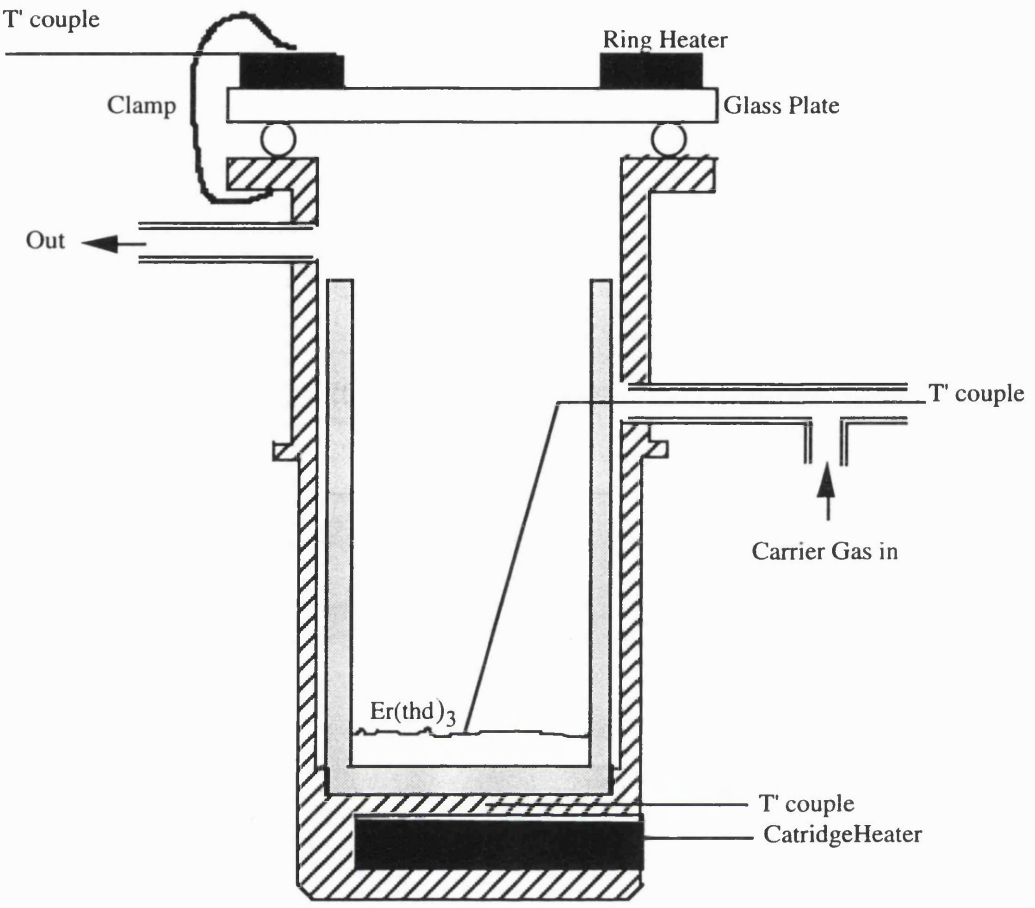

Figue 5.2. Schematic stainless steel heated vessel.

$Er(thd)_3$ is evaporated and kept at a constant temperature (140°C to 160°C) in a heated vessel. It is fed directly into the reactor by a N_2O gas flow. To avoid condensation the connecting tubes are heated. A miniature glass bubbler in an oil bath and heating mantle was initially used. However, condensation of the chelate in the glass lines affected the erbium oxide deposition rate and a new design was required. Figure 5.2 shows a schematic of the final design of the stainless steel heated vessel. The precursor is contained in an aluminium basket inside a heated stainless steel cylinder. A 315W cartridge heater controls the temperature; due to heat losses the heater is set to a slightly higher temperature than required. A thermocouple inserted into the material via the gas inlet measures the exact precursor temperature. The vessel lid is a glass plate through which the precursor can be monitored visually. A 250W ring heater clamped to this glass plate, maintains it at 100°C. A thermocouple is attached to the ring heater to avoid overheating of the glass which would melt the o-ring below it. To eliminate all condensation, heater tape is wrapped around the inlet pipe and the outlet flexible

stainless steel pipe. A second rare-earth or an Al chelate may be added using a second bubbler and heated pipes similar to the one described above.

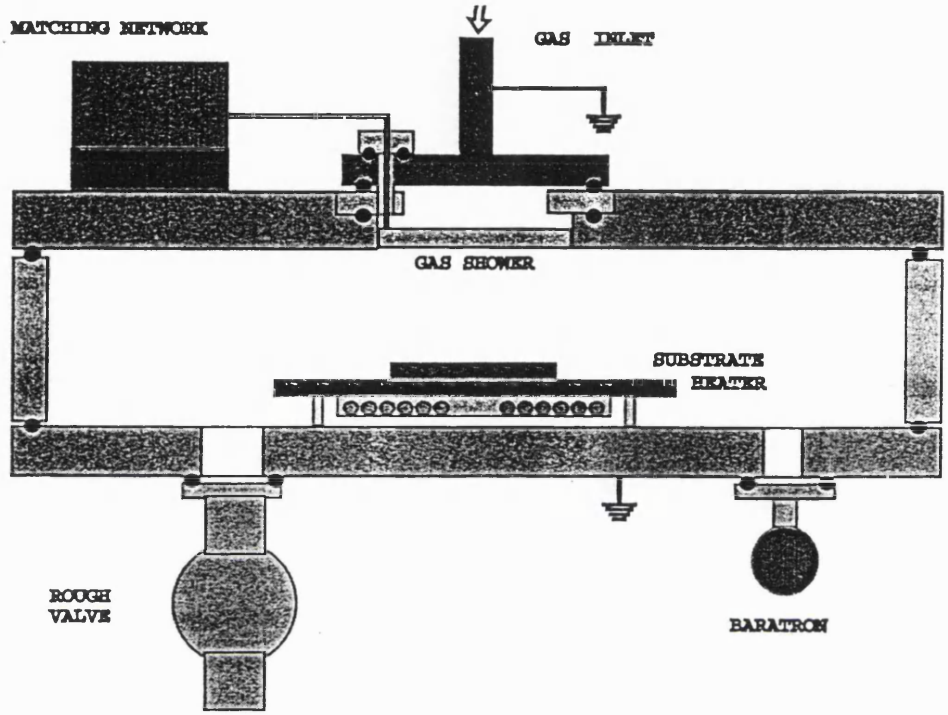

Figure 5.3. Schematic of the reactor.

Figure 5.3 shows a schematic of the reactor. The upper electrode is driven by a RF power supply. Two generators may be used: a low frequency generator which can supply up to 800W over the frequency range of 30 to 100kHz, and a high frequency generator which can supply up to 250W at 13.56MHz. The generator is connected to the top plate of the chamber via an impedance matching network. A rotary pump and booster combination are used to evacuate the chamber. A manual screw-down throttle valve controls the pumping outlet gas transconductance and thus the chamber pressure. The system's base pressure is of the order of 1-10mtorr, deposition pressures are generally in the 100-500mtorr range. The substrate table may be heated by a temperature controller and the heater power supplied via the table legs (max. temperature 400^{o}C). It is earthed and also acts as the lower electrode.

5.4. Film growth

Three types of substrates were used: fused quartz slides, silicon wafers, and thermally grown silica on silicon wafers. On the day preceding the runs the substrates were cleaned using trichloroethylene (with ultrasonic agitation), acetone, and isopropyl alcohol (IPA). They were then rinsed in de-ionised water and placed in a bath of hydrogen peroxide to which concentrated sulphuric acid was added. They were kept in the 50:50 H_2O_2:H_2SO_4 solution for 20 minutes, and were then rinsed in running de-ionised water and finally blown dry. The cleaning procedure was performed in clean room conditions.

Immediately prior to deposition, the substrates were taken from the clean room to the PECVD laboratory. They were placed on the substrate table and the chamber was pumped down. The temperature controllers for the substrate and precursors were set. The system was left to reach set temperatures and base pressure for about an hour.

The films were finally cleaned for a couple of minutes using an Ar gas glow discharge at 5-20W. The mass flow controllers were set so as to achieve the desired gas flow ratio. Each gas line was tested separately and then all necessary lines were left open. When the temperature and process conditions stabilised, the RF was switched on, set to the desired power, and matched so that the reflected power was a minimum. Throughout the run, process conditions were monitored.

At the end of the deposition, the RF system was switched off, the gas valves were shut, and the substrate table temperature was set to room temperature. The Al vessel was shut and turned to bypass, and the Er vessel was switched to direct evacuation by pumps. This ensured that residual precursor vapours did not contaminate the film surface. Specimens were not removed from the chamber until it reached room temperature. This precaution was added to avoid cracking of the film due to thermal stresses, resulting from a rapid exposure to the air.

Film surface roughness and thickness uniformity were examined using an optical microscope and ellipsometry. The difficulties encountered in producing uniform thick films, free from scattering centres, were attributed to the use of an unsuitable showerhead design. Large area, heated showerheads are widely available from commercial sources. They were not a financially viable alternative but nonetheless made the design and construction of a new showerhead an unnecessary exercise.

With the knowledge that the solution to imperfect film uniformity was available, we proceeded to examine the material composition and active optical properties.

5.5. Compositional analysis

5.5.1. Auger electron spectroscopy

Auger Electron Spectroscopy (AES) is a technique used for composition analysis. AES[11] involves ionisation of core levels by relatively high energy electron beams (>1.5eV) and the detection of the emitted Auger electrons of discrete energy resulting from the core-hole decay. The detection of the emitted Auger electrons is used to find the composition of films. When AES is used in combination with Ar ion etching, a composition versus depth profile may be obtained.

AES is an excellent technique for determining which elements are present in a matrix, however exact concentrations are difficult to determine. Backscattering effects can lead to variations of a factor 2 in concentration determinations. AES is performed using very high current densities of 0.1 Acm^{-2}. This results in charging of the surface which can cause migration of network modifiers such as Na^{+} and Er^{3+} to the bottom of the film. The sensitivity of AES for erbium is about 1%.

5.5.2. Rutherford back scattering

In Rutherford Back Scattering (RBS) the surface of a material is investigated by analysing the kinetic energy transfer of energetic (1MeV) incident ions. Classically, the experiment was performed using incident α particles, but other light ions can be used. If the dimensions of the nucleus are very small, and its charge is large, an α particle passing very close to the nucleus can be scattered by a strong Coulomb repulsion through a large angle during the traversal of a single atom. By measuring the angular distribution of scattered a particles it is possible to determine the composition of a material. The calculation considers only the scattering from heavy atoms to permit for the assumption that the mass of the nucleus is so large compared to that of the α particle, that the nucleus does not recoil appreciably during the scattering process.

For very energetic incident ions such as He^+ and H^+ at 1MeV, scattering cross sections are small. Energy losses due to multiple atom scattering are rare and electronic energy losses cause no deflection of ions. At these energies screening of the scattering potential is very weak and a Coulomb interaction may be used. Rutherford scattering experiments can give absolute surface and subsurface compositions. RBS works well for the study of high atomic number elements, (Z_{Er}=167) in low Z matrices, because scattering cross sections are proportional to Z^2, and for light elements, the low energy scattered ions are superimposed on a large background of scattering from heavier atoms.

5.5.3. X-ray crystallography

X-ray diffraction was used to probe the crystalline structure of Er_2O_3. The geometry of X-ray reflections is well documented[12].

5.6. Thickness measurements

A step was made on the deposited film by masking a portion of the substrate during deposition. Using a simple probe instrument, the Talystep, the film thickness was measured. A Talystep consists of a stylus which has a small tip and a light load to limit penetration of the surface. The instrument measures the vertical movement of the stylus travelling across the sample surface. The vertical displacement is converted to a signal which is then amplified and recorded on a strip chart. A wide variety of vertical amplifications are available, thus film thicknesses from about 20Å to 10μ can be measured.

For very thin films it was found the masking technique did not give satisfactory results. On removing the mask, the step produced was not always well defined. Figure 5.4a) shows how on removal of the mask, a film on the step boundary may be thicker than the average film thickness. Figure 5.4b) shows that if the mask is not adhering perfectly, a film can grow underneath the mask, resulting in an underestimate of the thickness.

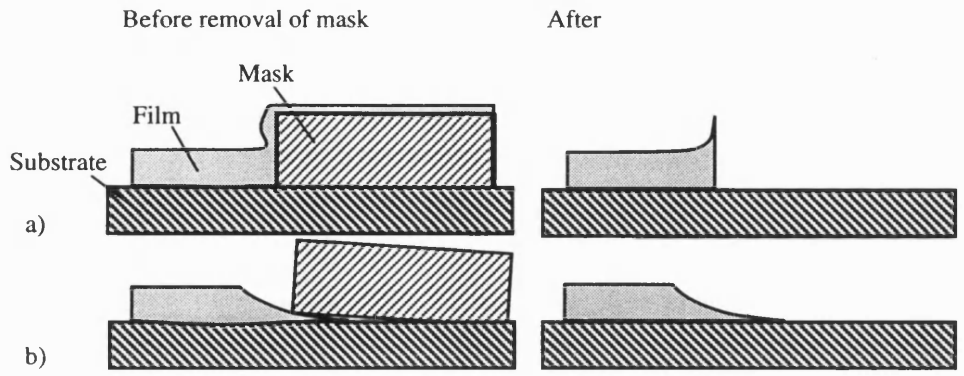

Figure 5.4. Masking a film may produce an ill-defined step. a) measured thickness too large b) measured thickness too small.

For very thin films, thicknesses measured with an ellipsometer (see 5.4.4) were more accurate. For thick films, the Talystep measurement was used to determine which ellipsometer order was correct.

5.7. Optical investigations

5.7.1. Prism coupling

Using a simple prism coupler[13] it is possible to measure the guiding properties, refractive index, loss, and thickness of a guide. A prism is placed above the thin film guide and is separated from it by a small gap of lower refractive index. The incident light is totally reflected at the base of the prism, the waves in the film and prism are coupled through the evanescent fields in the gap. By changing the angle of incidence of the laser beam, any of the waveguide modes may be excited.

Coupling takes place along the entire width of the incident beam. For strong coupling, the components parallel to the gap must be equal for the wave in the prism and the film. The wave vector, k, of the incident light can be divided into components parallel and perpendicular to the gap; the parallel component is $kn_4\sin\phi_4$, where n_4 is the refractive index of the prism, and ϕ_4 is the angle of incidence of the laser beam. Each wave mode propagates along the coupling direction with a different phase velocity v. When the direction of the incident beam is such that $kn_4\sin\phi_4=ß$, where ß is the propagation constant (ß=l/v) of one of the modes, one has efficient coupling, that is transfer of energy from prism to film and back again.

Film inhomogeneities cause scattering of the optical energy of the guided modes into other modes. When a symmetrical prism is used, some light is coupled out again and a series of bright lines, the so-called 'm'-lines, are observed. The total internally reflected beam is seen as a bright spot at the base of the prism. Inside this spot, a dark line which represents the energy lost from the excited mode by the scattering is sometimes visible. Each m line represents a mode; from the position of these lines, the mode angles, it is possible to calculate the refractive index and the thickness of the film using equation 2.1-8. Equation 2.1-8 is solved numerically[14]. The program calculates the thickness and the refractive index of the film from the β/k values of the mode lines.

Material	n_s	n_f	n_c	a_{TE}	h^1 (m)	h^3 (m)	h^{1*}(m)
Al_2O_3	1.46	1.65	1	1.9	0.5	1.6	
Er_2O_3	1.46	1.78	1	1	0.3	0.9	
Er-SiO_2	1.46	1.58	1	4.2	1.1	3.5	2.8
Er-SiO_2	1.46	1.55	1	9.5	2.6	8	6.4

h^1 thickness at which one mode can be sustained for λ= 632.8nm

h^3 thickness at which three modes can be sustained for λ=632.8nm.

h^{1*} thickness at which one mode can be sustained for λ=1535nm.

Table 5.1. Thicknesses at which materials of interest to this thesis sustain 1 mode at 1535nm and 632.8nm.

It was not deemed necessary to calculate the refractive indices and thicknesses of all the films. However, prism coupling was used as a fast method of assessing whether a film guided before trying more time consuming end firing methods. The number of modes present in the visible region was used to estimate the thickness of the guide by using equation 2.1-16. Table 5.1 shows typical waveguide parameters for the materials analysed. For good light confinement and polarisation independence, the Er^{3+} doped silicate waveguide should be monomode at λ=1535nm which is equivalent to a two to three moded waveguide at λ=632.8nm.

5.7.2 Transverse coupling

End firing or transverse coupling is the most direct method of coupling light into a waveguide and was used in some of the lifetime measurements and absorption loss

estimates. The TE polarised laser light is coupled into the end of a waveguide using a lens[15]. Micropositioners are used in order to position the input beam accurately with respect to the film. The ends of the waveguides must be polished (glass) or cleaved (SiO_2 on Si) and clean to avoid losses.

5.7.3 Colour comparisons

The variation of colour with film thickness has long been known. A common gauge is available for SiO_2 films on silicon. Different film thicknesses result in different colours. Direct comparisons of an unknown sample with the silica are made. Care must be taken not to confuse two film thicknesses which give rise to similar colours but in different orders. This can be done by comparing the colours of the films while varying the angle of observation. For films with a refractive index close to that of silicon dioxide, colour comparisons can be done for thicknesses between 500Å to 15000Å with an accuracy of ±100Å over most of the region. The detailed colour chart used is from Pliskin and Conrad[16]. At normal incidence the thickness is given by

$$d = \frac{N\lambda}{2n_2} \qquad 5.7.3\text{-}1$$

where N is the integral order number, n_2 is the refractive index of the film, and λ is the wavelength of the incident light. Using equation 5.6.3-1 we expected that a film of slightly higher refractive index than silica (such as Er^{3+}-SiO_2) would be thinner than the same colour silica film. This technique is a fast and reliable method of estimating film thickness.

5.7.4 Ellipsometry

Ellipsometry provides a fast reliable method for measuring both thickness and refractive index. The amount of literature on the ellipsometer is vast[17] and good computer controlled ellipsometers are widely available. Ellipsometry is based on evaluating the change in the state of polarisation for light reflected from a substrate. The state of polarisation is determined by the relative amplitude of the parallel component, ρ_p, and the perpendicular component, ρ_s, of radiation and the phase difference between the components, D_p-D_s. On reflection from a surface, the ratio ρ_p/ρ_s, and the phase difference undergo changes which are dependent on the

optical constants of the substrate n_3 and k_3, the angle of incidence θ, and n_2 k_2 of the film and film thickness d. If the optical constants of the substrate are known, and $k_2=0$, that is the film is non absorbing at incident wavelength, then the only unknowns d and n_3 can be determined.

In a typical ellipsometer, a He-Ne laser light is linearly polarised and then elliptically polarised by a compensator. After reflection from the sample, the light is transmitted through a second polariser which analyses the polarisation. Finally, the light intensity is detected by a photomultiplier. The angle of incidence and reflection can be varied but are generally set at 45° from the substrate plane. Triple angle measurements are used to calculate the thicknesses of very thick films.

The user places the sample on the ellipsometer, levels the sample table, and aligns the optics in order to maximise the signal intensity. The computer then rotates the polariser and analyser until extinction is obtained. The ellipticity caused by the polariser compensator and analyser combination is the opposite of that produced by reflection from the film and substrate. The four independent polariser and analyser readings which give extinction are picked. From these readings, the phase difference and amplitude ratio are determined and the refractive index and thickness values given.

The ellipsometer technique is accurate, however not all film thicknesses can be used when only one laser wavelength is available. When the thickness is $t \cong n\lambda/2$, the lines of constant refractive index merge and the refractive indices cannot be determined. The most accurate results are those obtained from films whose thickness is furthest from these positions of order change. A silica film, 1000Å in thickness, appears blue, this thickness is half way between the zeroth order and the first order.

The ellipsometers used were all calibrated for silica films deposited on Si and were only used to measure the thickness and refractive index of samples grown on Si. Prior to depositing thick films, a trial blue thin film was deposited with the same deposition parameters. The blue thickness film was used to get an estimate of the refractive index and deposition rates. If the thick film could not be measured because its thickness was on an interference order change, the refractive index measured on the blue film was used.

5.7.5. Absorption spectrometer

Figure 5.5 is a schematic of the visible to near infrared spectrometer assembled for the study of rare earth doped thin films.

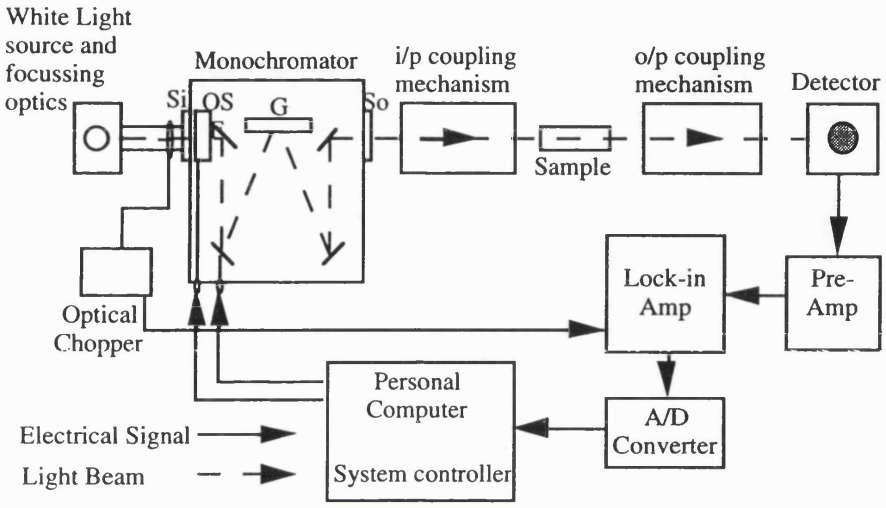

Figure 5.5. Block diagram of loss-measurement system.

The dashed line shows the optical path from the source to the detector via the chopper disk, monochromator entrance slit (Si), order sorting filter (OS), mirrors, grating (g), exit slit (So), input coupling mechanism, sample and output coupling mechanism. The part of the optical signal which has not been absorbed, and thus reaches the detector, is converted to an electrical signal and sent to the signal processing unit. The signal is amplified, then amplified again using the lock-in amplifier to minimise noise, and then converted to a digital signal by the integrating A/D converter. The digital signal can now be read by a computer where signal averaging and calculations are performed to produce loss and absorption data for the sample analysed. To calibrate the response of the system, sample and reference scans are performed using the same system configuration and parameters. The spectrometer can be used over the range 350-1600nm, using two gratings: a 1800 lines/mm grating for the visible region, and a 600 lines/mm grating for the near infrared region. A silicon pin detector is used between 350nm and 1200nm and an InGaAs diode is used for the rest of the range. The InGaAs diode can be cooled if necessary to improve the signal-to-noise ratio.

Waveguide coupling can be achieved by end firing and fibre butt coupling. Figure 5.6 shows the absorption spectrum obtained from an erbium oxide film deposited on silica by PECVD. This spectrum is a transmission spectrum, not a guiding one.

The Er^{3+}-ion characteristic absorption features are superimposed on a decaying expanding sinusoidal feature. This periodic feature is characteristic of thin films and is due to interference effects. In this sample, the peaks of the absorption bands at 380nm and 520nm can be seen while the 635nm and 820nm peaks are masked by the thin film interference oscillations.

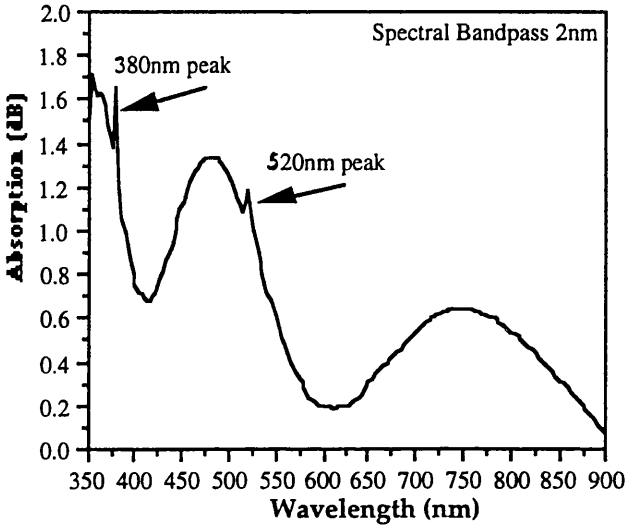

Figure 5.6. Absorption spectrum of an Er^{3+} doped film showing thin-film interference effects.

By end firing into the films, guiding absorption spectra were attempted. The measurement of loss spectra of PECVD grown films was abandoned for several reasons. End firing into waveguides can be very time consuming. The intrinsic loss of the unannealed films was very high, making the absorption peaks barely detectable above the background loss. The annealed films should result in better spectra, however due to time constraints, priority was given to measuring fluorescence spectra.

5.7.6. Fluorescence spectrometer

The spectrometer equipment and software can be used both for absorption and fluorescence spectra. The fluorescence measurement set up is shown in figure 5.7. The thin films were pumped using either a tuneable Ar^+ ion laser with power output of 0-4W, or a tuneable Ti:sapphire laser (780nm-1000nm), power 0-2W. The laser light passes through the chopper disk and impinges upon the sample which is at the focal point of the lens (l_1). Since focusing can cause damage to the film, l_1 was

only used for films which showed weak fluorescence. The sample is mounted at the brewster angle[18] for the incident light which assures that all polarised laser light is transmitted. The transmitted light collected by lens 2 passes through the monochromator. The signal detection, amplification, A-D conversion, and recording are as described for the absorption spectrometer.

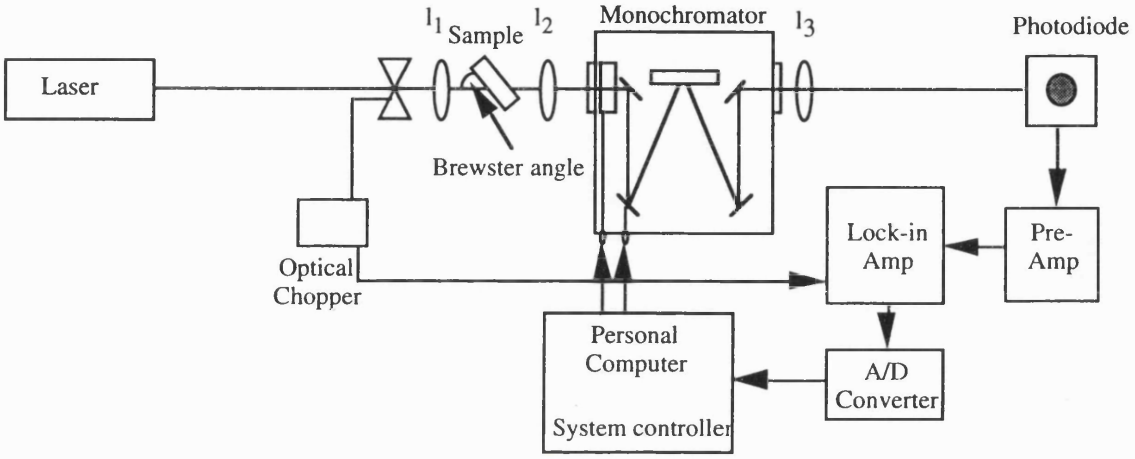

Figue 5.7. Block diagram of fluorescence measurement system.

5.7.7. Fluorescence lifetimes

The lifetime measurements were taken using the spectrometer shown in figure 5.7 above. The output from the pre-amplifier was recorded by a digital storage oscilloscope. The oscilloscope was triggered from the mechanical optical-beam chopper. The average read out of fall and rise times was displayed on the oscilloscope screen and plotted. From the trace (see Ch. 6) it is possible to make direct measurements of the lifetime.

Lifetimes of 2-3 ms were measured. The reason for these relatively short lifetimes is discussed in chapter 6. In order to get a sufficiently large signal the films required annealing, two temperatures were used; 900°C and 1200°C. Lifetimes of a few μs cannot be measured using a chopper and oscilloscope and were not attempted. The μs lifetimes are an indication of the presence of ion-pairs, as will be discussed in section 6.7.

References

1. S.B. Poole, D.N. Payne, and M.E. Fermann, 'Fabrication of low-loss optical fibres containing rare-earth ions', Electron. Lett., **21**, pp.737-739 (1985).

2. R.J. Mears, L. Reekie, I.M. Jauncey and D.N. Payne, 'Low noise erbium-doped fibre amplifiers operating at 1.54mm', Electron. Lett., **23**, pp.1026-1028 (1987).

3. B.P. Howell and T. Beerling, 'Evaluation of ion exchange for fabrication of rare-earth doped waveguides', Proc. SPIE , **836**, pp.44-47 (1987).

4. E.K. Mwarania, L. Reekie, J. Wang and J.S. Wilkinson, 'Low threshold monomode ion-exchanged waveguide lasers in neodymium-doped BK-7 glass', Electron. Lett., **26**, pp.1317-1318 (1990).

5. J. Shmulovich, A.Wong, Y.H. Wong, P.C. Becker, A.J. Bruce and R. Adar, 'Er^{3+} glass waveguide amplifier at 1.5mm on silicon', Electron. Lett., **28**, 13, pp.1181-1182 (1992).

6. J.A. Bebbington, G. Barbarossa, J.R. Bonar and J.S. Atchinson, 'Rare-earth doped silica waveguides on a Si fabricated by flame hydrolysis deposition and aeresol doping', Appl. Phys. Lett., **62**, 4, pp.337-339 (1993).

7. A.H. Bailey and C.W. Pitt, 'Plasma deposition of metal oxide films for integrated optics', Vacuum, **36**, pp.139-142 (1986).

8. J.A. Bittencourt, 'Fundamentals of plasma physics', Oxford Pergamon Press (1986).

9. B. Chapman, 'Glow discharge processes', Wiley (1980).

10. P. Trwoga, M.Phil transfer thesis, UCL (1993).

11. D.P. Woodruff and T.A. Delchar, 'Modern techniques of surface science' Cambridge Solid State Series (1986).

12. N.F.M. Henry, H. Lipson and W.A. Wooster, 'The interpretation of x-ray diffraction photographs', Macmillan (1951).

13. P. Tien and R. Ulrich ,'Theory of prism coupler and thin film light guides', J. Opt. Soc. Am., **60**, 10, pp.1325 -1337 (1970).

14. H. Robinson, 'Waveguide electro-optic modulators using the parallel-plate configuration', Ph.D. thesis, University College, London (1991).

15. M.V. Plissi, 'Rare-earth doped waveguide laser devices', Ph.D. thesis, University College, London (1993).

16. W.A. Pliskin and E.E. Conrad, 'Nondestructive determination of thickness and refractive index of transparent films', IBM J. Res. Develop., **8**, pp.43-51 (1964).

17. L.I. Maissel and R. Glang, 'Handbook of thin film technology', Mc-Graw Hill (1970).

18. M. Born and E. Wolf, 'Principles of optics. Electromagnetic theory of propagation inteference and diffraction of light', 6th Ed. (1991).

Chapter 6: Experimental results

Introduction

The aim of this project was to determine the feasibility of using PECVD to dope silicate glass with erbium. The emphasis of the deposition programme was on the development of fluorescing thin films with high dopant concentrations in the available project time. Thus a thorough characterisation of growth kinetics to produce uniform, very low loss material, was beyond the scope of the programme. The film characteristics would be significantly improved by depositing the films in clean room conditions and by ensuring minimum atmospheric contamination in the gas lines.

The first step was that of depositing the three glass components separately. The reasons for the choice of precursors used for deposition of silica, erbia and alumina are presented. 5% silane in argon was used for silica. The rare-earth precursors chosen are chelates of 2,2,6,6-tetramethyl-3,5-heptanedione. For historical reasons trimethylaluminium (TMA) was used as the source of aluminium. Calibration runs using these three precursors are presented. The PECVD reaction is a complex process in which many variables must be monitored and controlled. These variables are: RF power, RF frequency, electrode separation, electrode temperature, pressure, and reactive gas ratio. Each variable influences the end result to some degree, however it would have been too time consuming to optimise each one for a given process. The effects of electrode temperature and RF frequency were investigated for Al_2O_3. That of RF power, pressure, and gas ratio were analysed for SiO_2 and Er_2O_3.

The next step was that of combining the three components to form alumino-silicates, erbium silicate, and erbium alumino-silicates. The mixture of the alumina and silica processes resulted in highly carbonated films and it was decided that the Al source would need to be changed to improve results. Increasingly high erbia concentrations and silica were combined. In PECVD, solubility problems do not limit the amount of Er^{3+} which can be incorporated into the silica matrix and thus the role of aluminium as a clustering reducing codopant lost its relevance. Alumina is not needed to eliminate solvation problems, it is however necessary to increase the bandwidth of the spectra and to reduce the ion pair concentration. Fluorescence spectra and metastable lifetimes of Er^{3+}-doped films were measured. A log plot of the lifetime decay curve did not result in a straight line, as would be expected from

a single exponential lifetime due to randomly distributed ions. This indicates the presence of ion pairs in the glass.

6.1. Alumina

Al and P may be added to silicate waveguides to change the refractive index step, modify the fluorescence spectra, and to reduce clustering of rare-earths. PECVD technology is well established. Routinely and reproducibly grown optical quality Al_2O_3 films are not readily achieved. For work in this thesis, trimethylaluminium, (TMA), $Al(CH_3)_3$ is used as the aluminium precursor. TMA is highly volatile and is compatible with PECVD as demonstrated by Catherine and Talebian[1,2] and A. Bailey at UCL[3]. The direct bond between carbon and aluminium in its molecule must be broken in order to produce Al_2O_3 films with low carbon content.

6.1.1. Alumina films

Initially, the results obtained by A. Bailey[3] were reproduced. The TMA was cooled using water and dry ice. The precursor was carried to the chamber by an Ar carrier gas and Al_2O_3 was formed by the reaction of TMA and O_2. It was immediately apparent that a more reliable way of cooling and maintaining set temperatures would result in more reproducible results. An extracted cabinet containing a temperature controller and refrigerated bath was installed. The controller ensured reproducibility of the temperature conditions to within 0.1°C and minimised variations of the aluminium concentration in the chamber due to temperature drift. For safety and minimum air contamination, all lines to and from the bubbler are now in stainless steel.

The TMA vapour pressure equation is: $\log_{10}P = 10.475 - 2780/T$, where P is pressure in mmHg, and T is temperature in K. From the bubbler temperature and the gas flow rate, the amount of TMA that reaches the chamber can now be estimated. For example: 100sccm of TMA in Ar at 0°C is approximately 0.3sccm of pure TMA.

To investigate the background reaction rate of TMA with O_2, a run was performed without a plasma. The substrate was heated to 100°C, 20sccm of O_2, and TMA vapour at 19°C carried by 50sccm of Ar were delivered into the chamber. This experiment resulted in a cracked, non-uniform film, deposited at a rate of 50Å/min.

Normal deposition rates at 19°C vapour pressure were about 1000Å/min. If, for sake of argument, we assume that the natural reaction rate of TMA and O_2 is not affected by the production of radicals in the plasma (only 1 in 10^{-4} molecules present are ionised), then 5% of the film deposited is due to this background reaction. This rather high contamination can be removed completely by using N_2O, instead of O_2, as the oxidising agent. On comparison, by viewing the surfaces of relatively thick films (approximately 3μm) under the microscope, it was observed that the films obtained using O_2 showed irregularities such as crystallites and specs of powder, whereas those produced with N_2O were generally clear.

Details of alumina samples deposited by reacting TMA and N_2O are shown in table 6.1.

Sample	Flow Rate[a] TMA:N_2O (sccm)	Pressure (mTorr)	Elec T (°C)	RF Power[b] (W)	Refractive Index	Deposition Rate[c] (Å/min)	Composition Al:O:C:N
S1	0.07:50	241	100	100*		1000	
S2	0.07:50	276	200	100*		130	
S3	0.07:50	272	300	100*	1.77	200	26:49:11:7
S4	0.07:50	301	356	100*		300	
S5	0.07:50	259	300	150*	1.71	460	
AL1	0.1:20	136	300	12.5*	1.81	50	29:52:10:5
AL4	0.1:20	141	300	12.5*	1.59	20	
AL6	0.1:20	140	300	12.5*	1.59	10	
AL7	0.1:20	137	300	62.5*	1.65	170	38:57:1:0
AY2	0.3:50	135	300	12.5*	1.69	310	
AY4	0.3:50	139	300	62.5*	1.57	390	
AY5	0.3:50	150	300	25*	1.63	320	
AY6	0.3:50	150	300	37.5*	1.61	340	
AY7	0.3:50	132	300	0		0	
AY8	0.3:50	130	300	50*	1.55	430	
AY45	0.6:50	191	300	5	1.535	280	
AY46	0.6:50	190	300	5	1.581	620	
AY49	0.6:50	195	300	10	1.555	310	
AY54	0.6:50	214	280	30	1.587	380	
AY53	0.6:50	189	300	2.5	1.565	140	
AY51	0.6:50	215	300	20	1.589	320	
AY55	0.6:50	222	300	40	1.576	480	

[a]The quoted gas flows are for pure TMA. That is 100sccm TMA carried by Ar at 0°C corresponds to 0.3sccm of pure TMA, and 100sccm at 10°C corresponds to 0.6 sccm of pure TMA.
[b]Samples marked * were deposited at 90kHz, the unmarked ones were deposited at 13.56MHz.
[c]Deposition rates are quoted to the nearest 10Å.
For samples whose thickness was not close to an ellipsometric period, multiple angle measurements were taken. These give thickness and refractive index with a larger uncertainty.

Table 6.1. Alumina sample identification and description.

In agreement with the results by Catherine and Talebian[1], the deposition rate of aluminium oxide was found to decrease with an increase in substrate temperature. The results of AES, (see figure 6.5) suggest that this decrease in deposition rate may be due to a change in the evaporation rate of the dissociated TMA at the substrate, combined with more effective etching of unwanted organic molecules. The quality of the films: thickness uniformity, adherence to substrate, presence of imperfections, improved quite markedly as temperatures increased. Figure 6.1 and figure 6.3 are graphs of refractive index versus power at 90kHz and 13.56MHz respectively. At 90kHz the index range is 1.55 to 1.70, the highest indices being deposited at lowest powers. This trend is not seen at 13.56MHz where the index range is from 1.53 to 1.59.

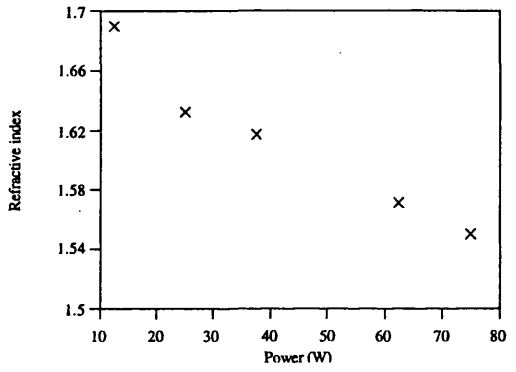

Figure 6.1. Graph of refractive index versus deposition power for alumina films deposited at 90kHz.

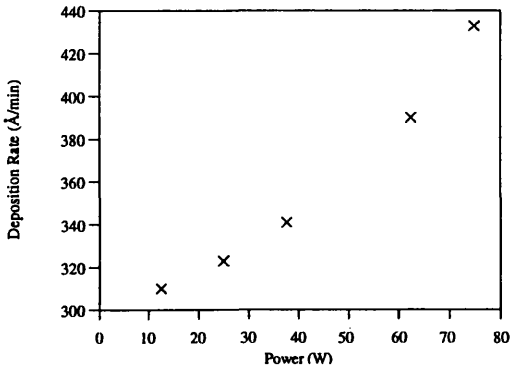

Figure 6.2. Graph of deposition rate versus power for alumina films deposited at 90kHz.

The deposition rate of the films was dependent on power. Figure 6.2 and figure 6.4 show graphs of deposition rates versus power at 90kHz and 13.56MHz respectively. The film thickness uniformity was better at low powers for both deposition frequencies.

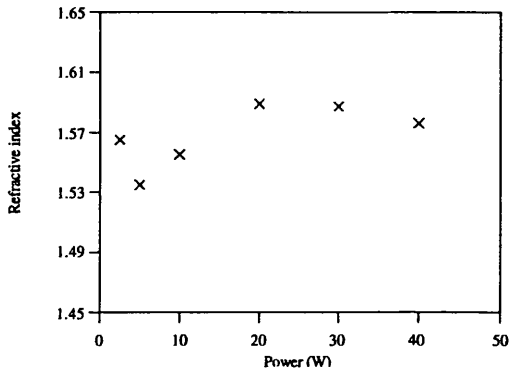

Figure 6.3. Graph of refractive index versus deposition power for alumina films deposited at 13.56MHz.

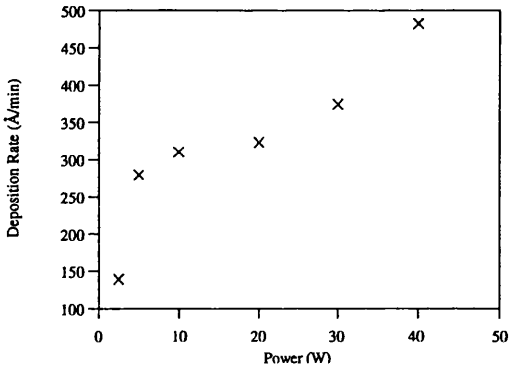

Figure 6.4. Graph of deposition rate versus power for alumina films deposited at 13.56MHz

In figure 6.5 the AES depth profiles of films S3, Al1, and Al7 are presented. The concentration of aluminium oxygen and carbon is in atomic %. The depth scales were calibrated by assuming the density of the films to be similar to that of Al_2O_3 and using sputtering rates equivalent to that of an Al_2O_3 film. AES on the films deposited at 90kHz showed a carbon content of 10% at 12.5W(Al1) and less than 1% at 62.5W(Al7). The film with high carbon content had little elemental aluminium (unbound aluminium atoms) and a relatively high refractive index. This indicates that at 12.5W and 90kHz, the power was not sufficient to break up the TMA molecule efficiently. The film (S3) deposited at 100°C and 100W had a

carbon contamination of 15%, demonstrating that substrate table temperature as well as power have a significant role in breaking Al-C bonds.

The AES compositional analysis of 3 films deposited at 13.56MHz at three different powers is shown in figure 6.6. The carbon content of the films deposited at 13.56 was <1% and was not affected by power.

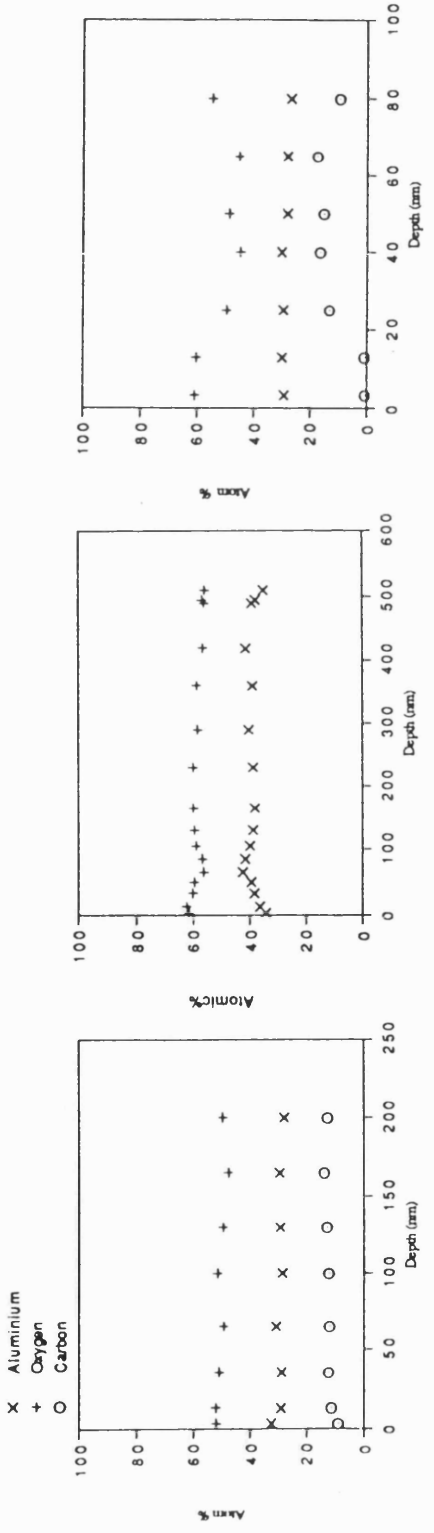

Figure 6.5. AES depth profiles for 3 films deposited at 90kHz. The deposition conditions for A1, A17 and S3 are presented in table 6.1.

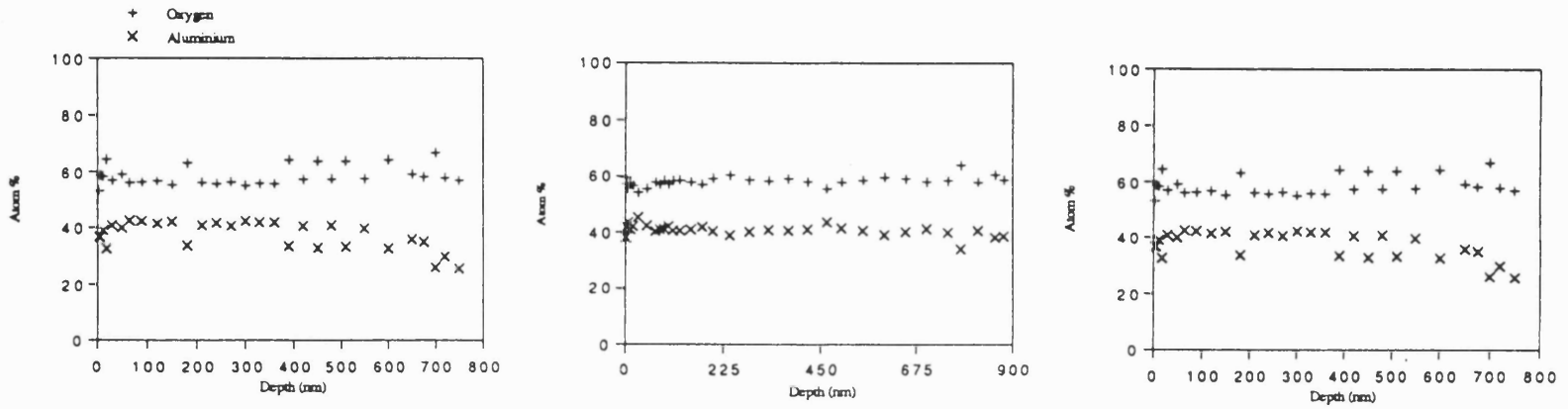

Figure 6.6. AES depth profiles for 3 films deposited at 13.56kHz. The deposition conditions for AY51, AY53 and AY54 are presented in table 6.1.

In summary, the initial investigations of Al_2O_3 deposited by PECVD using two generators and different deposition temperatures have been presented. Temperatures below 300°C resulted in poor quality films with high C contamination. The samples deposited at 13.56MHz had lower C content than those deposited using 90kHz. The fact that the 13.56MHz generator was more easily and reproducibly matched may account for the 13.56MHz RF generator being more effective at dissociating the TMA molecule. The best quality films were deposited using the 13.56MHz generator and substrate temperatures of 300°C.

6.2. Silica

The deposition of optical quality silica films by PECVD is a well characterised process. Several precursors (SiH_4, $SiCl_4$, TEOS) and oxidising agents (N_2O, C_2O, O_2) may be employed. Any of the conventionally used methods of depositing pure, or doped silica, can be adapted for codeposition with rare-earths. Our choice of SiH_4 as the Si precursor was regulated by its widespread use in industry. It is diluted to 5%SiH_4 in Ar, other inert gases such as He, or N, and different SiH_4 concentrations may be used. Low SiH_4 content results in slow silica deposition rates.

A set of preliminary experiments comparing, under identical conditions, O_2 and N_2O showed that film uniformity was better for the N_2O depositions. N_2O has the added advantage of not reacting spontaneously with SiH_4 and can thus be mixed with the precursors prior to the reaction chamber. The bond dissociation energy for N_2O is 1.7eV, which is a relatively low in comparison with other oxidising agents (CO_2 = 5.5eV, O_2 = 5.2eV). To produce stoichiometric films, ratios of 7:1, N_2O:SiH_4 have been used[4]. The overall reaction of nitrous oxide with silane[5] is

$$SiH_4 + 2N_2O = SiO_2 + 2N_2 + 2H_2$$

The possible mechanisms for the reaction may be explained as follows; nitrous oxide has two resonant electronic structures

$$-N{=}N^{+}{=}O \qquad \text{and} \qquad N{=}N^{+}{-}O^{-}$$

The nitrogen-nitrogen bonds have higher bond energies than the nitrogen-oxygen bonds or the silicon-hydrogen bonds. If SiH_4 is predominantly dissociated in the

plasma, SiH_2 or SiH radicals could form intermediate complexes of the type shown below:

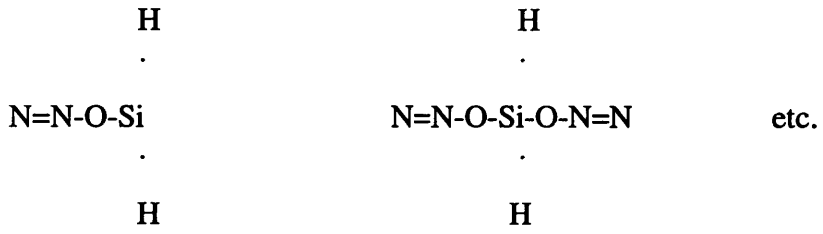

These complexes decompose to SiO_2 and $N_2 + H_2$.
The nitrogen-oxygen single bond energy is a factor 2 or 3 lower than the silicon-oxygen bonds.

6.2.1. Silica films

Two silane delivery arrangements were used, the second experimental set-up used was presented in chapter 5. The silica deposition system optimisation had to be repeated. Details of some silica samples deposited by reacting 5%SiH_4 and N_2O are shown in table 6.2. Most of the results obtained using the first silane set-up have not been included because an air inlet through a faulty regulator had an adverse effect on the silica quality.

Five minute runs were repeated at different powers and pressures. All other parameters were kept constant: table temperature was 300°C and mass flow ratio of N_2O:SiH_4 was 40:1. The results from the calibration runs are shown in the graphs in figures 6.7 and 6.8. For wafers which had large variations in thickness, the central value was used.

Sample[a]	Refractive index, n	Thickness[b] (Å)	Deposition Rate[b] (Å/min)	Flow Rate[c] SiH_4:N_2O (sccm)	RF Power (W)
AX22	1.465	980	200	2.5:100	5
AX19	1.465	960	200	2.5:100	5
AX20	1.465	1650	330	2.5:100	5
AX21	1.462	1600	320	2.5100	5
AX28	1.464	2105	420	2.5100	5
AX25	1.468	2350	470	2.5:100	5
AX26	1.464	1470	290	2.5:100	10
AX27	1.471	2330	470	2.5:100	10
AX29	1.465	2620	520	2.5:100	10
AX24	1.466	2810	560	2.5:100	10
AX36	1.464	1580	320	2.5:100	15
AX37	1.453	2560	510	2.5:100	15
AX38	1.472	-	-	2.5:100	15
AX9	1.463	-	-	2.5:100	15
AX33	1.465	2163	430	2.5100	20
AX35	1.465	-	-	2.5:100	20
AX34	1.464	-	-	2.5:100	20
AX30	1.463	-	-	2.5:100	20
CX32*^	1.484	1210	120	5:40	5
CX43*	1.490	6400	128	5:40	5
AY46*	1.480	1230		5:40	5
AY35*^	1.507	950	95	5:40	5
CY36*	1.505	1230	123	5:40	5
AS4*	1.500	-	128	5:40	12.5
TR	1.493	1570	157	5:40	5
BY39*^	1.462	5005	125	5:40	5

[a]Samples marked * were deposited in the presence of air inlet by a faulty regulator.
Samples marked ^ were deposited at 100°C, all others were deposited at 300°C.
[b]Deposition rate and thickness are quoted to the nearest 10Å.
For samples whose thickness was not close to an ellipsometric period, multiple angle measurements were taken. These give thickness and refractive index results with a larger uncertainty.
[c]The quoted gas flows are for the 5% SiH_4 in Ar. That is, 50sccm corresponds to 2.5sccm of pure SiH_4.

Table 6.2. Silica sample identification and description.

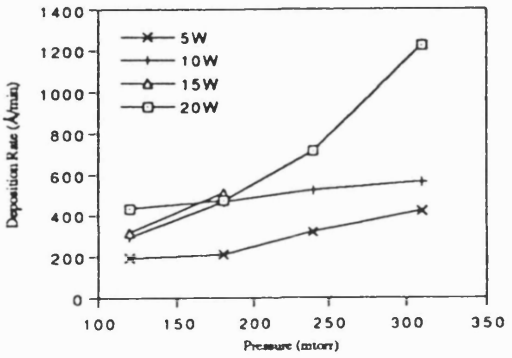

Figure 6.7. Graph showing pressure versus silica deposition rate for different powers.

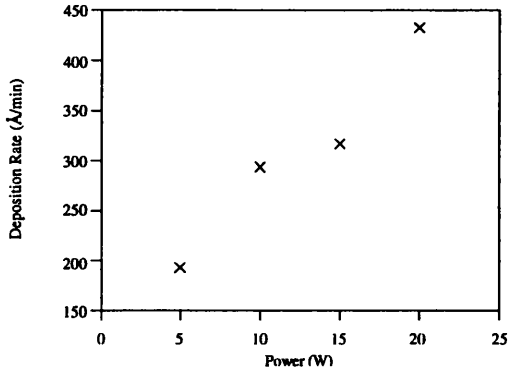

Figure 6.8. Graph showing deposition power versus deposition rate for 124mtorr pressure.

The film uniformity was best for low power and pressure (5W, 120mtorr). As the pressure was increased, films which were thin in the middle and thick at the edges were deposited. For example, the film deposited at 20W and 310mtorr was 800Å thick at centre and 6000Å on edge. The refractive index of the films varied from 1.46 to 1.47 and no trends in change of refractive index with change in power or pressure were visible.

The compositional analysis of a few of the SiO_2 films deposited using the first delivery system was determined using AES. The depth profile for AS4 is shown in figure 6.9. The stoichiometry of the film was 2.1, the slight oxygen abundance of the film is typical of PECVD grown films. The 3%N content of the film is responsible for the slightly raised refractive index. The Er^{3+}-SiO_2 composite glasses deposited in the presence of an air inlet also had a slight N content (see section 6.5.2.).

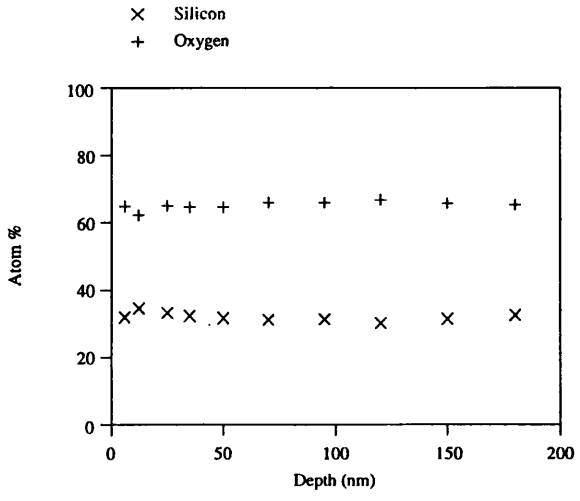

Figure 6.9. AES depth profile of SiO_2 sample AS4. The sample had a N content of about 3%.

6.3. Erbia

The key to growing rare earth films by PECVD is that of finding a compound which may be easily vaporised and is compatible with the low temperature glass forming process. Initially, we considered using erbium chloride ($ErCl_3$), a precursor commonly used in optical fibre fabrication[6], as the source of erbium. To obtain 1mm Hg vapour pressure, $ErCl_3$ must be heated to 1000°C; at typical PECVD temperatures (300°C) the vapour pressure of this compound is insufficient to justify its use. Alternatively, the $ErCl_3$ may be delivered using an aerosol[7], however the use of aerosol doping was discarded because we predicted that the high temperature required to reduce the high water content in films would cause clustering. An extensive literature search was done to find the most volatile rare-earth compound with good thermal stability synthesised to date. The rare-earth tri-chelates of 2,2,6,6-tetramethylheptane-3,5 dione, $Ln(thd)_3$, have sufficiently high vapour pressures[8] at the low temperatures used for PECVD experiments, and can be evaporated without decomposition[9]. K.J. Eisentraut and R.E. Sievers[10] give a detailed account of the synthesis for the preparation of these compounds. The complexes are synthesised from metal nitrates. A. Weber and H. Suhr[11,12,13] used the $Ln(thd)_3$ complexes for PECVD deposition of rare-earth metal and oxide thin films; the application of such films was for high temperature superconductors. They did not produce optical quality films.

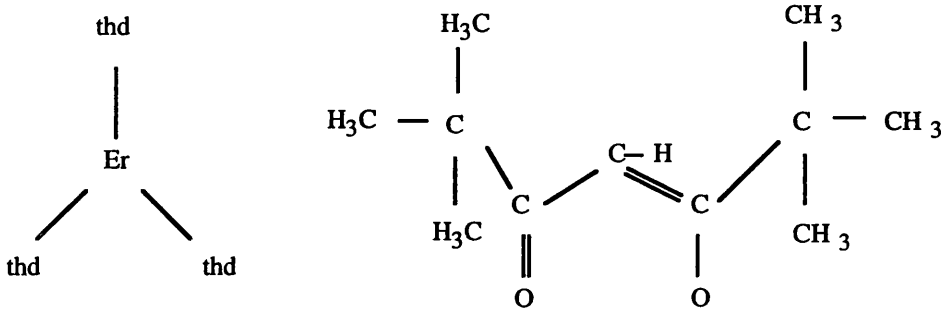

$Er(thd)_3$ thd

Figure 6.10. Structure of Er(thd)3 ligand.

Figure 6.10 shows the structure of the β-ditekonate ligand chosen as the most suitable Er precursor. From figure 6.7 it may be argued that for every atom of erbium in the plasma there will be 33 atoms of carbon and 57 of hydrogen. The radicals and ions produced by the plasma are oxidised to form volatiles when

sufficient O_2 is present. Note that since there are no direct bonds between C atoms and the Er^{3+}-ion, C contamination can be expected to be low. Elemental composition of the materials demonstrates negligible C contamination.

In 1990, R. Tumminelli et al.[14] published the first paper on the fabrication of high concentration rare-earth doped optical fibres using chelates. This paper confirmed our previous choice of the Er precursor as correct. They found that in MOCVD, the high vapour pressure of the rare-earth chelates relative to the vapour pressure of $ErCl_3$ leads to higher concentration of erbium oxide in the fibre. In 1993, while having completed the depositions, and during the writing of this thesis, Shuto et al.[15] reported the fabrication of an erbium doped phosphosilicate glass waveguide amplifier fabricated by PECVD!

6.3.1. Erbia films

Some twenty-three Er_2O_3 films were deposited. The Er_2O_3 was stoichiometric and contained less than 3% C. The waveguides had a refractive index of 1.78±0.01 at 632.8nm and an X-ray diffraction pattern typical of cubic Er_2O_3.

$Er(thd)_3$ is a solid at temperatures below 180°C, while between 180°C and 217°C it is a liquid. The vapour pressure equation[16] for the solid is: $\log_{10}P = 15.526 - 6955.5/T$, where P is pressure in mmHg, and T, the temperature in K, is $410<T<454$. The vapour pressure equation for the liquid is: $\log_{10}P = 10.065 - 4478.3/T$, where P is pressure in mmHg, and T, the temperature in K, is $454<T<490$. For example: 100sccm of $Er(thd)_3$ carried by N_2O at 154°C is approximately 0.02sccm of pure $Er(thd)_3$, and 100sccm of $Er(thd)_3$ carried by N_2O at 164°C is approximately 0.05sccm of pure $Er(thd)_3$. Temperature drifts have a significant effect on the vapour flow rate and thus deposition rate. Table 6.3 shows a sample of the erbia films deposited. The refractive index of Er_2O_3 grown by PECVD is slightly lower than that reported for thermally grown films. The relatively low $Er(thd)_3$ flow rates result in slow deposition rates. It is of interest to note that the deposition rate of Er_2O_3 decreases with power.

Sample	Refractive index, n	Thickness[a] (Å)	Deposition Rate[b] (Å/min)	Flow Rate[b] Er(thd)3 (sccm)	RF Power (W)
CX27	1.768	1100	30	0.04	5
CX28	1.775	9130	30	0.03	5
3.3	1.638	2580	40	0.06	5
3-5	1.777	2600	40	0.06	5
3-7	1.637	260	10	0.04	100
3-10	1.704	830	10	0.04	100
3-4	1.801	990	20	0.04	5
CX31	1.753	3040	20	0.03	5
CX26	1.780	1060	20	0.03	5
CX24	1.677	930	20	0.03	10
CX25	1.671	880	20	0.03	10

[a]Deposition rate and thickness are quoted to the nearest 10Å.
For samples whose thickness was not close to an ellipsometric period, multiple angle measurements were taken. These give thickness and refractive index with a larger uncertainty.
[b]The quoted gas flows are for pure Er(thd)3. That is, 50sccm of Er(thd)3 at 154°C carried by N_2O corresponds to approximately 0.01sccm of pure Er(thd)3.

Table 6.3 Erbia sample identification and description.

The chemical composition of four of the samples was assessed by AES. The depth profiles of three of these samples are shown figure 6.11. The stoichiometry of 1.6, showed a slight oxygen abundance. The extra oxygen may be attributed to the deposition process. This promising characteristic of PECVD Er_2O_3 and PECVD SiO_2 should relax solvation problems when the two components are mixed, as was discussed in chapter 3. The C content of the films was typically smaller than 3At.%. For example the C content of CX28 was ~0.7At%; this is a substantial improvement on the C content reported by Weber for erbia films.

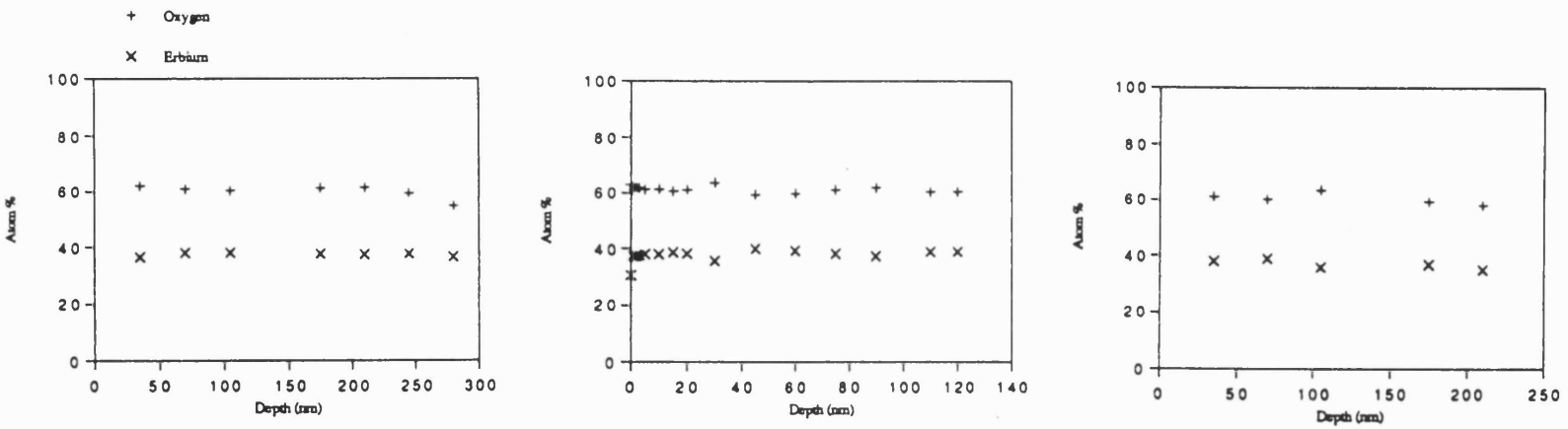

Figure 6.11. AES depth profiles for 3 Er_2O_3 samples. 3.3 and 3.5 had a C content of less than 3%. CX28 had an average C content of 0.7%. The deposition conditions for 3.3, 3.5, and CX28 are presented in table 6.3.

The depth profile of sample CX25 is shown in figure 6.12. The chemical composition showed the presence of small quantities of fluorine and carbon. This unexpected chemical composition was attributed to cleaning the chamber immediately proceeding the deposition of CX25. The chamber was cleaned using a CF_4 and O_2 plasma, followed by a thorough scrub with solvents, and was finally left pumping down over night. Traces of the CF_4 apparently caused the contamination. Having detected this problem we added a step to the chamber cleaning procedure: immediately proceeding a run, a 5 minutes sealing SiO_2 layer was deposited.

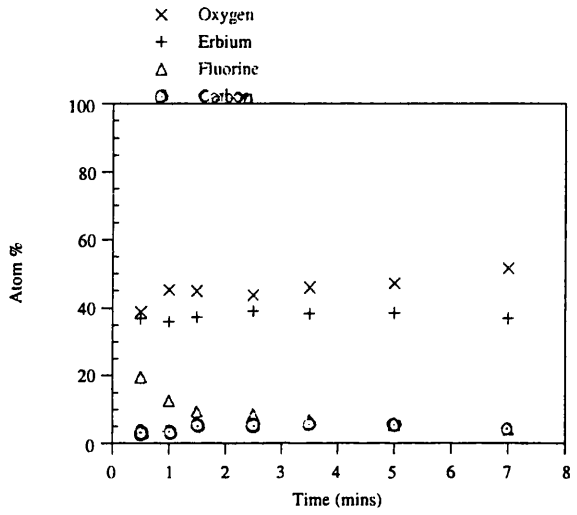

Figure 6.12. AES depth profile of sample CX25. The anomalous composition was attributed to cleaning the chamber immediately prior to the deposition.

AES established that the films had similar chemical composition to pure thermal erbia; the next step was to investigate whether they also had the same crystalline structure. X-ray powder diffraction was used to probe the crystalline structure of the films.

Most of the crystals M_2O_3 are oxides of trivalent metals[17], where M is a rare-earth. Their structures are ionic and do not generally involve strong polarisation. The metal to oxygen radius ratio is an essential factor in determining the type of one of these oxides. The Er_2O_3 radius ratio is 0.67[18]. For radius radii between 0.6 and 0.87 the structure is known as C-M_2O_3[19]. It is a cubic cell containing 16 molecules and thus 80 atoms. The cubic lattice parameter, a, of Er_2O_3 is 10.54Å.

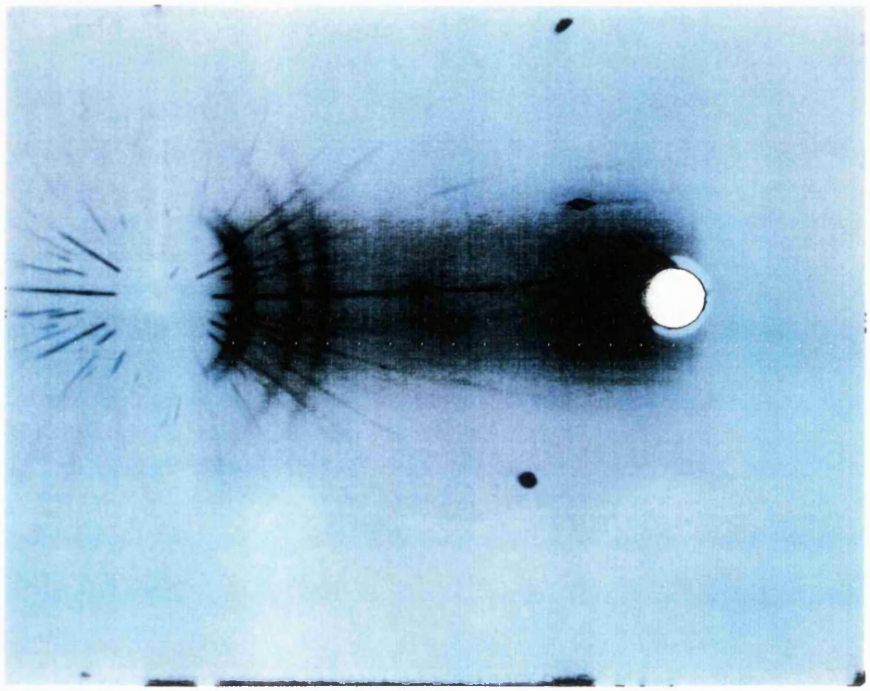

Fig. 6.13. X-ray diffraction pattern of an erbium oxide film on a silicon substrate, deposited at 300^{O}C and 5W by PECVD.

The photograph in figure 6.13 was taken using Ni filtered Cu radiation so that only the Cu-Ka (λ=1.541Å) reflections contributed to the patterns. Figure 6.13 shows the arcs due to unoriented erbium oxide and the straight streaks caused by the underlying silicon substrate. From the powder diffraction X-ray crystallography data file, 19-452, the 4 sharpest Er_2O_3 lines are at 3.045, 2.637, 1.894, 1.590mm. These four lines correspond to the four arcs clearly visible on the photograph shown in figure 6.13.

The author has not found any report in the literature of waveguiding in Er_2O_3. However, Er_2O_3 films sufficiently thick to sustain a mode were demonstrated to waveguide. Using prism coupling, the thicknesses and refractive indices of Er_2O_3 grown on silica were determined. The waveguides had a refractive index of 1.78±0.01 at 632.8nm. This value of refractive index is in close agreement with the indices measured by ellipsometry. The polycrystalline nature of erbia produces high losses thereby limiting potential applications for erbia waveguides. Fluorescence experiments were attempted, but as expected the Er_2O_3 did not fluoresce.

6.4. Alumina silicates

Several alumino-silicates were deposited. The films adhered well to the substrate, did not crack when they were removed from the chamber, and had good thickness uniformity. The results of AES compositional analysis for one of the samples is shown below. The chemical analysis revealed the sample to contain only 5%Si and 20%C. Having analysed different precursor mixtures and deposition powers, the carbon content could not be lowered significantly. It appears that C in TMA is not easily separated from Al.

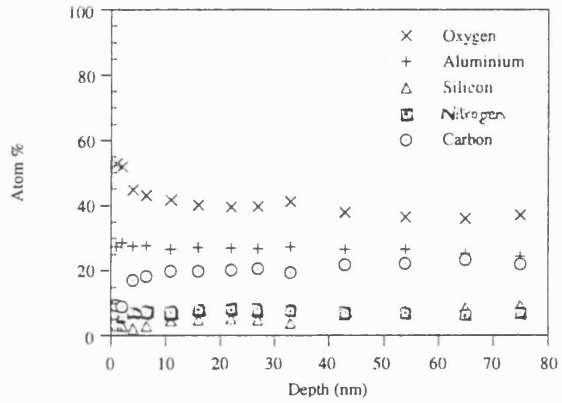

Figure 6.14. AES depth profile of an 'alumino-silicate' sample with high carbon contamination.

The disadvantage of TMA is that C contamination increases when deposition conditions are changed. Another organic precursor, trimethylamine alane ($AlH_3N(CH_3)_3$) TMAA, resulted in lower C contamination than TMA in metalorganic vapour phase epitaxy (MOVPE) of semiconductors[20]. TMMA contains no direct Al-C bonds, and has vapour pressure of 1.8mm at 25°C. The TMA cylinder was replaced by a TMAA one, however no experiments have been performed with the new precursor. The Al chelate, Al(hfa), is suggested as another suitable Al precursor. It can be used in a similar configuration to the $Er(thd)_3$ chelate.

6.5. Erbium doped alumina silicates

The three deposition processes were combined. The first samples obtained were powdery deposits. Lowering the TMA content of the gas mixture resulted in films that cracked on cooling. Reducing the total gas pressure resulted in mottled films which did not have uniform thickness. These experiments were attempted before receiving the alumino-silicate chemical analysis results which showed high carbon contamination. The high carbon content found from the AES analysis was attributed to the TMA precursor as discussed above.

In order to repeat these experiments using a different Al precursor, new calibration runs for Alumina would be required. Priority was given to the investigation of the simpler Er^{3+}-SiO_2 system. It must be remembered that Al is a codopant used to improve the solubility of Er^{3+} in silica and the spectral properties of Er^{3+}-SiO_2. At this stage in the project, it was suspected that the observed oxygen abundance in plasma deposited Er_2O_3 and SiO_2, could lead to highly doped Er^{3+}-SiO_2 without the need of a codopant. The primary objective of the research was to determine whether it is possible to dope silicate glass with high Er^{3+} concentrations. How spectral shape, fluorescence intensity, and lifetime decay are modified by adding a codopant were not investigated further during this project.

6.6. Erbium doped silica

6.6.1. Introduction

The Er_2O_3 and SiO_2 deposition processes were combined. Having previously encountered difficulties in mixing Al_2O_3 and SiO_2, we initially investigated whether a stable glass with an increasingly high Er^{3+} concentration could be deposited. The AES compositional analysis of these runs showed that the Er_2O_3 and SiO_2 maintained their stoichiometric ratios when mixed and that there was no significant increase in C contamination when the conditions were modified.

According to the model developed in chapter 4, maximum gain should be achieved for a concentration of $5x10^{19}$-10^{22} ion/cm^3. Using the AES results, we chose a mass flow ratio that would yield a concentration in the desired range.

The films deposited were a few microns thick and their fluorescence spectra are presented in section 6.5.3. The runs were reproduced and several fluorescing films obtained. The films were annealed and lifetimes of 2-3 ms were measured. Exact concentrations of Er for a few samples were obtained by RBS.

6.6.2. Erbium doped silica

Initially, we investigated whether a stable glass with increasingly high Er^{3+} concentrations could be deposited. A summary of the results for a sample of these films is shown in table 6.4.

Sample[a]	Flow Rate Er(thd)3:SiH4 :N2O (sccm)	Ratio	Thickness[c] (Å)	Deposition Rate[b] (Å/min)	Refractive index, n	RF Power (W)	Er conc.[d]
BCX4*	0.01:1.25	1: 125	3850	128	1.465	20	4 At%^
BCX3*	0.12:5	1:41	9680	80	1.505	10	
1.1*	0.06:5	1:83	1280	284	1.491	5	10 At%^
3.6*	0.03:1.25	1:41	2780	60	1.678	5	36 At%^
AV3*	0.03:2.50	1:83	5 modes		1.544	20	1 At%^
BV3*			28600				
AS3*	0.12:2.50:50	1:20:833	1 mode			5	
S4*	0.02:2.50	1:125	3 modes			5	
AV40	0.02:2.5	1:125	1 mode			5	0.2 10^{21}
BV40			3800				atom/cm^3
ABV40							
AV42	0.02:2.5	1:125	1 mode			5	0.2 10^{21}
BV42			14000				atom/cm^3
ABV42							
AV43	0.04:5:100	1:125:2500	14000			5	0.8 10^{21}
BV43							atom/cm^3
ABV43							
AV44	0.04:5:100	1:125:2500	950			5	
BV44							
ABV44							
AV45	0.04:5:100	1:125:2500	950			5	
BV45							
ABV45							

[a]Samples marked * were deposited in presence of air inlet by a faulty regulator.
[b]Deposition rate and thickness are quoted to the nearest 10Å.
For samples whose thickness was not close to an ellipsometric period, multiple angle measurements were taken. These give thickness and refractive index with a larger uncertainty.
[c]The quoted gas flows are for pure gases and vapours. That is, 50sccm of Er(thd)3 at 154°C carried by N_2O corresponds to 0.01sccm of pure Er(thd)3.
That is 50sccm of 5% SiH_4 in Ar corresponds to 2.5sccm of pure SiH_4.
The N_2O quoted gas flows are for added N_2O.

[d]AES analysis results are marked ^. RBS analysis results are unmarked.

Table 6.4. Erbium doped silica sample identification and description.

The refractive index of the films is related to the ratio of mass flows of $Er(thd)_3$ and SiH_4. AES (table 6.5) demonstrated that the films consist of a mixture of practically stoichiometric Er_2O_3 and SiO_2. This suggests that Er^{3+} sits in an oxygen environment in the matrix. The refractive index of erbia is about 1.78 and is higher than that of silica. As expected, the higher the Er^{3+} concentration in the glass, the higher its refractive index. The C contamination was less than 1% in all films.

ELEMENT	AX28	BCX4	1.1	3.6	CX28
Oxygen	66	65	65	58	60
Silicon	33	31	24	5	0
Carbon	0	0.3	0	1	1
Erbium	0	3.7	11	36	39
Refractive index	1.464	1.465	1.491	1.678	1.78

Table 6.5. AES composition analysis of three Er^{3+}-doped silica films.

The chemical composition of Er^{3+}-SiO_2 with increasing Er^{3+} concentration was determined by AES. The depth profiles of three of these films are presented in figure 6.15. An increase of $Er(thd)_3$ concentration in the plasma (of fixed power), results in higher Er^{3+} concentration in the film. The deposition rate of SiO_2 increases sharply with an increase of power and the deposition rate of Er_2O_3 decreases with power. Thus a similar $Er(thd)_3$:SiH_4 ratio at 5W and 20W will result in the latter film having a lower Er^{3+} concentration than the first.

It was established that stable silica glasses containing high erbia concentrations can be deposited by PECVD, and that the glass matrix stability does not pose restrictions on erbia concentrations. The results of the model presented in chapter 4 indicate that maximum gain should be achieved for dopant concentration in the 10^{20} to 10^{22}ion/cm^3 range. The conversion factors for concentrations in ions/cm^3 to At.% are given in Appendix B.

AV3 was the first waveguiding and fluorescing film deposited. By prism coupling at 632nm, 5 modes were visible for AV3. Using a waveguide analysis program the refractive index, n_f, and thickness, t_f, were calculated from the position of the mode lines: $n_f = 1.544 \pm 0.003$ and $t_f = 2.86 \pm 0.08$. The AES depth profile of AV3 is shown in figure 6.16. The N content responsible for the relatively high refractive index of 1.54, is due to an air inlet into the system. Here, the Er does not appear to

be uniformly distributed in the film. The depletion of the top part of the film may have been caused by a variation in deposition conditions during the run, or by charging of the surface during electron beam bombardment which can cause migration of network modifiers such as Er^{3+} to the bottom of the film. An average value of the Erbium concentration of AV3 is 0.8At.%, which assuming the density of glass to be 2.2g/cm^3, is about 1.8 x10^{20}ions/cm^3.

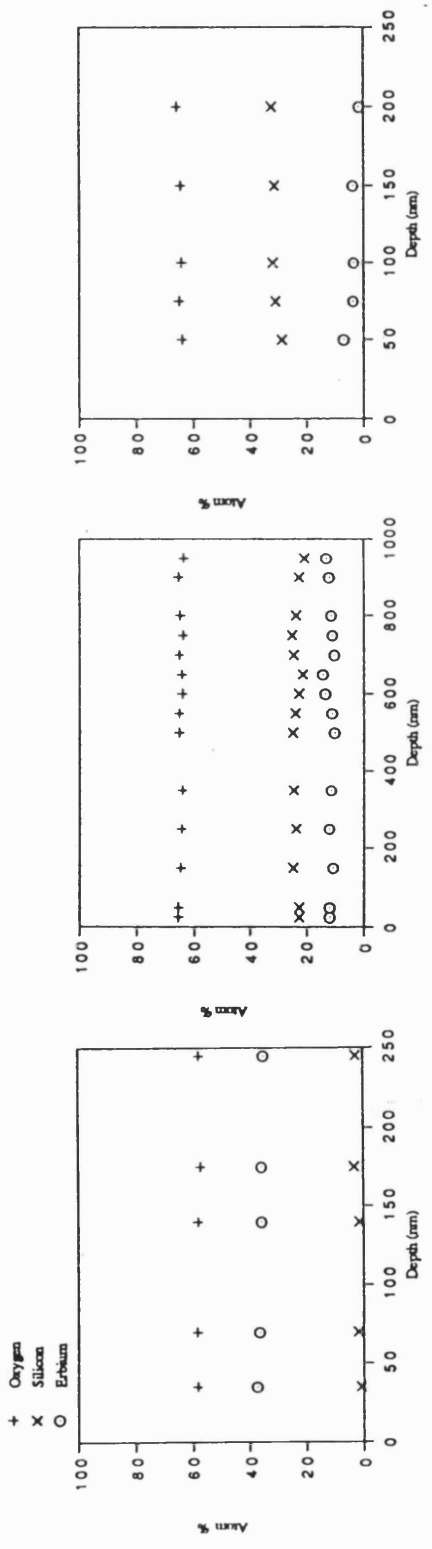

Figure 6.15. AES depth profiles for 3 Er^{3+}-SiO_2 samples doped with different Er^{3+} concentrations. The deposition conditions for BCX4, 1.1, and 3.5 are presented in table 6.4.

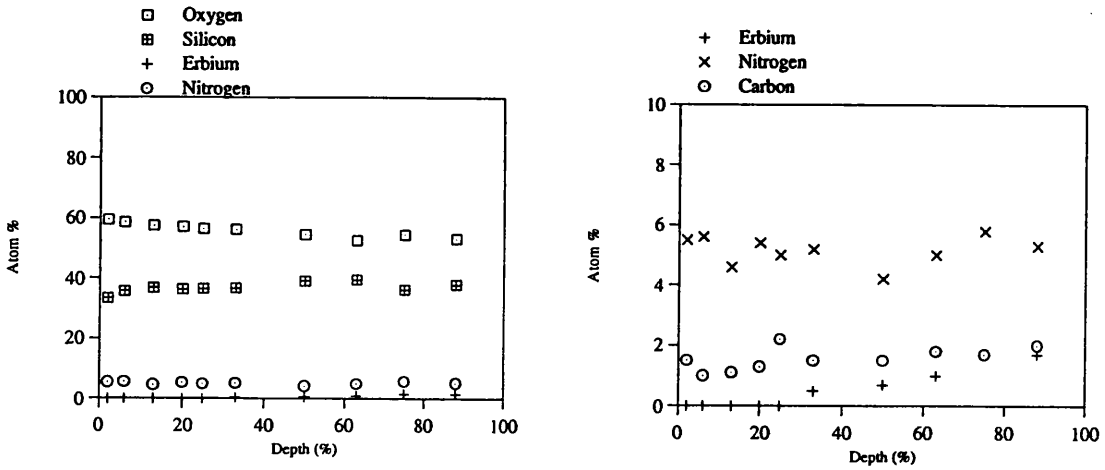

Figure 6.16. AES depth profile of AV3.

The fluorescence spectrum of AV3 is shown in figure 6.17 in section 6.6.3. Having obtained a fluorescing waveguide, other samples in the same concentration range were deposited. The conditions could not be reproduced exactly because the equipment required modifications. Specifically, a faulty SiH_4 regulator required a new SiH_4 delivery system to be installed. The $Er(thd)_3$ glass bubbler and heating mantle were replaced by the stainless steel vessel as described in chapter 5. Before the replacement of the SiH_4 regulator, an air inlet into the system via the regulator produced nitrogen rich films with raised refractive index. The films deposited after the instalment of the new SiH_4 system had lower nitrogen contents and lower indices.

6.6.3. Fluorescence spectra

Several films fluoresced: the spectral shape and bandwidth for all the films was very similar, thus to avoid repetition, not all spectra obtained are presented. The selection has been limited to the spectra of two films of known Er^{3+} concentration.

The spectra were obtained by exciting the Erbium ion using an Ar ion or Ti-Sapphire laser. The emission band at 1535nm is due to the decay of electrons from

the lowest excited state $^4I_{13/2}$ to the ground state $^4I_{15/2}$. The intensity of the emission depends on a number of factors: pump power absorption, quantum efficiency, output at other wavelengths, and glass quality. The lifetime of AV3 before annealing was 9ms. The intensity increased by a factor of 100 on annealing the deposited samples at 900°C. The spectra presented are all normalised by dividing by the integral of the area. The florescence spectrum of AV3 is shown in figure 6.17. The film had an Er^{3+} concentration of about 0.8At.%, and contained about 5At.%N in the SiO_2 matrix. Its refractive index measured by prism coupling was 1.54.

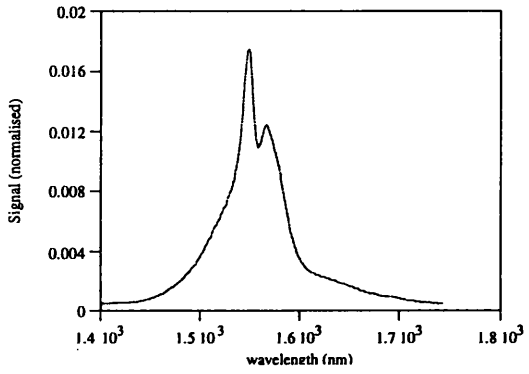

Figure 6.17. Fluorescence spectrum of a sample with n_E ~0.8At.%=1.8x10^{20}ions/cm^3, and lifetime ~2ms. The sample was annealed at 900°C for 90mins.

Figure 6.18 shows the fluorescence decay curve obtained from the same sample. The estimated lifetime of the sample taken from this curve is 2ms.

The fluorescence spectrum obtained after a 1200°C anneal was very similar to that shown above in Fig.6.17, however the intensity was lower. The lifetime was measured as 2.5ms. Table 6.5 shows the variation of peak intensity with annealing temperature, the sample having been pumped using an Ar^+ ion laser at 514.5mm. The decrease of intensity between 900°C and 1200°C is likely to be an indication of a variation in the glass matrix, such as the onset of component clustering. In order to investigate this point further EXAF analysis of the Er^{3+} sites would be necessary.

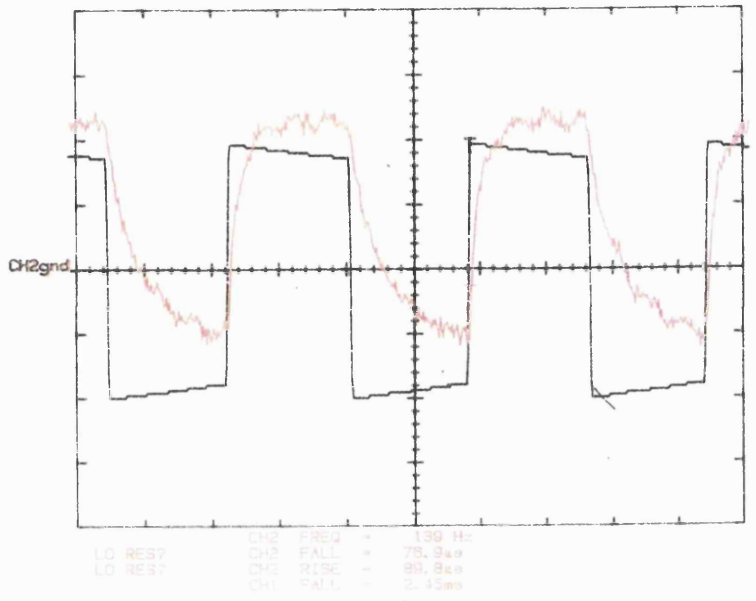

Figure 6.18. Lifetime decay curve for film AV3 with 0.8At% Er^{3+}.

Annealing temperature/^{O}C	Signal intensity (arb Units)
0	10
900	546
1200	285

Table 6.6. Effect of annealing temperature on fluorescence intensity at 1.532nm.

The samples AV40, AV42, and AV43 fluoresced. In order to get a more reliable value of Er^{3+} concentration, the compositional analysis of these films was performed by RBS. The results of the RBS are shown in figure 6.19.

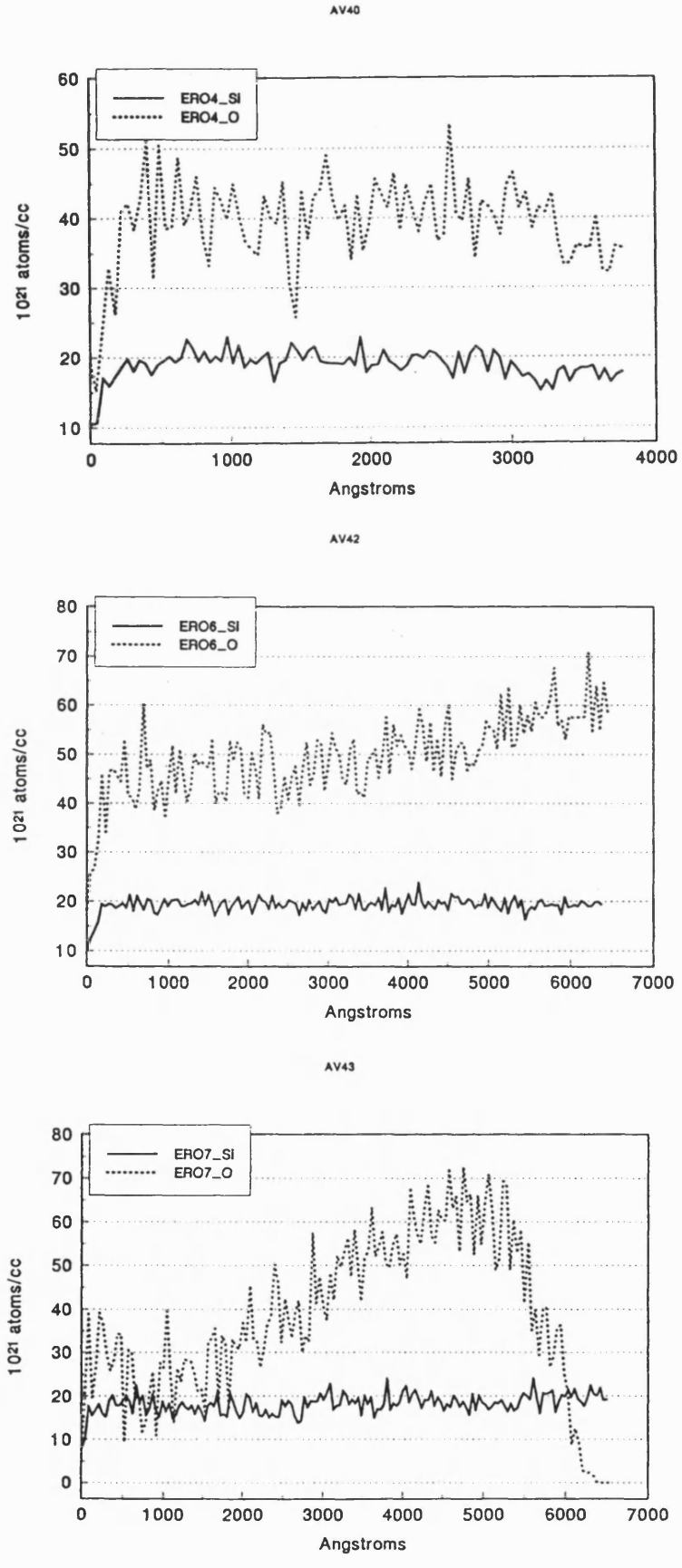

Figure 6.19. Compositional analysis by RBS.

The fluorescence spectrum of AV43 after annealing is shown in figure 6.20. The lifetime was estimated as 2.8ms from a fluorescence decay curve. Assuming the lifetime of the isolated ion to be 9ms, the 3ms lifetime expected from equation 4.5-6 is in close agreement to the experimental measured value of 2.8ms.

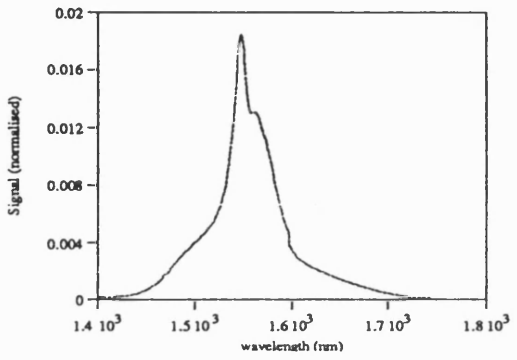

Figure 6.20. Fluorescence spectrum of sample with Er^{3+} concentration ~$1x10^{21}$ atoms/cm^3. Lifetime ~2.8ms. The sample was annealed at 900°C for 90mins.

6.7. Lifetime measurements

The lifetime of unannealed AV3 was measured by Dr. Hempstead at Southampton University. By fitting an exponential to the decay curve the lifetime was measured as 9ms. The logarithm of the curve (Fig. 6.21) resulted in a straight line, showing that the decay was due to a single exponential.

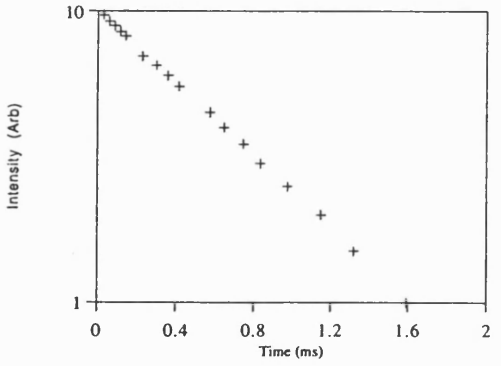

Figure 6.21. Log decay curve of AV3 as deposited.

The lifetime of AV3 after 900°C annealing was 2-3ms depending on power. A strong non-exponential decay was observed for input powers of a few hundred mW. The log decay curve is plotted in Fig. 6.22. The log decay curve was not a straight line, demonstrating the presence of an initial fast decay rate due to ion-pairs. Furthermore, the average lifetime was found to decrease with an increase of pump power. These results are consistent with the cooperative upconversion and cross-relaxation mechanism discussed in chapter 4. Excited ions in the $^4I_{13/2}$ metastable level can transfer energy between themselves in such a way that one ion is excited to the $^4I_{9/2}$ level, while the second ion returns to the ground state. The $^4I_{9/2}$ level will then rapidly relax to the $^4I_{13/2}$ level by non-radiative decay. This produces a decay rate which depends on the excited-state density, as observed. The lifetime tends to 9ms, the value of the isolated ion for low (2mW) pump powers and to 2ms, the value predicted from equation 4.5-6 for high pump powers.

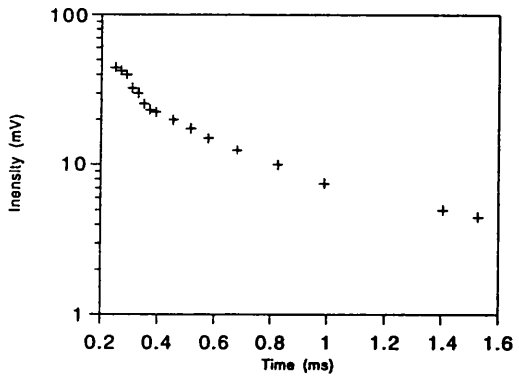

Figure 6.22. Log decay curve of AV3 after 900°C anneal.

Wysoski' et al.[21] predicted the non-exponential decay observed above by modifing the rate equations to account for ion pairs. However, their efforts to observe paired decay were unsuccessful, probably due to insufficient pump powers (<1W). The non-exponential decay observed for input powers of several mW is consistent with results obtained by Wyatt[22] for fibres with Er concentration>1At%. Wyatt showed that for fibers with Er^{3+} concentration <0.1At %, the decay curve is a smooth

exponential with a lifetime of 10-12ms. For these low concentration samples, no significant changes in the decay rate with excitation level are seen . However, for Er concentration>1At% and high pump powers, the decay is non-exponential and is affected by pump power.

Conclusions

The precursors chosen for the silica, alumina and erbia were presented, followed by the results of calibration experiments for each component. The compositional analysis of the films was done by AES. The refractive indices of the films was measured by ellipsometry and prism coupling, and it was 1.78 for Er_2O_3, 1.46 for SiO_2, and in the 1.55-1.8 range for Al_2O_3.

Mixing difficulties were encountered when the TMA and silane chemistry were combined to form alumino-silicates. The resulting films had more than 10At.% of carbon. The reduction of C contamination in the alumino-silicates could be achieved by closer calibration of the process, or by changing the precursors.

It was demonstrated that PECVD silicate glass can be doped with erbium. The $Er(thd)_3$ and silane chemistry were readily combined. Solubility problems do not limit the concentration of erbium. RBS was employed to determine the exact Er^{3+} concentration of a few Er^{3+}-SiO_2 films.

The fluorescence spectra and lifetimes were typical for Er^{3+}-SiO_2 glass. The lifetime measured before annealing was 9ms. A post deposition anneal necessary to eliminate OH^- impurities and reduce losses resulted in the formation of ion pairs. The presence of ion pairs was detected by observing a non-exponential lifetime decay and a decrease of lifetime with an increase of power.

References

1. Y. Catherine and A. Talebian, 'Plasma deposition of aluminium oxide films', J. Electronic Mater., **17**, 2, pp.127-134 (1988).

2. C. Boyrreau and Y. Catherine, 'Effect of deposition temperature on plasma grown aluminium oxide films', J de Phys. **C4**, pp.409-412 (1988).

3. A.H. Bailey, PhD. Thesis, University College, London (1989).

4. A.R. Reinberg, Ann. Rev. Mater. Sci. 9, **341** (1979).

5. J.R. Hollahar and P.S. Rosler, 'Thin film processes', Academic Press (1978).

6. S.B. Poole et al., 'Fabrication and characterisation of low-loss optical fibres containing rare-earth ions', J. Lightwave Technol., **4**, 7, pp. 870-876 (1986).

7. J.A. Bebbington, G. Barbarossa, J.R. Bonar and J.S. Atchinson, 'Rare-earth doped silica waveguides on Si fabricated by flame hydrolysis deposition and aerosol doping', Appl. Phys. Lett., **62**, 4, pp. 337-339 (1993).

8. M.F. Richardson and R.E. Sievers, 'Volatile rare-earth chelates of 1,1,1,5,5,5-hexafluoro-2,4-pentanedione and 1,1,1,2,2,3,3,7,7,7-decafluoro-4,6-heptanedione', Inorg. Chem. **10**, pp.498-504 (1971).

9. R.E. Sievers and J.E. Sadlowski, 'Volatile metal complexes', Science **201**, pp.217-223 (1978).

10. K.J. Eisentraut and R.E. Sievers, 'Volatile rare-earth chelates of 2,2,6,6-tetramethylheptane-3,5-dione', Inorg. Synth. **11**, pp.94-98 (1968).

11. A. Weber and H. Shur, 'Thin lanthanum oxide and rare-earth oxide films by PECVD of β-ditekonate chelate complexes', Mod. Phys. Lett. B, **3**, pp.1001-1008 (1989).

12. C. Oehr and H. Shur, 'Thin copper films by plasma CVD using copper-hexafluore-acetylactonate', Appl. Phys. A, **45**, pp. 151-154 (1987).

13. H. Holzschuh et al., 'Thin films of barium, yttrium, europium, erbium and copper oxides prepared by plasma enhanced CVD', Mod. Phys. Lett.B, **2**, pp.1253-1257 (1988).

14. R.P. Tuminelli, B.C. McCollum and E.Snitzer, 'Fabrication of high-concentration rare-earth doped optical fibres using chelates', J. Lightwave Technol., **8**, pp.1680-1683 (1990).

15. K. Shuto, K. Hattori, T. Kitagawa, Y. Ohmori and M. Horiguchi, 'Erbium-doped phosphosilicate glass waveguide amplifier fabricated by PECVD', Electron. Lett., **29**, 2, pp.139-141 (1993).

16. J.E. Sicre, J.T. Dubois, K.J. Eisentraut and R.E. Sivers, 'Volatile lanthanide chelates. II. Vapor pressures, heats of vaporization and heats of sublimation', J. Am. Chem. Soc., **91**, pp.3476-3481 (1968).

17. R.W.G. Wyckoff, 'The structure of Crystals', 2nd. Ed., The Chemical Catalog Company Inc., pp252-254.

18. R.Weast, ed., 'CRC handbook of chemistry and physics', 51st Ed., F-152.

19. A.F. Wells, 'Structural inorganic chemistry', 3rd. Ed, Oxford at the Clarendon Press, pp.464-466.

20. A.C. Jones, 'Metalorganic precursors for semiconductors. Requirements and recent developments', J de Phys. C2, **1**, (1991).

21. P.F. Wysocki, J.L. Wagner, M.J.F. Digonnet, and H.J. Shaw, 'Evidence and modelling of paired ions and other loss mechanisms in erbium doped silica fibres', SPIE, **1789**, Fiber Laser Sources and Amplifiers IV, pp.66-79 (1992).

22. R. Wyatt, 'Spectroscopy of rare-earth doped fibres' in 'Optical fibre lasers and amplifiers', E. Snitzer Ed., pp.78-105 (1991).

Chapter 7: Conclusions

7.1. Objectives

The objective of the thesis was to fabricate and model active glass with the appropriate characteristics for optical integration. Glass waveguides must have low losses and accurate refractive index control. High doping levels are required for short active waveguiding devices. Clusters and ion-pairs can form when high rare-earth concentrations are used.

The experimental aim was to determine whether PECVD silica could incorporate high rare-earth dopant concentrations without the onset of clustering.

The theoretical performance of erbium doped optical amplifiers was analysed with the effect on gain of ion-pairs taken into consideration.

7.2. Summary of research

Chapter 3 starts with a review of the research on rare-earth lasers and excited states. The electronic configuration of rare-earth ions is such that the position of their absorption and emission bands are not strongly effected by the host and external fields. By changing the glass matrix, the shape and magnitude of the spectra can be slightly modified and broadened, however, the position of the peak emission and absorption does not generally shift. Pure silica has a rigid network which can incorporate only small amounts of rare-earths before the appearance of clusters. The solubility of rare-earth ions in silica has been improved[1] by the addition of codopants, such as Al or P, which were shown to change the glass matrix. The effect of adding a codopant can be inferred by looking at the characteristics of the oxide components which form the glass. The addition of intermediate ions such as P and Al results in a higher erbium solubility, this is due to an increase of allowed bonding configurations. These considerations can explain how the addition of Al or P can eliminate clustering. Gain is not only effected by the presence of clusters but also by the Er^{3+}-ion distribution within a glass matrix.

When the project started, the literature gave conflicting evidence on whether an increase in concentration should result in an increase in gain. The source of the conflict could be that rare-earth doped glasses with the same composition can have several structures. The separation of rare-earth ions in the different structures effects gain. Thus an assumption of random distribution of rare-earth ions common to several models[2] may not always be correct. An historical literature search proved this assertion to be correct. There are several sites[3,4] for rare-earths in silica. Er^{3+}, with its high cationic field strength, requires a high coordination number of non-bridging oxygens to screen the electronic charge of the cation. If the number of codopant ions is insufficient for charge compensation, the rare-earths group together forming pairs, triplets, or quadruplets around a silica tetrahedron. The interionic separation of a rare-earth ion pair is between 3.5-5Å depending on the glass matrix. When two rare-earths of the same species sit in a pair, the energy transfer between the two excited ions has a deleterious affect on gain. The reduction in gain due to ion-ion interactions was linked with this unusual structure only on completion of the thesis. The presence of ion pairs[5,6] has been used to explain the sub-optimal performance of EDFA.

The energy levels of the erbium ion are labelled by the Russell-Saunders notation. The levels are introduced in chapter 3 and used in chapter 4 to derive the rate equations. An Er^{3+} concentration of about 10^{20} ions/cm^3 is required to achieve gains of a few dB/cm in a short device (<10cm). In chapter 4, the rate equations are solved to derive an expression for gain in terms of level populations and cross sections. The populations of the energy levels participating in radiative transitions are dependent on the waveguide design and pumping conditions, and on the concentration and distribution of the rare-earth ions. The waveguide geometry and refractive index profile can be tailored to improve pump efficiency through the overlap between Er^{3+} concentration and field intensity. Monomode channel waveguide amplifiers with small square cores and high refractive index step, result in the highest gain per centimetre. They provide polarisation insensitive signal gain, lower noise levels and higher pump efficiencies than planar waveguide amplifiers.

Ion-ion interactions lead to concentration quenching in Er^{3+}-doped glasses through either cooperative upconversion or cross-relaxation. It was initially assumed that the energy transfer rate between the two interacting ions was a

constant independent of concentration[2]. However, the interaction coefficient must be dependent on ion concentration. Gain is reduced by ion-ion interactions; the strength of interaction between randomly distributed rare-earth ions is insufficient to account for this reduction. The reduction in slope efficiency and increase in threshold is probably caused by rapid interactions between paired ions. This reduction is related to the proportion of the total Er^{3+} concentration which forms ion pairs. Several factors effect the ion pair concentration; deposition, processing techniques, and concentrations of codopants. For modest pump powers, ion pairs may not significantly vary the lifetime of the metastable level. They can, however, be detected by observing that for high population inversions the lifetime decay is not exponential. The lifetime decay curve presented in chapter 6 was obtained at high pump powers of a few hundred mW. The presence of an initial non exponential component may be attributed to ion pairs.

The experimental techniques and results are presented in chapters 5 and 6. The experiments were focused on the use of the Er^{3+}-ion as the sole dopant in a silica matrix. PECVD was chosen because of its compatibility with component forming techniques and because dopant concentration can be closely controlled by using gaseous precursors. A suitable sufficiently volatile Er^{3+} precursor was not commercially available. An extensive literature search on rare-earth organic compounds resulted in the choice of $Er(thd)_3$ as the precursor. It has a sufficiently high vapour pressure at temperatures above 140°C for use in PECVD and can be evaporated without decomposition. A novel heated container and gas delivery system was designed and built for the unusual precursor.

The three glass components: silica, alumina, and erbia were deposited and calibrated separately. After the calibration runs, the silica and erbia components were combined. Solvation problems similar to those found when producing glass from melts, and by MOCVD, were expected. It was found that increasingly high Er^{3+} concentrations could be introduced into a silica matrix without the onset of microscopic clustering. AES was used to obtain the composition of the films. RBS was employed to determine the exact Er^{3+} concentration. The refractive index of the films was measured by ellipsometry and prism coupling and varied from 1.78 for Er_2O_3 to 1.46 for SiO_2.

The films had the typical fluorescence spectra of Er^{3+}-SiO_2. The lifetime at low pump powers, and before annealing, was 9ms. After annealing, the lifetime for high pump powers was around 2-3 ms.

7.3. Applications

In the US, there is strong media attention on the 'information super-highway', an extension of the present telecommunication and cable television network. All future homes will have the use of visual and audio telephones, electronic mail, fax and interactive television via a single fibre. The Er-doped planar waveguide amplifier in several systems configurations will be an essential component of this future telecommunications network.

EDFAs offer significant competition to electronic repeaters in which the signal is detected, amplified, and then relaunched into a further length of fibre. The number of rare-earth fibre laser systems is proliferating. The variety of hosts now available provide special lasers for medical and sensor applications. However the applications for fibre lasers and amplifiers are limited by fibre geometry. The challenge of this thesis was to demonstrate that it is possible to fabricate a rare-earth doped material which can be integrated. Rare-earth doped waveguides which can easily be integrated will make it possible to construct a much wider range of cheap and compact optical systems for communications, sensors and medical instruments.

Nykolak et al.[7] have demonstrated a systems evaluation for an Er^{3+}-doped planar waveguide providing 15dB net optical gain with low noise. In the systems experiment, the planar waveguide amplifier was used in a preamplifier configuration, it resulted in 6dB enhanced sensitivity, limited by output coupling and component insertion loss.

A single mode waveguide amplifier and laser have recently been demonstrated[8] in an Er-doped P-SiO_2 glass fabricated by PECVD. A signal gain of 0.33dB/cm was obtained using a 0.98μm pump of 420mW power, the threshold was 70mW and the slope efficiency was 1.4%.

Kitagawa[9] presented an Er-doped silica based planar amplifier module with single mode fibre pigtails pumped with 980nm laser diodes. The application of this module is as an optical preamplifier. The Er-doped glass was deposited by flame hydrolysis. The preamplifier worked at 2.488GHz bit rate, the gain output was 0.11dB/cm, and the noise figure was 3.8dB.

7.4. Future Work

It has been shown that high Er^{3+} concentrations can be incorporated into glass whilst maintaining a radiative lifetime of a few ms. Although it was beyond the scope of the programme to fabricate a waveguide device, modelling work presented in Ch. 4 indicates that gains of a few dB/cm can be achieved. With the view to future developments, however, the addition of a second rare-earth codopant may be a more promising way of achieving high optical gains. There is theoretical[10] and experimental[11,12,13,14] evidence of this in the case of Er-Yb doped glasses. If, as it appears, interactions between Er-Yb ions are beneficial, then the ion pair formation should not be avoided but encouraged. The energy transfer between two rare-earth ions of different species can increase gain. There are therefore two approaches for maximising gain; producing an Er^{3+} doped glass with a low ion pair concentration or introducing a second rare-earth in the matrix. Several of the recently reported high gains were achieved by using glasses which contain two rare-earths in ion pairs. It can be deceiving to relate the gain to the Er^{3+} concentration when it is the ion separation and hence the distribution which is the primary factor that affects gain.

Wang et al.[15] reported the fabrication of an Er-doped composite glass waveguide amplifier. The phosphate used had an Er concentration of $N_{Er}=1x10^{19}$ ions/cm^3 and the Yb concentration was $N_{Er}=1X10^{21}$ ions/cm^3. Kitagawa[16] disputed the reported gain of 21dB/cm because it was in disagreement with the experimental[17,18] and theoretical results on Er-doped fibre amplifiers published in the early nineties. It can however be explained by adapting Gapontsev's[19,20] theory of 1982 for Yb-Er glass lasers to waveguides.

In phosphate glass, Yb and Er are in ion pairs where the interionic separation is of 5Å. The transfer efficiency from Yb to Er is x=95%, and the back transfer from Er to Yb can be assumed to be negligible for Yb concentrations$<2x10^{21}$ions/cm^3. The result of this very efficient energy transfer is that practically total population inversions can be achieved that is, $n_2=n_{Er}$.

If the gain of the codoped glass is written approximately as

$$g = x\sigma_{Yb}n_{Er} \qquad 7.4\text{-}1$$

where the Yb emission cross-section at 0.9734μm is $\sigma_{Yb}=1.43X1^{-21}cm^2$. The maximum theoretical gain for Wang's waveguide is 22dB/cm (the experimental gain reported was 21dB/cm).

The aim of the project was that of finding whether an increase of Er^{3+} concentration would result in an increase in gain for short glass waveguides. It was demonstrated that PECVD silicate glass can be doped with high (10^{20}-10^{22} ions/cm^3) erbium concentrations. Formation of clusters and ion pairs within the glass was forecast as the most serious problem to overcome. Component clustering did not occur. The presence of ion pairs was observed experimentally, and included in the model. The results of the model showed that an increase in Er^{3+} concentration leads to an increase in gain even in the presence of ion pairs. It would be interesting for future work to find out whether there is a relation between annealing temperature and lifetime, and a critical temperature at which a short lifetime, indicative of ion pairs, appears. It would also be of interest to investigate how adding Al, P, Yb and other codopants effect the spectral shape, the fluorescence intensity and the lifetime decay.

References

1. K. Arai, H. Namikawa, K. Kumata, and T. Honda, 'Aluminium or phosphorous co-doping effects on the fluorescence and structural properties of neodymium-doped silica glass', J. Appl. Phys., **59**, pp.3430-3436 (1986).

2. P. Blixt, J. Nilsson, T. Carlnas and B. Jaskorzynska, 'Concentration-dependent upconversion in Er^{3+}-doped fiber amplifiers: experiments and modelling', IEE Trans. Photonics Technol. Lett., **3**, pp.996-998 (1991).

3. C.C. Robinson, 'Multiple sites for Er^{3+} in alkali silicate glasses(I). The principal sixfold coordinated site of Er^{3+} in silicate glass', J. Non-Cryst. Solids, **15**, pp.1-10 (1974).

4. C.C. Robinson, 'Multiple sites for Er^{3+} in alkali silicate glasses(II). Evidence of four sites for Er^{3+}', J. Non-Cryst. Solids, **15**, pp.11-29 (1974).

5. P.F. Wysocki, J.L. Wagener, M.J.F. Digonnet and H.J. Shaw, 'Evidence and modelling of paired ions and other loss mechanisms in erbium-doped silica fibers,' Proc. SPIE, **1789**, pp.66-79 (1992).

6. T. Georges, M. Monerie, P. Lamouler, J.F. Bayon, and E. Delavaque, 'Pair-induced quenching in erbium-doped silicate fibers,' Tech. Digest Series, **17**, pp.71-78 (1992).

7. G. Nykolak, M. Haner, P.C. Becker, J. Shmulovich, and Y.H. Wong, 'Systems evaluation of an Er^{3+}-doped planar waveguide amplifier', IEEE Photonics Technol. Lett., **5**, 10, pp.1185-1187 (1993).

8. K. Shuto, K. Hattori, T. Kitagawa, M. Horiguchi, 'Single-mode waveguide amplifier and laser in erbium doped glass waveguides fabricated by PECVD', OAA Proc., MoP 2.3, pp.53-55 (1993).

9. T. Kitagawa, K. Hattori, K. Shuto, M; Oguma, J. Temmyo, S. Suzuki, M. Horiguchi, 'Erbium-doped silica-based planar amplifier module with single-mode fiber pigtails pumped with 980nm laser diodes', OAA Proc., ThC. 12-11, pp.41-43 (1993).

10. F. Di Pasquale and M. Federighi, 'Improved gain characteristics in high-concentration Er^{3+}/Yb^{3+} co-doped glass waveguide amplifiers', J. Quantum Electronics, to be published (1994).

11. E. Snitzer and R. Woodcock, 'Yb^{3+}-Er^{3+} glass laser', Appl. Phys. Lett., **6**, 3, pp.45-46 (1965).

12. J.A. Hutchinson, T.H. Allik, 'Diode array-pumped Er, Yb: phosphate glass laser', Appl. Phys. Lett., **60**, 12, pp.1424-1426 (1992).

13. P. Laporta, S. De Silvestri, V. Magni, and O. Svelto, 'Diode-pumped cw bulk Er:Yb:glass laser', Opt. Lett., **16**, 24, pp.1952-1954 (1991).

14. P. Laporta, S. Longhi, S. Taccheo, O. Svelto, and G. Sacchi, 'Single-mode cw erbium-ytterbium glass laser at 1.5μm', Opt. Lett., **18**, 1, pp.31-33 (1993).

15. W.J. Wang, S.I. Najafi, S. Honkanen, Q. He, C. Wu, J. Glinski, 'Erbium doped composite glass waveguide amplifier', Electron. Lett., **28**, pp.1872-1873 (1992).

16. T. Kitagawa, K. Hattori, Y. Hibino and M. Horiguchi, 'Comment on Erbium doped composite glass waveguide amplifier', Electron. Lett., **29**, 1, pp.131-132 (1992).

17. J. Shmulovich, A. Wong, Y.H. Wong, P.C. Becker, A.J. Bruce and R. Adar, 'Er^{3+} glass waveguide amplifier at 1.5μm on silicon', Electron. Lett., **28**, 13, pp. 1181-1182 (1992).

18. T. Kitagawa, K. Hattori, K. Shuto, M. Yasu, M. Kobayashi, M. Horiguchi, 'Amplification in erbium-doped silica based planar lightwave circuits', SPIE Proc., PD pp. 1-4 (1992).

19. V.P. Gaponsev, A.K. Gromov, N.S. Platonov, 'Peculiarities of energy transfer in high-activated disordered laser materials', International Conference on Lasers Proc., pp. 315-320 (1982).

20. V. P. Gapontsev, S.M. Matitsin, M.E. Zhabotinski, 'Influence of excited-state absorption on the emission characteristics of Erbium glass laser', International Conference on Lasers Proc., pp. 321-326 (1982).

Appendix A: List of publications

1. M. Federighi, I. Massarek, P.F. Trwoga, 'Optical amplification in thin film waveguides with high Er concentration', IEEE Photonics Technol. Lett., 5, 2, pp.227-229 (1993).

2. I. Massarek, P.F. Trwoga, M. Federighi, 'Ion-ion interactions in waveguides with high Er concentration', ECIO Proc., 3, pp.40-41(1993).

3. F.Di Pasquale, M. Zoboli, M. Federighi, I. Massarek, 'Finite-element modelling of silica waveguide amplifiers with high erbium concetration', IEEE Photonics Technol., to be published (1994).

4. M.Federighi, I.Massarek, P.F. Trwoga, 'Modeling of optical waveguides with high Er concetration' J. Lightwave Technol., to be published (1994).

Appendix B: Concentration unit conversion

Rare earth concentrations are often quoted in different units: ppm, At.%, Wt.%, ions/cm^3 or ions/m^3. The conversion between the units is straight forward and is presented here.

The atomic weight of Er $Z_{Er} = 167$. The atomic weight of SiO_2 $Z_{SiO_2} = 60$. The density of silica[1] is $\rho = 2.2 g/cm^3$. The number of molecules per cubic centimetre with the same composition as the glass matrix is:

$$N = \frac{\rho N_A}{xZ_{Er} + yZ_{SiO_2}} \qquad \text{B.1}$$

where Avogadro's number, $N_A = 6.023 \times 10^{23}$ / mole. x is the Er concentration in At.%, and y is the SiO_2 concentration in At.%. For multi-component glasses extra terms must be added to the denominator of equation B.1. The Er concentration in ion/cm^3 is xN. 1At%=2.2 x10^{20}ion/cm^3.

To convert from At% to ppm, multiply by 10^4. That is 1At%=10000ppm.

The number of molecules per cubic centimetre with the same composition as the glass matrix is:

$$N = \frac{\rho N_A m}{Z_{Er}} \qquad \text{B.2}$$

where m is the Er weight.

---

[1]D.Lide Ed., 'CRC handbook of chemistry and physics', 73rd Ed., (1993).